Physics – Uspekhi **68** (1) 46 – 86 (2025)

REVIEWS OF TOPICAL PROBLEMS

PACS numbers: 42.25.Bs, **71.35. – y, 78.67. – n**

ON THE 90th ANNIVERSARY OF THE P.N. LEBEDEV PHYSICAL INSTITUTE (LPI)

Optics of plasmon-exciton nanostructures: theoretical models and physical phenomena in metal/J-aggregate systems

V.S. Lebedev, A.D. Kondorskiy

DOI: https://doi.org/10.3367/UFNe.2024.08.039742

Contents

Abstract. We review the studies of a wide range of optical phenomena resulting from near-field coupling between excitons and localized surface plasmon-polaritons in hybrid nanostructures. Modern physical approaches and theoretical models reported here for the description of light absorption, scattering, and extinction spectra are appropriate for interpreting physical effects in nanosystems containing metals and various excitonic materials, such as molecular aggregates of organic dyes or inorganic quantum-confined semiconductor structures. Using the example of hybrid nanosystems composed of a metallic core and an outer shell of dye J-aggregate, we perform a theoretical analysis of the optical spectra behavior in the regimes of weak, strong, and ultrastrong plasmon-exciton coupling. We consider resonance and antiresonance phenomena induced by the coupling of an exciton with dipole and multipole plasmons, including a pronounced dip in light absorption, as well as the spectral band replication effect of plexcitonic nanoparticles and their dimers. In addition, we discuss the significant roles of the size-dependent permittivity of the metallic core, the effects of anisotropy and chirality of the excitonic J-aggregate shell, and the influence of an intermediate passive layer on the formation of the optical spectra of bilayer, trilayer, and multilayer nanoparticles. The review outlines the experimental and theoretical results for hybrid nanosystems of various geometri-

V.S. Lebedev [(1)], **A.D. Kondorskiy** [(2)]
Lebedev Physical Institute, Russian Academy of Sciences,
Leninskii prosp. 53, 119991 Moscow, Russian Federation
E-mail: [(1)] vlebedev@lebedev.ru, [(2)] kondorskiy@lebedev.ru

Received 7 May 2024, revised 27 August 2024
Uspekhi Fizicheskikh Nauk **195** (1) 50 – 93 (2025)
Translated by I.A. Ulitkin

cal shapes, sizes, and compositions, broadens our understanding of the physical phenomena caused by the plasmon-exciton coupling, and represents the current state of research in the optics of metalorganic nanostructures.

Keywords: nanophotonics, optical spectra, light–matter interaction, plexcitonics, plasmon-exciton interaction, hybrid nanomaterials, core-shell nanoparticles, metal/J-aggregate nanostructures, localized surface plasmon-polaritons, delocalized Frenkel excitons

1. Introduction

Over the past two decades, optical properties of various hybrid nanoparticles and nanometer structures, as well as effects of their interaction with light fields, have been comprehensively studied by leading scientific centers. Interest in hybrid nanosystems is motivated by intense development of nanophotonics, nanoplasmonics, and the physics of quantum-confined structures. Moreover, hybrid nanomaterials are used extensively to develop next-generation photonic, optoelectronic, and light-emitting devices [1–3]. We also note research and development efforts in the field of optical switches [4, 5], memory elements [6, 7], photodetectors [8], photovoltaic elements [9–11], light-emitting diodes [12, 13], and nanosensors [14–16]. Much attention is paid to the development of the element base for nanophotonic integrated circuits [17, 18] and plasmonic networks controlling optical information [19], nanolasers and spasers [20–22], superlenses, nanowaveguides, and near-field optical probes [23–25], as well as a number of other devices operating on the basis of subwavelength optics effects and quantum-confinement, nonlinear optical, and plasmon-induced phenomena. Of considerable importance in this context are studies and developments in the field of hybrid organic/inorganic photonics and optoelectronics [26–28].

Particular focus has been put onto the study of optical properties of hybrid systems consisting of metal nanoparticles and molecular complexes, including dye aggregates. Physical properties of metal nanostructures and effects of their interaction with light fields have been studied in detail [29–35]. Metal structures and nanoantennas fabricated on their basis [36, 37] are capable of converting light into a highly localized electromagnetic field associated with collective oscillations of free electrons in metals. Such structures and devices make it possible to control and manipulate light fields on a nanometer scale [38, 39], increasing significantly the photodetection efficiency [40], the intensity of photoluminescence [41–45] and light scattering [46–49], and the sensitivity of biological and chemical sensors [50–52].

The use of ordered dye aggregates as an organic subsystem of metalorganic nanostructures has advantages over monomer molecules. A characteristic feature of J-aggregates is that, due to the translational order, electronic excitations of individual molecules are collectivized, forming Frenkel excitons. J-aggregates of polymethine (cyanine) dyes have a very narrow optical absorption peak (J-band), shifted to the red spectral range relative to the peak of the monomer of the same dye. They also exhibit resonance fluorescence with a small Stokes shift, an anomalously large oscillator strength of the transition in the J-band, and a giant nonlinear optical susceptibility. These unique optical properties arise due to the coherence of the states of molecules constituting the J-aggregates. A number of reviews are devoted to describing the structure, synthesis, and physicochemical properties of cyanine dye aggregates [53–57]. In recent years, the optical properties and effects of excitation energy transfer in aggregates of more complex types, such as tubular aggregates [58], columnar aggregates [59], X-aggregates [60], and multichromic multilayer aggregates [61, 62], have been intensively studied.

As has been shown [63–70], metalorganic nanoparticles containing J-aggregates have unique optical properties. In certain regimes of their interaction with light fields, they combine advantages of the excitonic subsystem (a large oscillator strength of the radiative transition and a small width of the J-absorption band) and the plasmonic subsystem, which is capable of enhancing strongly the local field near the surface of the metal nanoparticle compared to external electromagnetic radiation. Strong local light fields can modify the electronic structure and properties of J-aggregates [71]. Therefore, they may significantly affect photoluminescence processes of dyes deposited on plasmonic nanostructures [72–74]. Many interesting effects, such as giant Raman scattering [75–77], plasmon-enhanced fluorescence of J-aggregates [78, 79], superquenching (a sharp decrease in fluorescence intensity) [80], photoinduced charge separation reactions in J-aggregates near a metal surface or metal particles [81], plasmon-enhanced resonance energy transfer from donor molecules to acceptors, and energy transfer from molecular aggregates to surface plasmons [82–85], are manifested in various metalorganic systems.

In the physics of composite nanosystems containing metal particles of various shapes and sizes and molecular aggregates of dyes deposited on them, of greatest interest are the effects that arise as a result of coupling between Frenkel excitons and localized surface plasmons excited in the metal subsystem under the action of light [86–95]. Related to this area of research are investigations of the effects of near-field coupling between Frenkel excitons and propagating surface plasmons in planar systems containing J-aggregates of dyes deposited on a flat metal substrate [96–100]. To a considerable extent, these physical phenomena are similar to the intensively studied effects resulting from plasmon-exciton coupling in hybrid systems containing quantum-confined semiconductor compounds and metal nanostructures [101–106], including nanoparticles and thin films. Similar optical phenomena stem from electromagnetic coupling between excitons and polaritons or plasmon-polaritons in microcavities [107–111].

Plasmon-exciton coupling leads to the emergence of new hybrid states of the system with optical properties different from those of each of its components. In the general case, the spectrum of a composite system cannot be described as a simple superposition of the spectra of individual components. The effects that arise here are called plasmon-exciton coupling or, for short, plexcitonic coupling [112–114]. It has been shown that, due to plexcitonic coupling, it is possible to effectively control luminescence, absorption, and scattering spectra of light in metalorganic nanostructures by varying the geometric parameters and shape of their components [115–119]. The behavior of these spectra also depends markedly on specific values of optical constants of metals and molecular aggregates that constitute hybrid nanostructures, including on the magnitude of the oscillator strength of the J-band transition in the dye [89, 120, 121] and the mutual positions of

plasmon resonance peaks and the center of the absorption J-band [89, 122]. All these factors make it possible to radically influence the spectral-kinetic and nonlinear-optical [123, 124] properties of the composite plexcitonic system. The most striking physical phenomena are manifested in the regimes of strong and ultrastrong coupling between plasmons and Frenkel excitons of molecular J-aggregates [86–106, 116, 118–134].

To date, several reviews devoted to the discussion of various aspects of plasmon-exciton interaction have been published [135–142]. They discuss general principles of plexcitonic coupling and some applications to photonics and optoelectronics; describe methods for creating the plexcitonic nanosystems; consider the effects of plasmon amplification and quenching of spontaneous emission, as well as exciton energy transfer between quantum emitters; and study other topical issues. However, to date there are no reviews that would present a clear and sufficiently complete physical picture of plexcitonic phenomena in the optics and spectroscopy of metal nanoparticles and nanostructures of various shapes and sizes, coated with an outer shell of molecular aggregates of dyes. Moreover, a number of physical approaches and analytical models of plexcitonic coupling have not yet received proper theoretical discussion in the literature. Furthermore, many results of specific experiments and theoretical calculations of the processes of absorption, scattering, and extinction of light, as well as of photoluminescence in such composite nanosystems, have been left without due attention.

This review presents the current state of research in the optics of metalorganic nanosystems and considers the effects of near-field coupling between Frenkel excitons and localized surface plasmons in such systems. The analysis of plexcitonic coupling effects includes the cases of dipole and multipole plasmons, the influence of which increases with increasing particle size. We report the results of numerical calculations and experiments for hybrid particles of simple spherical shape and more complex geometric shapes, including nanorods, nanodisks, and nanoprisms. The contributions of light absorption and scattering processes to the total extinction cross sections for different particle sizes are discussed. We clarify the influence of the size-dependent dielectric functions of their metal core on the spectral distributions of the coefficient of light absorption by a core–shell nanoparticle. The behavior of the optical spectra of two- (metal/J-aggregate), three- (metal/spacer/J-aggregate), and multilayer nanoparticles is studied. In addition to the commonly used isotropic model of the excitonic outer shell of a nanoparticle, we report results demonstrating the significant influence of the effects of anisotropy of the outer J-aggregate shell and orientation phenomena on the formation of optical spectra of hybrid plexcitonic particles with a metal core. We provide a detailed discussion of various plasmon-exciton coupling regimes and consider a number of resonance and antiresonance phenomena observed when light interacts with plexcitonic nanoparticles. They include a pronounced dip in light absorption (or induced transparency in transmission spectra), and spectral band replication in hybrid metalorganic dimers consisting of metalorganic nanospheres and nanodisks placed close to each other. We also note possible applications of the fundamental results presented in the review to the fabrication of new materials with specified optical properties for developing efficient photonic and optoelectronic devices.

2. Surface plasmon-polaritons

2.1 Introductory remarks

Below, we present some preliminary remarks on surface plasmon-polaritons which are necessary for understanding the effects of near-field plexcitonic coupling. Surface plasmon-polaritons are formed under certain conditions at the interface between a metal and a dielectric as a result of the interaction of free electrons of the conductor with electromagnetic radiation. The physical essence of these surface waves of a combined nature is that the electron density in the metal oscillates coherently with the electromagnetic field in the surface layers of both the metal and the dielectric. There are two types of surface plasmon-polaritons: propagating surface plasmon-polaritons (PSPPs) and localized surface plasmon-polaritons (LSPPs) [141, 142]. The excitation of such waves is possible not only in systems with flat or extended curved surfaces (for example, in metal films, nanowires, and nanowaveguides) but also in nanoparticles of various geometric shapes and sizes (nanospheres, nanorods, nanodisks, nanoprisms, nanocubes, and nanostars) and in their arrays, as well as in nanopores in three-dimensional structures and holes in metal films. A necessary condition for the excitation of surface plasmon-polaritons, both propagating along the flat boundary of a two-component metal/dielectric system and localized in a metal nanoparticle surrounded by a dielectric medium, consists in the difference in signs of the real parts of the permittivities of the metal, $\mathrm{Re}\,\{\varepsilon_\mathrm{m}\} < 0$, and the dielectric, $\mathrm{Re}\,\{\varepsilon_\mathrm{d}\} > 0$. We shall start by recapping the main concepts of the theory of propagating surface plasmon-polaritons, which will allow us to highlight the common physical nature of the two types of plasmon-polaritons, PSPPs and LSPPs, and to point out differences in their properties. Note that the words 'surface' and 'polariton' in the terms PSPP and LSPP are often omitted for brevity.

2.2 Propagating surface plasmon-polaritons

Under certain conditions, surface plasmon-polaritons can be excited by light and propagate in a thin layer along a flat metal–dielectric interface. This situation is illustrated in Fig. 1, which shows a schematic view of the electric field of a surface wave propagating along the x-axis directed along this interface. The z-axis is directed along the normal to the surface, such that, at $z > 0$, the material of the hybrid system is a dielectric, and the region $z < 0$ is filled with a metal. The alternating charge signs in the near-surface layer of the metal shown in Fig. 1 mean that oscillations of the electron density are predominantly longitudinal along the x direction of electromagnetic field propagation [143]. Analysis of the boundary conditions shows [143] that, in this case, the electromagnetic field is a transverse magnetic (TM) wave in which the magnetic field, **H**, is normal to the plane of the figure ($H_x = H_z = 0$), and the electric field, **E**, has both longitudinal (E_x) and transverse (E_z) components. For such plasmon-polaritons, the dispersion relation has the form

$$k_x^{\mathrm{SPP}} = \frac{2\pi}{\lambda}\sqrt{\frac{\varepsilon_\mathrm{d}\varepsilon_\mathrm{m}}{\varepsilon_\mathrm{d}+\varepsilon_\mathrm{m}}}, \qquad k_z^{\mathrm{SPP}} = \begin{cases} \dfrac{2\pi}{\lambda}\sqrt{\dfrac{\varepsilon_\mathrm{d}^2}{\varepsilon_\mathrm{d}+\varepsilon_\mathrm{m}}}, & z > 0\,, \\ \dfrac{2\pi}{\lambda}\sqrt{\dfrac{\varepsilon_\mathrm{m}^2}{\varepsilon_\mathrm{d}+\varepsilon_\mathrm{m}}}, & z < 0\,. \end{cases} \tag{1}$$

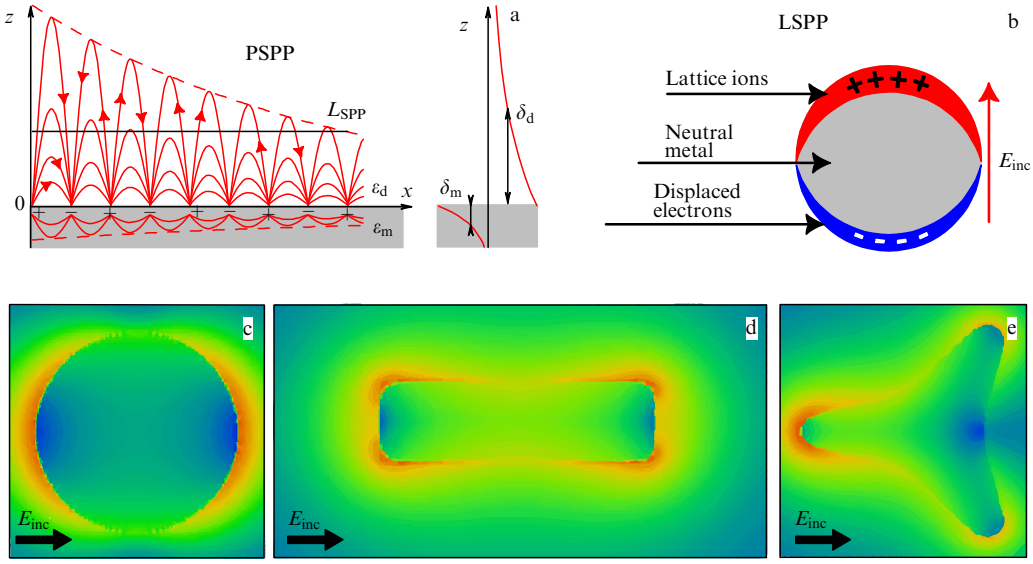

Figure 1. (a) Schematic view of a propagating surface plasmon-polariton (PSPP) along planar metal/dielectric interface. (b) Illustration of mechanism of charge separation on surface of metal nanosphere leading to the formation of a localized surface plasmon-polariton (LSPP) induced by the electric field of incident wave, $\mathbf{E}_{inc}$. (c–e) Spatial distributions of square modulus $|E|^2$ of electric field in longitudinal section of nanoparticles: (c) disk, (d) rod, and (e) three-point star. Calculations were performed using FDTD method for wavelengths of incident light corresponding to positions of maxima of spectral peaks of longitudinal plasmon resonances, which are (c) $\lambda = 425$ nm for the disk, (d) $\lambda = 690$ nm for the rod, and (e) $\lambda = 510$ nm for the three-point star. The following geometric parameters of nanoparticles were used: (c) $D = 27$ nm (disk diameter) and $h = 15$ nm (disk thickness), (d) $D = 15$ nm (rod diameter) and $L = 49$ nm (rod length), and (e) $L = 35$ nm (distance between tips of the star) and $h = 35$ nm (star thickness). In figures (c–e), directions of electric field of wave incident ($\mathbf{E}_{inc}$) along normal to plane of figure are indicated by black arrows.

As follows from relations (1), when conditions

$$\mathrm{Re}\,\{\varepsilon_m + \varepsilon_d\} < 0\,, \qquad \mathrm{Re}\,\{\varepsilon_m \varepsilon_d\} < 0 \tag{2}$$

are met, the surface wave propagates along the interface between the media, and the field strength **E** decays exponentially along the normal direction both into the metal ($z < 0$) and into the dielectric ($z > 0$). The depths of field penetration into the metal (δ_m) and the dielectric (δ_d) are given by the expressions [143–145]

$$\delta_d = \frac{\lambda}{2\pi}\sqrt{\left|\frac{\varepsilon_d + \varepsilon_m}{\varepsilon_d^2}\right|}\,, \qquad \delta_m = \frac{\lambda}{2\pi}\sqrt{\left|\frac{\varepsilon_d + \varepsilon_m}{\varepsilon_m^2}\right|}\,, \tag{3}$$

where λ is the wavelength of light in a vacuum, and ε_m and ε_d are the permittivities of the metal and dielectric, respectively.

Table 1 shows the results of calculations using formula (3) for the values of the field penetration depth into the metal (δ_m) and the dielectric (δ_d) at different wavelengths of light (λ) in a vacuum. In the calculations, quartz (SiO_2) was chosen as a dielectric, and silver (Ag) and gold (Au) were used as metals. It is evident from the data in Table 1 that a wave traveling along the interface penetrates into the metal a significantly shorter distance than into the dielectric.

The surface plasmon-polariton undergoes attenuation as it propagates along the x-axis due to energy dissipation in the metal (see the dashed envelope in Fig. 1). The corresponding propagation length L_{SPP} can be expressed in terms of the imaginary part $\mathrm{Im}\,\{k_x^{SPP}\}$ of the complex wave vector of the surface plasmon, determined by dispersion law (1). According to [144, 145], the value of L_{SPP} mainly depends on the value of the permittivity of the metal (ε_m) at the surface plasmon oscillation frequency ($\omega = 2\pi c/\lambda$). It is determined by the expression [144, 145]

$$L_{SPP} = \frac{\lambda}{2\pi}\left(\frac{\varepsilon_d + \mathrm{Re}\,\{\varepsilon_m\}}{\varepsilon_d\,\mathrm{Re}\,\{\varepsilon_m\}}\right)^{3/2}\frac{\left(\mathrm{Re}\,\{\varepsilon_m\}\right)^2}{\mathrm{Im}\,\{\varepsilon_m\}}\,. \tag{4}$$

Table 1 also presents the results of calculations (formula (4)) of the propagation length (L_{SPP}) of the surface plasmon-polariton along the flat metal–dielectric interface in the direction of the x-axis. The data presented for two systems, quartz on silver and quartz on gold, show that the plasmon propagation length L_{SPP} depends substantially on the wavelength λ of the incident light in a vacuum and decreases significantly in the short-wavelength part of the visible spectrum. Thus, the L_{SPP} value is ≈ 5 μm in the case of silver at $\lambda = 0.5$ μm, while for gold, a cutoff effect occurs near this wavelength, i.e., the wave stops propagating along the gold–quartz interface along the x-axis. It also follows from Table 1 that plasmon-polaritons have the longest propagation lengths in the near-IR region. For example, in the vicinity of the telecommunication wavelength $\lambda \approx 1.5$ μm, the L_{SPP} value is several hundred microns in the case of Ag/SiO_2 and approaches one hundred microns in the case of Au/SiO_2.

It is important to recall one well-known feature of the dispersion law of propagating plasmon-polaritons. According to (1), when conditions (2) are met, the component k_x^{SPP} of the plasmon-polariton wave vector along the direction of its propagation, x, is always greater than the value of the wave vector, $k_d = 2\pi\sqrt{\varepsilon_d}/\lambda$, of the light wave in the dielectric at the frequency $\omega = 2\pi c/\lambda$. Therefore, due to the law of conservation of momentum, light freely propagating in the dielectric cannot directly excite a propagating surface plasmon-polariton (PSPP). A huge number of papers are devoted to various methods of excitation of propagating surface plasmon-polaritons to ensure the matching of momenta. In particular, the following excitation schemes have become wide-

Table 1. Results of calculations (using formulas (3)–(4)) of field penetration depth δ_m and δ_d and propagation length L_{SPP} of surface plasmon-polariton at flat interfaces of silver and gold with quartz (Ag/SiO_2 and Au/SiO_2) for different wavelengths λ of exciting radiation in vacuum.

	Ag/SiO_2			Au/SiO_2		
λ, μm	δ_{Ag}, nm	δ_{SiO_2}, nm	L_{SPP}, μm	δ_{Au}, nm	δ_{SiO_2}, nm	L_{SPP}, μm
1.5	21.7	1236	350	22.8	1174	87.7
1.0	21.9	527	225	24.0	478	28.7
0.7	22.1	241	42.3	25.6	200	7.62
0.5	22.5	103	5.42	34.5	71	0.003
0.4	21.7	44	0.68	does not propagate		

spread: (1) Kretschmann and (2) Otto configurations based on the phenomenon of frustrated total internal reflection; (3) excitation by an optical probe of a near-field microscope; and diffraction (4) on a grating, (5) on a corrugated structure, and (6) on inhomogeneities and roughnesses of the metal–dielectric interface (see, for example, [145, 146]).

2.3 Localized surface plasmon-polaritons

Localized surface plasmon-polaritons are excited in metal nanoparticles and metal-containing nanostructures whose size can be smaller than the wavelength of light, λ, and even smaller than the values of the penetration depth, δ_m, of the electromagnetic field into the given bulk metal sample (see Table 1). Modern synthesis methods make it possible to obtain nanoparticles of various shapes, including rather complex ones (Fig. 2). Similar to the case of propagating surface plasmon-polaritons, the localized field of electromagnetic waves near the nanoparticles is evanescent [147]. Its strength undergoes a strong local increase in the regions adjacent to the nanoparticle boundary inside and outside the metal. When localized plasmon-polaritons emerge in metal nanostructures, collective coherent oscillations of the charge density are excited in the near-surface layer, as is the case for extended geometry. However, unlike the case of propagating surface plasmon-polaritons, electron oscillations are confined by the closed surface of the nanoparticle, and the evanescent field is concentrated in the vicinity of the interface between the particle and the environment. Therefore, the properties of localized surface plasmon-polaritons are largely determined by the geometric shape and size of the nanoparticle, in addition to the permittivities of its material and the environment.

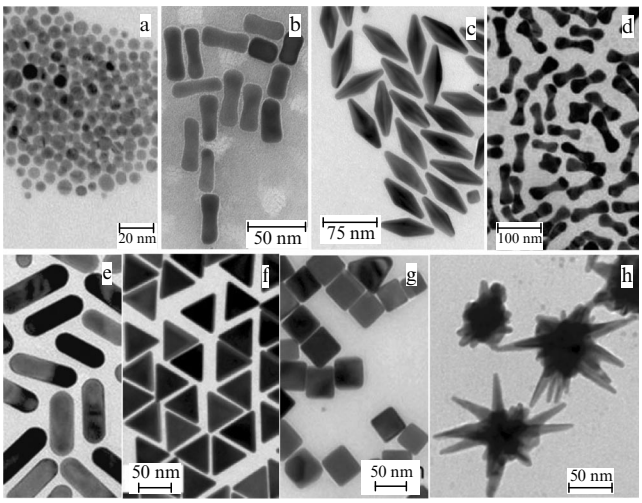

Figure 2. TEM images of metal nanoparticles of various shapes: (a) nanospheres [66], (b) nanorods [68], (c) nanobipyramids [151], (d) nanodumbbells [152], (e) nanorods with round ends [153], (f) triangular nanoprisms [154], (g) nanocubes [155], and (h) nanostars [156].

The mechanism of the formation of a localized surface plasmon-polariton is schematically shown in Fig. 1b, where a spherical particle is used as an example. An electromagnetic wave in metal nanoparticles displaces free conduction electrons relative to the ionic cores of the crystal lattice. As a result, surface charges of different signs at opposite ends of the particle generate a restoring field, the strength of which is proportional to the displacement of electrons relative to the ionic core. The signs of the positive and negative charges shown in Fig. 1b periodically change over time, following the oscillations of the external field, $\mathbf{E}_{inc}$. Thus, a metal particle is a system with a set of eigenfrequencies, the values of which are determined by the shape, size, and optical constants of the particle material and its environment [148, 149].

The shape of a nanoparticle dramatically affects the spatial distribution of the electric field. This is clearly demonstrated in Figs 1c–e, which show the results of our calculations of $|E|^2$ for a silver disk, rod, and three-point star. The calculations were performed using the finite-difference time-domain (FDTD) method. One can see from the figure that, for particles of a complex geometric shape, the field is strongly localized near the curved surface of the metal nanoparticle, and its intensity is maximal in those areas of space where the curvature of the particle surface is the highest, i.e., where the radius of curvature is especially small. Thus, the field distributions shown in Figs 1c–e confirm the validity of using the term "localized surface plasmon-polariton," since the field strength in the main part of the volume of the depicted particles is extremely low, and it actually exists only in the near-surface layer inside and outside the metal.

Note another fundamental difference between a localized plasmon-polariton and a propagating one. The excitation of the latter requires the matching of the wave vectors of the photon and the plasmon-polariton. In the case of localized plasmon-polaritons, due to the absence of propagation, the condition for the coincidence of the wave vectors of the photon and the plasmon-polariton is not needed. Accordingly, there is no difficulty in exciting plasmon-polaritons, as is the case for flat extended metal–dielectric surfaces.

When the radius of curvature, r, of the nanoparticle surface is less than the thickness of the metal skin layer, δ_m, in the bulk sample, which lies in the range of 20–35 nm in the visible and near-IR spectral ranges, then the fraction of the particle volume into which the field effectively penetrates gradually increases [149]. The specific nature of the field

localization inside and outside the particle and the depth of its penetration into the metal, δ_m, and the dielectric surrounding the particle, δ_d, substantially depend on the value of r. Correspondingly, the greatest increase in the local field compared to the incident field occurs near the vertices and tips of nanoparticles, for example, bipyramids, prisms, cubes, and stars (see, respectively, Figs 2c and f–h). Note that, when optical radiation interacts with nanoparticles of small size a, the quasistatic approximation is applicable if the condition $ka \ll 1$ is met. In this case, the contribution of the electric field dominates the contribution of the magnetic field to the total energy of the evanescent electromagnetic field.

In the opposite limiting case, when the radius of curvature of the particle surface (r) becomes much greater than the characteristic values of the field penetration depths into the metal and dielectric ($r \gg \delta_m, \delta_d$), the situation becomes similar to the case of a flat interface between these materials. In this case, the field is concentrated inside and outside the particle in the near-surface region, whose volume is significantly smaller than that of the particle. In this limit, the depth of field penetration into the metal is almost independent of the shape and size of the particle, but is determined only by the permittivities of the metal, ε_m, and the surrounding medium, ε_d, and their characteristic values correspond to the case of propagating plasmon-polaritons (see Table 1).

2.4 Size-dependent dielectric functions of nanoparticles

For metal particles, two ranges of size with qualitatively different electronic structure are usually distinguished. The characteristic size separating these ranges is the Fermi wavelength of the electron, which is $\lambda\!\!\!^{-}_F \sim 1$ nm for gold, silver, and copper. In the range of $r \lesssim \lambda\!\!\!^{-}_F$, quantum-confinement effects appear in the energy spectrum and optical properties of metal clusters, and the role of these effects increases with decreasing size. The properties of subnanometer metal clusters can be described by various quantum-mechanical methods and time-dependent density functional theory [150]. If the size of a noble metal particle exceeds $\lambda\!\!\!^{-}_F \sim 1$ nm, its energy spectrum becomes quasicontinuous within the allowed bands. Therefore, starting with sizes of several nanometers, it is possible to introduce the concept of the size-dependent dielectric function of a metal particle, ε_m, and describe its optical properties based on Maxwell's equations within the framework of classical electrodynamics of continuous media.

The local dielectric function of a noble metal in the visible and near-IR spectral ranges can be expressed as the sum of the contributions of intraband, ε_{intra}, and interband, ε_{inter}, transitions,

$$\varepsilon_m(\omega) = \varepsilon_{intra}(\omega) + \varepsilon_{inter}(\omega)\,, \tag{5}$$

$$\varepsilon_{intra}(\omega) = \varepsilon_m^{\infty} - \frac{\omega_p^2}{\omega^2 + i\omega\gamma_{intra}}\,,\ \omega_p = \left(\frac{4\pi n_e e^2}{m_e}\right)^{1/2}, \tag{6}$$

$$\varepsilon_{inter}(\omega) = K\int_{\omega_g}^{\infty} dx\,\frac{\sqrt{x-\omega_g}}{x}\left[1 - F(x,\Theta)\right] \times \frac{x^2 - \omega^2 + \gamma_{inter}^2 - 2i\,\omega\,\gamma_{inter}}{(x^2 - \omega^2 + \gamma_{inter}^2)^2 + 4\omega^2\gamma_{inter}^2}\,. \tag{7}$$

The quantity ε_{intra} in (5) is described by the modified Drude formula (6) and includes a frequency-dependent part (the second term in (6)) responsible for the collective oscillations of free electrons in the metal with plasma frequency ω_p and damping coefficient γ_{intra} ($1/\gamma_{intra}$ is the corresponding relaxation time of free electrons). In addition, following [157, 158], formula (6) contains a frequency-independent term — the constant ε_m^{∞}, which is generally not equal to unity.

The quantity ε_{inter}, described by formula (7), determines the frequency-dependent contribution of bound electrons, i.e., electron transitions between the valence d-band and the conduction sp-band of noble metals; $F(x,\Theta)$ is the distribution function of electron energy, $\hbar x$, at temperature Θ; and γ_{inter} is the damping coefficient for the specified interband transitions. According to [159, 160], transitions occur between the dispersionless d-band and the parabolic sp-conduction band with minimum energy $\hbar\omega_g$ relative to the d-band. The constant $K \propto D^2$, where D is the transition dipole moment.

Taking into account only the contribution of free electrons, one can put $\varepsilon_m^{\infty} = 1$ in formula (6). However, for convenience, a term $\varepsilon_m^{\infty} - 1$ is usually added to this formula [157, 158]; this term describes the contribution of those interband transitions that are not located in the visible and near-IR ranges of the spectrum and whose frequency dispersion can be ignored. According to [157], the typical values of the constant ε_m^{∞} for different metals can vary in the range $1 \leqslant \varepsilon_m^{\infty} \leqslant 10$.

When the particle size is small compared to the mean free path of electrons, l_∞, in a bulk metal, then, in calculating the value of $\varepsilon_{intra}(\omega)$, it is necessary to additionally take into account the size effect resulting from the scattering of free electrons at the interface between a metal particle and its external medium (e.g., solution or J-aggregate shell). This leads to the dependence of the damping coefficient γ_{intra} and, accordingly, the dielectric function $\varepsilon_{intra}(\omega, r)$ on both the particle frequency ω and the radius r. For the effective damping coefficient, we will use the well-known expression [161]

$$\gamma_{intra}^{(r)} = \gamma_{intra}^{bulk} + \xi\frac{v_F}{r}\,,\quad \gamma_{intra}^{bulk} = \frac{1}{\tau} = \frac{1}{\tau_{e\text{–}e}} + \frac{1}{\tau_{e\text{–}ph}} + \frac{1}{\tau_{e\text{–defect}}}\,. \tag{8}$$

Here, v_F is the Fermi velocity; ξ is a dimensionless constant ($\xi \sim 1$), the value of which is determined by the specifics of the scattering process of free electrons at the interface between a metal nanoparticle and its environment and can be found from a comparison with experimental data on photoabsorption; and γ_{intra}^{bulk} is the damping coefficient in a bulk metal, determined by the relaxation times $\tau_{e\text{–}e}$ and $\tau_{e\text{–}ph}$ in electron-electron and electron-phonon collisions, as well as the relaxation time $\tau_{e\text{–defect}}$ in electron scattering by defects, respectively.

Since the size effect has a weak influence on the contribution of bound electrons, following the semiempirical approach [161], use is often made of the expression

$$\varepsilon_m(\omega, r) = \varepsilon_{bulk}(\omega) + \omega_p^2\left(\frac{1}{\omega^2 + i\omega\gamma_{intra}^{bulk}} - \frac{1}{\omega^2 + i\omega\gamma_{intra}^{(r)}}\right) \tag{9}$$

to reliably describe both contributions to the permittivity of a metal particle taking into account the size effect. Here, ε_{bulk} is the experimentally obtained permittivity of the bulk metal (see Refs [162–165] for Ag, Au, Cu, and Al); γ_{intra}^{bulk} is the frequency of electron scattering in the bulk metal; and $\gamma_{intra}^{(r)}$ is

the frequency (8) of electron scattering from the surface of a metal particle.

To demonstrate the size-dependent behavior of the dielectric functions of silver and gold nanospheres with a size smaller than the mean free path of an electron in the bulk metal, Figs 3a and b show dependences of their real and imaginary parts on the wavelength for three values of the particle radius $r = 5$, 10, and 100 nm. One can see that the real parts $\mathrm{Re}\,\{\varepsilon_\mathrm{m}(\omega, r)\}$ of silver and gold depend weakly on r. In contrast, the imaginary parts $\mathrm{Im}\,\{\varepsilon_\mathrm{m}(\omega, r)\}$ depend significantly on the particle size, especially at $\lambda \gtrsim 320$ nm and 550 nm for Ag and Au, respectively, where the contribution of free electrons is dominant.

A comparison of the results of calculations of the light absorption spectra for a number of metal and metalorganic nanospheres of different radii r showed that the dielectric function determined by equations (8), (9) describes well the spectral manifestations of the size effect for Ag, Au, Cu, and Al [65, 66, 161]. In [166, 167], the same expressions were applied to nanoparticles of more complex shapes, including nanoprisms and nanorods. It was found that, even in the case of complex geometry, expressions (8), (9) allow us to accurately describe the available experimental data on the extinction spectra of metal nanoparticles. To this end, it is required to introduce the effective radius r_eff of a sphere with the same volume $\mathcal{V}$ as that of the nanoparticle under consideration as a dimensional parameter, i.e., $r_\mathrm{eff} = [3\mathcal{V}/(4\pi)]^{1/3}$. As was shown in [167], for silver nanoprisms, this approach provides a good agreement between theory and experiment when varying the prism size over a wide range.

For a very small size of a metal nanoparticle ($r \lesssim 2\pi v_\mathrm{F}/\omega$), its dielectric function should be calculated by taking into account the nonlocal nature of the relationship between the induction vectors **D** and the electric field strength **E**, which leads to spatial dispersion effects. The theory of light absorption by spherical metal particles of small radius with the spatial dispersion effects taken into account has been developed in a number of papers (see, for example, [168, 169]). In this case, the permittivity of a nanoparticle is a tensor even in an isotropic medium, and the distinct direction is defined by the wave vector **k**. Furthermore, when the medium also has an inversion center, one can introduce the quantities $\varepsilon_\mathrm{l}(\omega, k)$ and $\varepsilon_\mathrm{t}(\omega, k)$, referred to as the longitudinal and transverse permittivities, respectively. If $\mathbf{E} \parallel \mathbf{k}$, then $\mathbf{D} = \varepsilon_\mathrm{l}\mathbf{E}$, and if $\mathbf{E} \perp \mathbf{k}$, then $\mathbf{D} = \varepsilon_\mathrm{t}\mathbf{E}$. Thus, both transverse and longitudinal waves can propagate in the medium. Their dispersion laws are given by

$$k_\mathrm{t}^2 = \left(\frac{\omega}{c}\right)^2 \varepsilon_\mathrm{t}\,(\omega, k_\mathrm{t})\,, \qquad \varepsilon_\mathrm{l}(\omega, k_\mathrm{l}) = 0\,. \tag{10}$$

Within the framework of the hydrodynamic model of electron gas [170], which includes the spatial dispersion, the permittivity can be written as

$$\varepsilon(\omega, k) = 1 - \frac{\omega_\mathrm{p}^2}{\omega^2 + \mathrm{i}\omega\gamma - \beta^2 k^2}\,, \qquad \beta^2 = \frac{3}{5}\,v_\mathrm{F}^2\,, \tag{11}$$

so that the longitudinal wave vector turns out to be equal to

$$k_\mathrm{l}^2 = \frac{5}{3v_\mathrm{F}^2}\,(\omega^2 + \mathrm{i}\omega\gamma - \omega_\mathrm{p}^2)\,. \tag{12}$$

Calculations within the framework of this theory show that the nonlocal effects lead to a slight shift in the position of the maximum of light absorption by metal particles to the short-wavelength region of the spectrum as their radius r decreases [169]. The magnitude of the shift depends on the wavelength of light λ and Fermi velocity v_F, with the shift becoming stronger as the size of the sphere decreases. At the same time, the amplitude of the absorption peak decreases slightly. For silver nanospheres at $r = 1$ nm, the shift $\Delta\lambda$ in the position of the absorption maximum turns out to be equal to $\Delta\lambda = 11$ nm and decreases rapidly with increasing radius. At $r = 10$ nm, this shift becomes equal to only $\Delta\lambda = 1$ nm, and at $r > 10$ nm, it is negligible. For gold nanoparticles, nonlocal effects are even weaker.

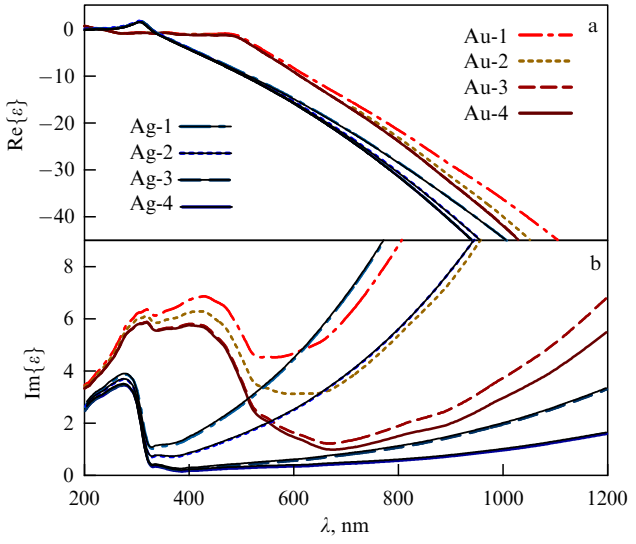

Figure 3. (a) Real and (b) imaginary parts of dielectric functions of silver and gold spherical nanoparticles calculated using formulas (8) and (9) for three values of their radius r: curves Ag-1, Ag-2, and Ag-3 for silver and Au-1, Au-2, and Au-3 for gold are plotted, respectively, at $r = 5$, 10, and 100 nm. Curves Ag-4 and Au-4 show experimental data for bulk samples [162, 163].

2.5 Dipole and multipole plasmon resonances

When the frequency of the external electromagnetic field coincides with one of the eigenfrequencies of plasma oscillations of a nanoparticle, the phenomenon of localized surface plasmon resonance is observed. Under resonant conditions the induced oscillations of free conduction electrons, being coherent with the electromagnetic field oscillations lead to a strong enhancement in the local field strength near the nanoparticle as compared to the external field strength. As a result, the light absorption and scattering cross sections increase drastically. The frequencies and widths of the resonance peaks of light absorption and scattering depend on the particle size, shape, and permittivities of the metal and the environment [29, 171, 172]. In aqueous solutions, silver and gold nanospheres exhibit plasmon-polariton resonances in the visible range. For many other metals, they are located in the UV range [89, 173].

For a homogeneous metal sphere, the frequency of the dipole plasmon mode can be determined in the quasistatic approximation ($kr \ll 1$) from the relation $\mathrm{Re}\,\{\varepsilon_\mathrm{m}(\omega)\} = -2\varepsilon_\mathrm{h}$. Here, ε_h is the permittivity of the host medium. Substituting expression (6) for the contribution of free electrons to the dielectric function ε_m and neglecting its

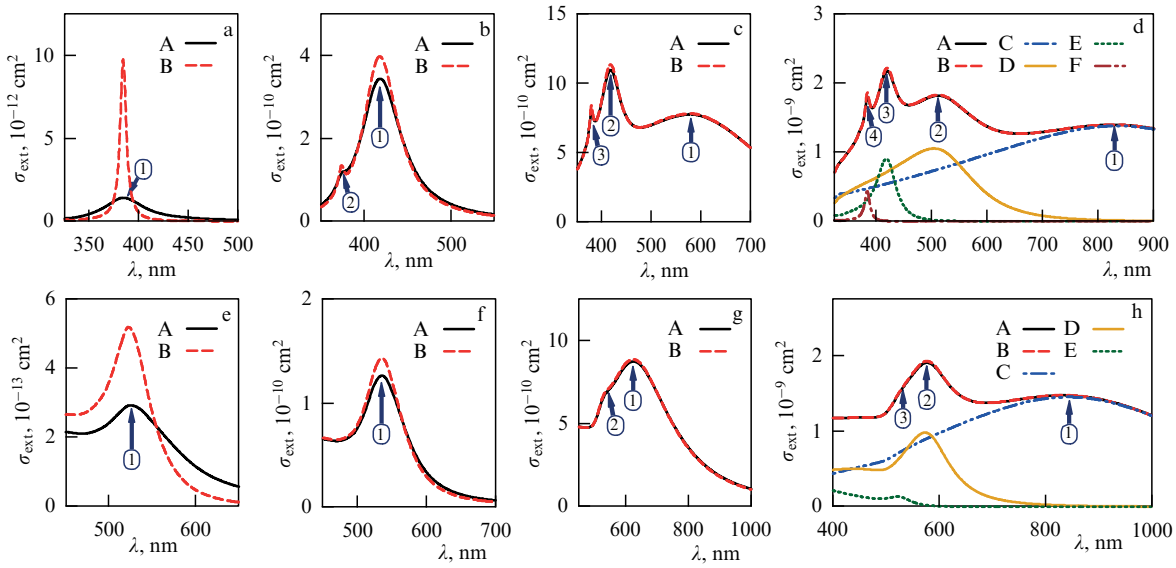

Figure 4. Extinction cross sections of (a)–(d) silver and (e)–(h) gold nanospheres with diameters $D = 10$ nm (a, d), 60 (b, f), 140 (c, g), and 220 nm (e, h) in an aqueous solution as a function of wavelength of light in vacuum, λ [33]. Solid black curves (A) are calculations based on Mie theory using size-dependent local dielectric functions $\varepsilon(\omega, D)$ of silver and gold particles (see formulas (8) and (9)). Red dotted curves (B) are similar results obtained using dielectric functions $\varepsilon_{bulk}(\omega)$ of bulk materials Ag and Au. Plasmon resonances in spectra are designated by numbers 1, 2, 3, and 4, indicating the nth order of the multipole. For particles of large diameter, $D = 220$ nm, curves C, D, E, and F in panels (d) and (h) show contributions of multipoles of different orders ($n = 1$, 2, 3, and 4, respectively) to total extinction cross section σ_{ext}.

imaginary part, we have

$$\omega_{pl}^{(dip)} \equiv \omega_{Fr} = \frac{\omega_p}{\sqrt{2\varepsilon_h + \varepsilon_m^{\infty}}}\,. \qquad (13)$$

This is the expression for the Fröhlich frequency [148], which determines the position of the resonant electric dipole plasmon mode, $\omega_{pl}^{(dip)}$, which relates it to the plasma frequency of electrons, ω_p, in the metal (6). Analytical consideration [29, 148] of the conditions for the excitation of electric-type plasmon resonance of the nth order of multipolarity leads to the well-known result: $\mathrm{Re}\,\{\varepsilon_m(\omega)/\varepsilon_h\} = -(n+1)/n$.

Figure 4 shows the results of calculations of the extinction cross sections σ_{ext} of silver and gold nanospheres in an aqueous solution, calculated within the framework of the standard Mie theory. The permittivity of the aqueous solution (the host medium surrounding the particle) changes slightly in the visible region of the spectrum and is $1.77 < \varepsilon_h < 1.82$ at $350 < \lambda < 700$ nm. A comparison of the dependences of the cross sections σ_{ext} on the wavelength of light at different sphere diameters $D = 10$, 60, 140, and 220 nm allows us to trace changes in the behavior of the extinction spectra. In particular, this makes it possible to determine changes in the positions of the intensity maxima of the peaks of localized surface plasmon resonances with an increase in particle size.

At $D = 10$ nm, the spectral peaks of gold (Fig. 4a) and silver (Fig. 4e) particles correspond to the electric dipole plasmon resonance ($n = 1$). An increase in the particle size (Figs 4b–h) leads to a qualitative change in the behavior of their extinction cross sections. This is primarily due to an increasing role of plasmon resonances of a higher multipolarity order, $n > 1$. In particular, Figs 4b–d clearly show the sequential formation of new spectral peaks for silver nanoparticles: first, quadrupole at $D = 60$ nm ($n = 2$, Fig. 4b); then, octupole at $D = 140$ nm ($n = 3$, Fig. 4c); and, finally, hexadecapole at $D = 220$ nm ($n = 4$, Fig. 4d). It is evident that the contribution of multipole resonances ($n > 1$) changes drastically the spectral behavior of extinction cross sections as compared to that for particles of a smaller diameter.

Results of similar calculations for gold particles (Figs 4e–h) also demonstrate the sequential formation of new spectral peaks of multipole plasmon resonances with increasing D. However, their specific impact on the behavior of the $\sigma_{ext}(\lambda)$ dependences noticeably differs from the previous case (Figs 4a–d). Note that, since the widths of plasmon resonances for gold turn out to be larger than those for silver, some peaks partially merge. As a result, the contribution to the extinction cross sections of multipole resonances on the order of $n > 1$ becomes more pronounced at higher values of D than that of resonances of the same order n in the case of silver particles.

The results shown in Fig. 4 allow us to establish how the size effect in the dielectric function (9) of silver and gold nanoparticles, $\varepsilon_m(\omega, r)$, affects their optical properties. We compared the results for $\sigma_{ext}(\lambda)$, calculated with (black solid curves) and without (red dotted curves) the effect associated with free electron scattering from the metal–water interface taken into account, i.e., using the permittivity of the bulk sample, $\varepsilon_{bulk}(\omega)$ [162, 163]. The size effect is especially strong in the case of a silver particle (Figs 4a–d) if its size, $D = 10$ nm, is significantly smaller than the mean free path of electrons, $l_{\infty}^{Ag} = 53.3$ nm, in the bulk sample. Then, the peak of the dipole plasmon resonance, calculated using the permittivity $\varepsilon_{bulk}^{Ag}(\omega)$ at $D = 10$ nm, turns out to be much narrower than that observed experimentally [66, 174]. In contrast, the use of the size-dependent dielectric function of silver, $\varepsilon_{Ag}(\omega, r)$, leads to the peak's broadening by a factor of 6.7 and 1.2 at $D = 10$ and 60 nm, respectively. The corresponding decrease in the maximum intensity of the dipole peak also turns out to be most significant at small particle sizes $D \ll l_{\infty}^{Ag}$.

When the particle diameter D becomes greater than $l_{\infty}^{Ag} = 53.3$ nm, the effect of the size-dependent dielectric

function of silver on the extinction spectrum is weak (Figs 4c and d). A similar analysis for Au (Figs 4e–h) shows that the influence of the size effect in the dielectric function on the spectral properties of gold nanoparticles is less than that in the case of silver [89, 117]. The reason is that, in the frequency range $\hbar\omega \lesssim 3.5$ eV, the main contribution to the permittivity of silver is made by intraband transitions, while interband transitions in gold begin to play a significant role already at $\hbar\omega \gtrsim 1.7$ eV. In addition, the mean free path of an electron in gold is lower than that in silver.

2.6 Effect of shape of nanoparticles on their optical spectra

For a particle of an elongated (for example, spheroid and rod) or oblate (disk, prism, and star) shape, the plasmon peak is split into two, so that the optical spectra exhibit longitudinal and transverse plasmon resonances. This holds true even for nanoparticles of a sufficiently small size, for which the quasistatic approximation is definitely justified. The greater the difference between the longitudinal and transverse sizes of the nanoparticle, the greater the spectral distance between the positions of the maxima of these peaks. The peak shifted toward shorter wavelengths corresponds to electron oscillations in the transverse direction relative to the long axis of the particle, and the second peak (shifted to the red) corresponds to oscillations in the longitudinal direction (Fig. 5).

These spectral features of elongated and oblate nanoparticles are clearly illustrated in Fig. 5. There we compare results of our calculations for the extinction cross sections of silver nanoparticles of different shapes. All calculations were performed using the FDTD method for nanoparticles having the same volume $\mathcal{V} = 8500$ nm^3. The following systems were chosen for this comparison: a sphere with diameter $D = 25$ nm (black solid curve *1*); a disk with diameter $D = 27$ nm and height $h = 15$ nm (red dashed curve *2*); a rod with transverse diameter $D = 15$ nm and longitudinal length $L = 49$ nm (blue dotted curve *3*); a dumbbell with length $L = 42$ nm, ball diameter $D = 20$ nm, and waist diameter $h = 10$ nm (brown dashed-double-dotted curve *4*); and a triangular prism with edge length $L = 33$ nm and height $h = 15$ nm (green dashed-dotted curve *5*). The presented results correspond to the cross sections averaged over three equiprobable particle orientations, corresponding to the nanoparticles randomly oriented in the solution. Calculations of the extinction spectra of nanoparticles of various shapes were also performed elsewhere [33, 171, 172, 175].

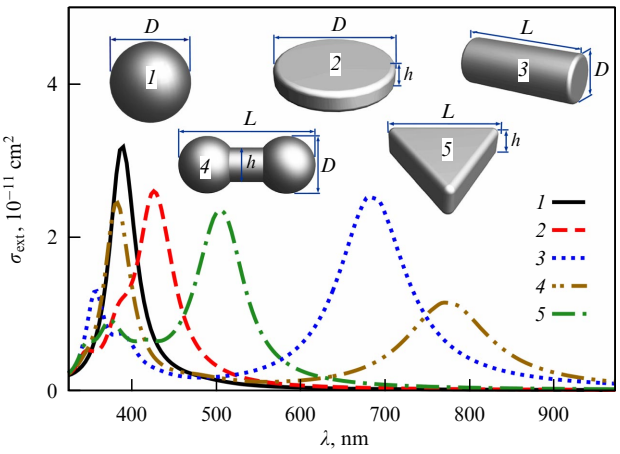

Figure 5. Extinction cross sections of silver nanoparticles in water as functions of light wavelength in vacuum, λ [175]. Particles have different shapes but same volume ($\mathcal{V} = 8500$ nm^3): *1* — sphere with diameter of 25 nm; *2* — disk with diameter $D = 27$ nm and height $h = 15$ nm; *3* — rod with diameter $D = 15$ nm and length $L = 49$ nm; *4* — dumbbell with length $L = 42$ nm, ball diameter $D = 20$ nm, and waist diameter $h = 10$ nm; *5* — triangular prism with edge length $L = 33$ nm and height $h = 15$ nm. Cross sections are averaged over all possible orientations of the particle.

Figure 5 clearly demonstrates the significant influence of the geometric shape of the nanoparticles on the behavior of the extinction cross sections, the positions of the maxima of the spectral peaks, and their total number. It is evident that for a small silver sphere, the extinction spectrum has only one peak corresponding to the electric dipole plasmon resonance (black solid curve *1*), whose position of the maximum is described well in the quasistatic approximation by the Fröhlich formula (13). Whereas, for a nanorod with a given ratio of the length to the transverse diameter, $L/D = 3.3$, there are two spectral peaks corresponding to the longitudinal (long-wavelength peak) and transverse (short-wavelength peak) plasmon resonances (blue dotted curve *3*). A similar situation is observed for a dumbbell (brown dashed-dotted curve *4*). Here for the aforementioned geometric parameters, the spectral distance between the peaks of the longitudinal and transverse resonances reaches $\Delta\lambda \approx 400$ nm.

The effect of plasmon resonance splitting is also observed in the case of nanoplatelets, i.e., nanoparticles of an oblate geometric shape. Figure 5 illustrates this with examples of a nanodisk (red dashed curve *2*) and a triangular nanoprism (green dashed-dotted curve *5*), both having two pronounced spectral peaks in their optical spectra. Thus, by varying the particle shape, it is possible to shift the positions of the plasmon resonance peak into a given wavelength range. This specific feature of plasmonic nanoparticles is very attractive for the development of nanostructures and nanomaterials with desired optical properties.

As noted above, the splitting of the longitudinal and transverse resonances in structures of elongated and oblate shapes is already observed even for small-sized nanoparticles for which the quasistatic approximation is definitely justified, i.e., even when the peaks of the multipole resonances ($n > 1$) do not yet make a noticeable contribution to the light extinction and scattering cross sections. However, a significant increase in the particle size in at least one direction leads to the inapplicability of the quasistatic approximation. Then for a correct description of the optical spectra, it is also necessary to take into account the contributions of higher-order multipoles (quadrupole, octupole, etc.) on top of the contribution of the electric dipole term. Therefore, for a rod of a nanometer transverse diameter D and a large longitudinal size L, exceeding the de Broglie wavelength of light, $\lambda\!\!\!^{-} = \lambda/(2\pi)$, the behavior of the extinction spectra becomes more complicated. This is clearly demonstrated in experiments [176] for gold nanorods with a narrow size distribution in heavy water. Measurements were performed in the visible and near-IR regions of the spectrum in the range of $400 \lesssim \lambda \lesssim 2000$ nm. The diameter of the rods in [176] was $D = 85$ nm, and the length reached $L = 1175$ nm. In a number of works, calculations of the optical spectra of micrometer-sized nanoparticles of various elongated and oblate shapes took into account nth order multipole contributions ($n > 1$) [177–179].

3. Ordered molecular aggregates of organic dyes

3.1 Formation of molecular aggregates and simple excitonic model

3.1.1 Types of molecular packing in aggregates. Molecular J-aggregates are nanoclusters of noncovalently bound organic molecules in which the intermolecular interaction is significantly weaker than the intramolecular interaction. The monomer molecules in such a complex retain their individuality to a great extent, so that collective electronic excitations of the entire system can be correctly described in terms of small-radius excitons (Frenkel excitons) [180]. It is very important that the excitation localized on a specific molecule, due to the presence of translational symmetry and intermolecular coupling, not be stationary and that it begin to travel throughout the aggregate. In contrast, the stationary excitation of an aggregate is delocalized, being a superposition of localized exciton states, with the coherence region covering the entire ordered aggregate [180, 181].

The most studied aggregates are those of polymethine (cyanine) dyes. Frequently used cyanine dyes are described by the structural formula (Fig. 6a), according to which they are cationic chromophores with heterocyclic nuclei (based on benzoxazole, benzthiazole, benzimidazole, and quinoline) linked by a polymethine chain containing an odd number of methine groups [182]. Their compounds absorb light excellently in the visible and near-IR spectral regions due to the alternation of the signs of the π-charges along the chromophore chain and their change to the opposite ones upon excitation by external radiation. The molar extinction coefficients reach values of $\epsilon = (2-3)\times 10^5$ l mol^{-1} cm^{-1}, which correspond to absorption cross sections of $\sigma = (3-5)\times 10^{-16}$ cm^2.

Basically, the molecules of cyanine dyes are almost flat with angles of less than 15° between the planes of heterocycles. For this reason, cyanine dyes are inclined to form aggregates having a 'plane-to-plane' structure with a shift of molecules relative to each other for optimal π–π-charge interaction of oppositely charged methine groups of neighboring molecules. Aggregates of cyanine dyes are formed in solutions [54]; on crystal surfaces, including metal substrates [96, 97]; on the surfaces of metal nanoparticles [68, 174, 183, 184]; and on anionic platforms of magnesium dye complexes [61, 62]. They can also assemble on DNA templates [185]. In addition, dye aggregates can grow along polymer threads and be embedded in polymer matrices [186].

Depending on the concentration, dyes in solutions can exist in the forms of monomers M, dimers D, and J- and H-aggregates (see Fig. 6). When the concentration of the solution increases and it is cooled, the dye first dimerizes, and then H- or J-aggregates are formed from the dimers in accordance with the 'block' construction mechanism [53, 187]. Thus, the simplest aggregate consists of two dimers (four monomers). However, at present, it is aggregates of a large number of monomers that are of significant interest for many practical applications, so that the length and width of the supramolecular system can range from 1 μm to 300 μm and from 100 nm to 1 μm, respectively [61]. The characteristic thicknesses of the J-aggregate layers can vary greatly. For example, on the surfaces of metal nanoparticles, the thickness usually ranges from 0.5–1 nm [174] to 3–5 nm [113], while the layers on metal films reach a thickness of about 10–20 nm [183].

The main physical properties of aggregates are determined by the type of molecular packing [53]. The most studied is the brickwork-type packing of linear and planar aggregates [188]. Other well-known types of packing are the 'ladder' and 'deck of cards'. Recently, the main focus in the studies of molecular aggregates has shifted towards supramolecular assemblies with a more complex geometric structure. For example, there have been many works on tubular [189] and columnar [59] aggregates, cross-stacked aggregates (X-aggregates) [60], and helical nanofibers [190]. In this review, we present only a number of basic results and theoretical treatments of the simplest linear aggregates with one molecule in the unit cell, because this review is aimed at the discussion and analysis of the most prominent results in

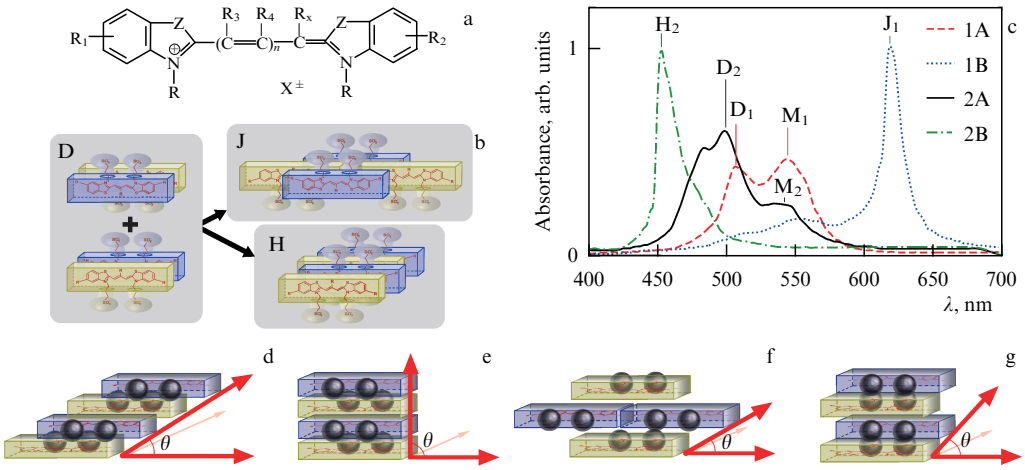

Figure 6. Structure and spectra of molecular aggregates of dyes: (a) typical structural formula of cyanine dye [182]; Z can be O, S, Se, NR, –CH = CH–, etc.; R, R_1-R_x are various substituents; *n* can take values from 0 to 7; $X^{\pm}$ is a counterion. (b) Pathways of formation of J- and H-aggregate blocks (J and H) from dye dimers (D). (c) Absorption spectra of an aqueous solution of *meso*-ethyl-substituted thiatrimethine cyanine (1A) and (1B) and *meso*-methyl-substituted thiatrimethine cyanine (2A) and (2B) [187]. Curves (1A) and (2A) and curves (1B) and (2B) show both compounds before and after aggregation, respectively. Vertical lines and designations near them in figure (c) indicate positions of peak maxima corresponding to different forms of the dye in solution: monomers, M; dimers, D; and J- and H-aggregates. Spectra (1A) and (1B) are normalized to maximum of J-band of the aggregate, and spectra (2A) and (2B) are normalized to maximum of H-band of the aggregate. (d–g) Types of molecular packing in aggregates: (d) 'staircase,' (e) 'deck,' (f) 'brickwork,' and (g) 'ladder.'

the optics of plexcitonic systems. Most of the experimental and theoretical work in this field is devoted to the study of hybrid metalorganic nanoparticles and nanostructures, containing the conventional J-aggregates of cyanine dyes as their organic component.

3.1.2 Dispersion relation for simplest aggregates. Now we come to the basic aspects of delocalized Frenkel excitons [181, 191] using the example of conventional J- and H-aggregates within the framework of the simple McRae–Kasha model [192–194] based on the point dipole–dipole interaction between monomer molecules. In this model, vibronic and charge transfer effects are neglected, and in the potential interaction energy the predominant contribution of the nearest neighbors only is taken into account. Thus, the energy of intermolecular interaction, which largely determines the behavior of the optical spectra of aggregates, can be expressed as

$$U_{\rm dd} = \frac{\mathbf{d}_1\mathbf{d}_2 - 3(\mathbf{d}_1\mathbf{n})(\mathbf{d}_2\mathbf{n})}{r^3}\,, \tag{14}$$

where $\mathbf{d}_1$ and $\mathbf{d}_2$ are the transition dipole moments of molecules '1' and '2,' and $\mathbf{n} = \mathbf{r}/r$, $\mathbf{r}$ is the displacement vector connecting their centers of mass.

To derive the dispersion law of excitons and calculate the optical spectra of aggregates, it is necessary to perform a basis transformation from the localized to delocalized states of Frenkel excitons (see, for example, [181]). More specifically, the basic concepts of the theory of molecular excitons can be formulated as follows: (1) any state of a molecular aggregate is represented as a product of the eigenstates of its constituent molecules; (2) the localized excited state of an individual monomer transfers to other molecules (mainly to its nearest neighbors) via dipole–dipole interaction; and (3) due to the presence of translational symmetry of the aggregate, its eigenstate is represented as a coherent superposition of local excitations.

For conventional linear aggregates with one molecule per unit cell ($|\mathbf{d}_1| = |\mathbf{d}_2| \equiv d$), containing N molecules in total, these considerations lead to the dispersion relation [181, 192]

$$\mathcal{E}_q(\theta) = \mathcal{E}_{\rm M} + \mathcal{D} + 2\mathcal{U}_{\rm dd}(1-3\,\cos^2\theta)\cos(ql)\,, \quad \mathcal{U}_{\rm dd} = \frac{d^2}{l^3}\,. \tag{15}$$

Here, q is the wave number of an exciton, θ is the angle between the transition dipole moment of the monomer and the aggregate axis, $\mathcal{E}_{\rm M}$ is the transition energy in an isolated monomer molecule, and $\mathcal{D}$ is the gas-to-crystal shift determined by a change in the energy of electrostatic interaction of the monomer with the environment and other aggregated molecules upon the local excitation [181]. The parameter $\mathcal{U}_{\rm dd}$ determines the scale of the dipole–dipole coupling between the nearest neighbors; the value of l corresponds to the distance r between the centers of neighboring molecules in formula (14) .

A discrete set of possible values of the exciton wave number $q \equiv q_j$ appears in formula (15) due to the finite size of the linear aggregate and is determined by the expression $q_j = \pi j/[l(N+1)]$, where j is the excitonic state number ($j = 1, \ldots, N$). According to the terminology accepted in the theory of molecular aggregates, such values of q_j correspond to so-called open boundary conditions (see, for example, [195]). Thus, the energy width of the excitonic band is given by

$$W_{\rm ex} = 4\mathcal{U}_{\rm dd}|1-3\cos^2\theta|\cos\left(\frac{\pi}{N+1}\right), \tag{16}$$

and the energy positions of its top and bottom can be written as

$$\begin{aligned}\mathcal{E}_{\rm top}(\theta) &= \mathcal{E}_{\rm M} + \mathcal{D} + \frac{W_{\rm ex}}{2},\\ \mathcal{E}_{\rm bottom}(\theta) &= \mathcal{E}_{\rm M} + \mathcal{D} - \frac{W_{\rm ex}}{2}\,.\end{aligned} \tag{17}$$

Note that dispersion relation (15) is applicable to linear aggregates with one molecule per unit cell. Such a structure is seen, for example, in aggregates of cyanine dyes as TC, OC, Thia(Et), and TDBC (Table 2), which were widely used as an organic component in 'core–shell' plexcitonic systems. For aggregates with a more complex geometric shape, the structure of the excitonic band is significantly more complex and, as a rule, is determined by numerical simulation. Nevertheless, for linear aggregates with two molecules per unit cell, the dispersion relation can be presented in analytical form [197, 198].

Optical properties of molecular aggregates are determined to a great extent by the structure of their excitonic band. For

Table 2. Abbreviations, names, and positions of spectral peaks and their full widths at half maximum (FWHM) for a number of dye J-aggregates according to data from papers [64, 68, 87, 88, 153, 174, 196, 322, 323].

Abbreviation	Dye	$\hbar\omega_{\rm ex}$, eV	$\lambda_{\rm ex}$, nm	$\gamma_{\rm ex}$, meV (FWHM)
OC	3,3′-disulfopropyl-5,5′-dichlorooxacyanine triethylammonium salt	3.04	407	39
TC	3,3′-disulfopropyl-5,5′-dichlorothiacyanine sodium salt	2.61	475	66
PIC	1,1′-disulfopropyl-2,2′-cyanine triethylammonium salt	2.13	582	33
TDBC	5,5′,6,6′-tetrachloro-1-1′-diethyl-3,3′-di(4-sulfobutyl)-benzimidazolo-carbocyanine	2.12	585	48
NK2567	2,2′-dimethyl-8-phenyl-5,5′,6,6′-dibenzothiacarbocyanine chloride	1.79	693	52
D725	3,3′-di(g-sulfopropyl)-6,6′-dimethoxy-8,10-dimethylene thiacarbocyanine betaine triethylammonium salt	1.71	725	13
JC1	5,5′,6,6′-tetrachloro-1,1′,3,3′-tetraethylimidacarbocyanine iodide	2.09	592	28
TPP	5,10,15,20-tetraphenyl-21H,23H-porphyrin	2.82	440	90
Thia(Et)	3,3′-disulfopropyl-5,5′-dichloro-9-ethylthiacarbocyanine potassium salt	2.00	621	67
Thia(Ph)	3,3′-disulfopropyl-5,5′-dichloro-9-phenylthiacarbocyanine triethylammonium salt	1.85	671	85

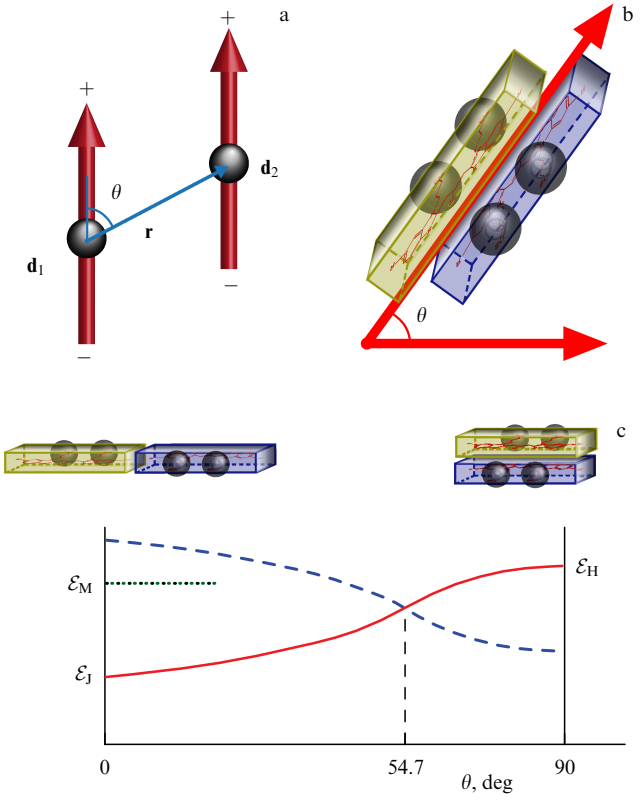

Figure 7. (a) Schematic view of a dye dimer as point-like dipoles; r is distance between dipoles, $|\mathbf{d}_1| = |\mathbf{d}_2| \equiv d$ is magnitude of transition dipole moment in monomer molecule, and θ is angle between directions of transition dipole moments $\mathbf{d}_1$ and $\mathbf{d}_2$ and aggregate axis. (b) Relative positions of monomer molecules in dimers that constitute dye aggregates. (c) Dependence of phototransition energies of dye dimers on angle θ. Red solid and blue dashed curves show energies of allowed and forbidden phototransitions to edges of excitonic band, respectively. Green dotted horizontal line is energy $\mathcal{E}_M$ of excited state of the monomer. J-aggregates are formed at $\theta < \theta_m$, and H-aggregates are formed at $\theta_m < \theta < \pi/2$ ($\theta_m = 54.7°$ is the magic angle).

the considered linear aggregates, the sign of the excitonic coupling energy, U_{dd}, of dye molecules plays a key role. Thus, in the case of negative coupling energy ($U_{dd} < 0$), a J-aggregate is formed, and the most efficient radiative transition occurs to the bottom of the excitonic band, while the transition to the top of the band is forbidden. In contrast, in the case of positive coupling energy ($U_{dd} > 0$), an H-aggregate is formed, and the transition to the bottom of the band is forbidden, while the transition to the top of the band is the most intense. Correspondingly, in J-aggregates, the main peak in the absorption spectrum shifts to the red region and undergoes a substantial narrowing compared to the spectrum of the monomer. On the contrary, for H-aggregates, the spectral maximum shifts to the blue region relative to the monomer, and the band width is usually substantially larger compared to the typical width of the J-aggregate spectral band. However, in some cases, the H-aggregate band is not much wider than the J-aggregate band. This is shown, for example, in Fig. 6c, when these two types of molecular aggregates are formed from the same dye.

It is important to note that the exciton dispersion law (15), derived for the simplest case of a linear aggregate with one molecule in the unit cell, is suitable for describing two possible types of aggregation (J and H). Moreover, expression (15) clearly shows that the aggregation type (J or H) and the corresponding qualitative behavior and quantitative characteristics of the optical spectrum depend directly on the angle θ, which specifies the orientation of the transition dipole moments relative to the axis connecting the centers of neighboring molecules (Fig. 7a). The condition $U_{dd} = 0$ yields the so-called magic angle, $\theta_m = \arccos(1/\sqrt{3}) = 54.7°$, separating the J- and H-types of aggregation (Fig. 7c). In J-aggregates, the molecules are packed in a 'head-to-tail' arrangement with the orientation angle of the transition dipole moments in the range $0 \leqslant \theta < \theta_m$. In this case, the dipole–dipole coupling energy (14) is negative ($U_{dd} < 0$). In contrast, H-aggregates have a side-by-side packing with orientation angles of the transition dipole moments in the range $\theta_m < \theta \leqslant \pi/2$, resulting in a positive sign of the interaction energy ($U_{dd} > 0$).

3.1.3 Photoluminescence and photoabsorption. The probabilities of radiative decay per unit time differ greatly for J- and H-aggregates. For a J-aggregate consisting of N molecules, the rate of spontaneous decay increases by a factor of N compared to the case of a monomer (superradiance effect [199]). In contrast, in H-aggregates, after light absorption, rapid intraband relaxation occurs, leading to the effective population of the state with the lowest energy, with the dipole transition to this state being forbidden. Regarding the quantum yield of luminescence, we note that its value in J-aggregates is typically large, while in H-aggregates, it is usually small. Nevertheless, there are fluorescent H-aggregates [200, 201], in which the low rate of radiative decay dominates over the even slower rate of nonradiative decay, leading to a fairly high quantum yield.

Further, we present the analytical expression for the absorption coefficient of light, K_q, of a linear aggregate with one molecule per unit cell on an individual transition from its ground state $|g\rangle$ to a given exciton state $|e_q\rangle$ with wave number q. It was recently obtained [197, 198] within the framework of the McRae–Kasha model [192] and can be written as

$$K_q = N_{aggr} \frac{\pi^2 d^2}{\hbar\omega c} \mathcal{E}_q^2(\theta) \left(1 + \frac{1}{2}\cos^2\theta\right) f_N(ql)\, a_q(\omega)\,, \tag{18}$$

$$f_N(ql) = \begin{cases} \dfrac{2}{N+1}\cot^2\left(\dfrac{ql}{2}\right), & j = 1,\ 3,\ 5,\ \ldots\,, \\ 0, & j = 2,\ 4,\ 6,\ \ldots \end{cases} \tag{19}$$

Here, N_{aggr} is the concentration of aggregates in the ground state, N is the number of molecules in the aggregate, ω is the photon frequency, and c is the speed of light. Possible values of q determined from open boundary conditions are $q \equiv q_j = \pi j/[l(N+1)]$, where j is the excitonic state number ($j = 1, \ldots N$); l is the unit cell length; and $a_q(\omega)$ is the contour of the resonance spectral band normalized by the relation $\int a_q(\omega)\, d\omega = 1$, with a maximum at $\hbar\omega = \mathcal{E}_q(\theta)$. Formula (18) is averaged over the directions of the incident light polarization.

In [197, 198], formula (18) was extended to linear aggregates with two monomer molecules in a nonplanar unit cell. In addition, expressions were obtained for the coefficient of polarized light absorption by aggregates with a given axis orientation on a substrate or inside a flow-through cuvette. The resulting coefficient, $K_{tot}(\omega) = \sum_q K_q(\omega)$, of light absorption at frequency ω by a molecular aggregate is determined by the sum over transitions $|g\rangle \to |e_q\rangle$ to all

possible states of the excitonic band $|e_{q_j}\rangle$ (j=1, ..., N). Transitions to excitonic states with the lowest wavenumber q make the most of the contribution to the resulting absorption coefficient.

The above excitonic approach, based on the works by Frenkel [180], Davydov [181], and McRae and Kasha [192–194], turned out to be successful for the classification and reasonable explanation of the photophysical properties of a number of experimentally studied dye aggregates. Its further development is associated with the generalization of the simplest model of point dipole–dipole interaction as a result of a more accurate consideration of the effects of long-range and short-range interactions between molecules [57, 202, 203], as well as with the inclusion of vibronic coupling and intermolecular charge transfer effects in the theory [57, 189, 202, 204]. A variety of molecular packing types in ordered aggregates of various shapes and topologies have been considered in the literature, including two-dimensional 'herringbone' and 'HJ' aggregates and various tubular, columnar, and helical structures. It is then possible to explore a wide range of new photophysical and photochemical phenomena (see [61, 203, 205, 206], as well as reviews [53–60] and the references therein). Their detailed discussion is beyond the scope of this review.

3.1.4 Nonlinear optical properties. In Section 3.1.3, the optical properties of molecular J-aggregates, which manifest themselves at relatively low densities of electromagnetic excitation energy, were discussed. At the same time, as has been established in several studies [207–216], molecular aggregates have extremely high resonant nonlinear optical susceptibilities and picosecond-scale relaxation times of the nonlinear response when they are exposed to optical radiation. For example, for the resonant cubic susceptibility $\chi^{(3)}$ of molecular aggregates PIC-I (pseudoisocyanine iodide) characteristic values of $\chi^{(3)} \sim 10^{-9}$ cm^2 V^{-2} were obtained [217–219] based on data from z-scan experiments with nanosecond laser pulses. Such values of $\chi^{(3)}$ are record breaking among most organic and inorganic materials, including composite glasses; they are 5–6 orders of magnitude greater than those of polyconjugated polymers. Therefore, studies of various nonlinear optical effects involving J-aggregates were initially carried out given their fundamental significance and potential applications in photonics and optoelectronics, for example, for efficient and high-speed nonlinear optical switches. In addition, giant nonlinear optical susceptibilities of molecular aggregates were used in a number of works on nonlinear effects of their interaction with laser pulses of various time scales: from nanosecond [217–219] to femtosecond [220–235].

Specifically, the pump–probe technique was utilized to study the collective properties of multiexciton states in aggregates; four-wave mixing was used to investigate the coherence times of delocalized excitons [188, 236–238], and hole burning was used to identify the features of the hierarchical structure of cyanine dye aggregates [188, 239]. In recent years, two-dimensional electron spectroscopy has become an extremely efficient method for examination of supramolecular structures, including J-aggregates [227–235]. It is also appropriate to note a series of studies on the effects of the optical bistability of molecular aggregates [240–247] and composite metal/J-aggregate systems [248], since such effects are of certain interest in nonlinear optics and spectroscopy [249]. At the same time, despite the undoubted significance of these studies on the nonlinear optical properties of molecular aggregates of organic dyes, there have not been that many works on plexcitonic nonlinear effects in hybrid metalorganic nanostructures. In other words, plexcitonic nonlinear optics has not yet emerged as an separate extensive field, as is currently the case for the linear optics of systems involving metals and aggregates of organic dyes. Thus, the results of the above papers are not considered in detail in this review.

3.2 Dielectric properties of dye aggregates

3.2.1 Scalar model of excitonic shell. For a reliable analysis of the plexcitonic coupling effects in metalorganic nanostructures using classical electrodynamics, it is necessary to correctly describe the dielectric properties not only of their plasmonic but also of their excitonic components. Within the framework of the commonly used isotropic model, the local dielectric function of the J-aggregate shell of the dye is described in the Lorentz oscillator model,

$$\varepsilon_{\mathrm{J}}(\omega) = \varepsilon_{\mathrm{J}}^{\infty} + \frac{f\omega_{\mathrm{ex}}^2}{\omega_{\mathrm{ex}}^2 - \omega^2 - \mathrm{i}\omega\gamma_{\mathrm{ex}}} \,. \tag{20}$$

The parameters of the Lorentz countour of the J-band of a dye aggregate are determined experimentally; ω_{ex} is the transition frequency associated with the center of the J-band; γ_{ex} is the full width at half maximum (FWHM); and $\varepsilon_{\mathrm{J}}^{\infty}$ is the permittivity at frequencies far from the absorption J-band. The dimensionless quantity f in formula (20) is the effective oscillator strength, which reflects the resonant contribution of the J-band of the dye to the dielectric properties of the excitonic shell. According to Wooten [250], the value of f is proportional to the concentration of the dye molecules. In a series of papers on excitonic and plexcitonic topics, this value is also referred to as the reduced oscillator strength or strength of resonance. The center position and width of the J-band included in formula (20) are given in Table 2 for a number of dyes. Note that the values of the effective oscillator strength, f, and the constant, $\varepsilon_{\mathrm{J}}^{\infty}$, reported by different authors for J-aggregates of the same dyes, sometimes differ greatly from each other.

Individual dye aggregates usually exhibit optical anisotropy, and their polarizability is of a tensor nature. However, when a material consists of many randomly oriented aggregates, its macroscopic permittivity no longer exhibits orientational effects. In this case, the isotropic model (20) can be appropriate for describing the spectra of dye J-aggregates. To obtain more accurate results in a wide spectral range and to correctly reproduce the asymmetry of the left and right wings of the absorption J-band (Fig. 6c), the imaginary part of the dielectric function of J-aggregates can be restored from experimental data on the light extinction spectra, and its real part can be calculated using the Kramers–Kronig relation.

The coupling regime of the Frenkel exciton in the J-aggregate shell and the surface plasmon-polariton in the metal core of a metal/J-aggregate nanoparticle depends essentially on the optical constants of its constituent materials, as well as on the relationship between the frequency of the incident light and the resonance frequencies of the studied system. Therefore, one of the most important physical parameters determining the coupling regime is the spectral detuning between the center of the absorption J-band of the excitonic shell (ω_{ex}) and the peak maximum of the plasmon resonance of the metal core (ω_{pl}). To demonstrate the considerably different relative positions of the exciton and

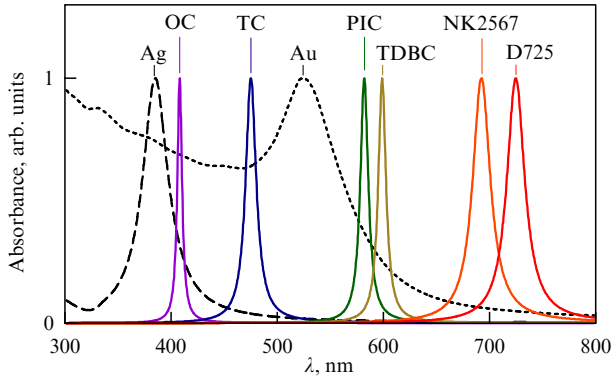

Figure 8. Normalized photoabsorption J-bands (solid curves) of aggregates of dyes OC, TC, PIC, TDBC, NK2567, and D725, calculated within the framework of scalar Lorentzian model (20) with parameters taken from papers [64, 68, 87, 88, 174, 322]. Dashed curves show absorption spectra of silver and gold spherical nanoparticles with radius $r = 10$ nm in an aqueous solution, calculated within the framework of Mie theory.

plasmon peaks, Fig. 8 shows the normalized absorption peaks for J-aggregates of several common dyes together with the peaks of plasmon resonances of silver and gold nanospheres with a radius of $r = 10$ nm. Such dye J-aggregates are listed in Table 2, complete with their names, abbreviations, maxima positions, and full widths of spectral peaks. Note that, for those dyes (e.g., PIC and TPP) whose J-aggregates have several peaks in the visible and near-IR ranges, Table 2 presents the parameters for the most intense of them.

3.2.2 Tensor model of excitonic shell. In many situations, it is fundamentally imperative to take into account anisotropic and orientational effects in molecular aggregates to correctly describe the behavior of their optical spectra. As was recently shown in Refs [251, 252], the pronounced tensor nature of the permittivity of dye aggregates also becomes crucial in exploring plexcitonic effects in hybrid metalorganic nanosystems. In other words, to include anisotropic and orientational effects of the outer excitonic shell in the theoretical description of optical properties of metal/J-aggregate and metal/spacer/J-aggregate nanoparticles, its local dielectric function should be substantially modified from expression (20). Thus, the dielectric function of the aggregate should be represented in tensor form and take into account the more complex nature of the J-band, in particular, the presence of several resonance peaks with a specific polarization. If the molecular aggregates in the outer shell have a favored direction of their orientation on the nanoparticle surface (Fig. 9), the tensor components of the dielectric function of the organic shell should be described as the sum of Lorentzians [251]

$$\varepsilon_{(\parallel,\perp)}(\omega) = \varepsilon^{\infty}_{(\parallel,\perp)} + \sum_n \frac{f_n^{(\parallel,\perp)} (\omega_n^{(\parallel,\perp)})^2}{(\omega_n^{(\parallel,\perp)})^2 - \omega^2 - \mathrm{i}\omega\gamma_n^{(\parallel,\perp)}} \,. \quad (21)$$

Here, the tensor components $\varepsilon_{\parallel}$ and $\varepsilon_{\perp}$ correspond to the directions parallel (*longitudinal* component) and perpendicular (*transverse* component) to the axis of the aggregate orientation. The parameters in (21) are chosen based on the measured absorption spectra of the J-aggregate, as described in [251].

According to [251], the most appropriate explanation of some available experimental data can be given by considering

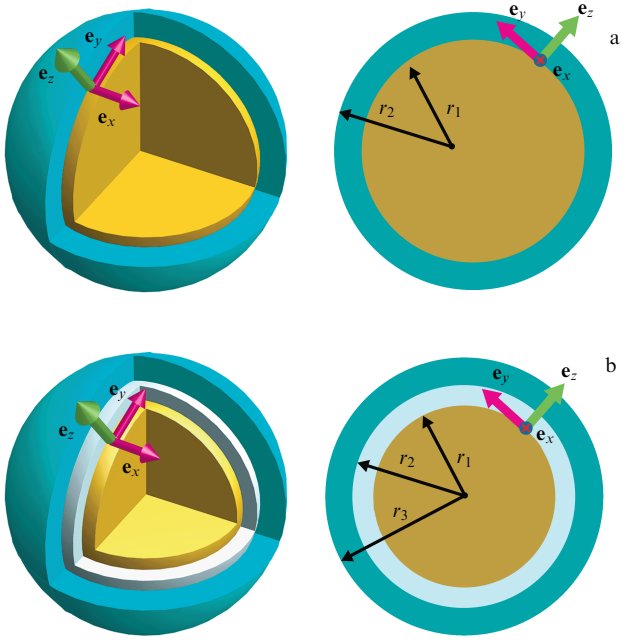

Figure 9. Schematic view of two-layer and three-layer nanospheres: (a) particle with a metal core coated with J-aggregate shell of dye; r_1 is radius of core and r_2 is radius of outer shell; (b) particle with a metal core, passive dielectric spacer layer, and outer J-aggregate shell; r_1 is radius of core, r_2 is radius of spacer shell ($\ell_s = r_2 - r_1$ is thickness of spacer layer), r_3 is radius of outer shell ($l_J = r_3 - r_2$ is thickness of J-aggregate layer).

the following possible arrangements of molecules in the J-aggregate shell: (1) *normal* orientation of aggregates, when their axes are directed along the normal to the nanoparticle surface (i.e. along the unit vector $\mathbf{e}_z$ in Fig. 9); (2) *tangential* orientation of aggregates, when their axes lie in the tangent plane to the nanoparticle (i.e. in the plane formed by the unit vectors $\mathbf{e}_x$ and $\mathbf{e}_y$) but do not have any particular direction in this plane; and (3) *equiprobable* orientation of the aggregate axis in space. In these three cases, the dielectric functions are described by tensors whose form is obtained by appropriate averaging over the possible directions of the J-aggregate axis. Provided that the tensor components are oriented along the $\mathbf{e}_x$, $\mathbf{e}_y$, and $\mathbf{e}_z$ axes (see Fig. 9), the resulting expressions for the dielectric tensors take the form

$$\hat{\varepsilon}_{\mathrm{norm}} = \begin{pmatrix} \varepsilon_{\perp} & 0 & 0 \\ 0 & \varepsilon_{\perp} & 0 \\ 0 & 0 & \varepsilon_{\parallel} \end{pmatrix},$$

$$\hat{\varepsilon}_{\mathrm{tang}} = \begin{pmatrix} \frac{1}{2}\varepsilon_{\parallel} + \frac{1}{2}\varepsilon_{\perp} & 0 & 0 \\ 0 & \frac{1}{2}\varepsilon_{\parallel} + \frac{1}{2}\varepsilon_{\perp} & 0 \\ 0 & 0 & \varepsilon_{\perp} \end{pmatrix}, \quad (22)$$

$$\hat{\varepsilon}_{\mathrm{epo}} = \begin{pmatrix} \frac{1}{3}\varepsilon_{\parallel} + \frac{2}{3}\varepsilon_{\perp} & 0 & 0 \\ 0 & \frac{1}{3}\varepsilon_{\parallel} + \frac{2}{3}\varepsilon_{\perp} & 0 \\ 0 & 0 & \frac{1}{3}\varepsilon_{\parallel} + \frac{2}{3}\varepsilon_{\perp} \end{pmatrix}.$$

To compare our calculations [251] with those obtained using conventional isotropic theoretical models, one more case (4) should be considered. It corresponds to a fully *isotropic* J-aggregate shell described by the scalar expression (20) for a

single excitonic peak or its direct generalization,

$$\varepsilon_{\rm iso}(\omega) = \varepsilon_{\rm J}^{\infty} + \sum_n \frac{f_n \omega_n^2}{\omega_n^2 - \omega^2 - {\rm i}\omega\gamma_n}\,, \qquad (23)$$

taking into account the presence of multiple absorption bands present in a number of aggregates.

Importantly, the choice of scalar or tensor models corresponding to one or another orientation of the molecular aggregate in the outer shell is primarily determined by the physicochemical properties of the surface on which aggregation occurs, i.e., a metal or an organic spacer layer. Most calculations and theoretical analysis of optical properties of hybrid plexcitonic metal/J-aggregate and metal/spacer/J-aggregate nanosystems were performed using a scalar isotropic model (23) to describe the permittivity of the outer shell of the dye. However, recent studies [251, 252] clearly point to the importance of using tensor models of the permittivity of aggregates to explain and describe quantitatively the available experimental data.

4. Summary of theory of light absorption and scattering by hybrid nanostructures

4.1 Physical approaches to description of plexcitonic coupling

Physical interpretation of the plexcitonic coupling effects in hybrid nanostructures that include metal and excitonic subsystems is usually given within the framework of classical or semiclassical approaches. In classical electrodynamics, these subsystems are treated using the dielectric functions of the corresponding materials, written, for example, using the Drude and Lorentz models. The theoretical basis for calculating optical spectra and explaining various phenomena caused by the electromagnetic coupling of surface plasmons with excitons in organic and inorganic components of hybrid nanostructures are solutions to Maxwell's equations. A notable example here is the analytical solution to the problem of scattering and absorption of a plane electromagnetic wave by a multilayer concentric sphere (extended Mie theory). Additionally, numerical solutions obtained by the FDTD method or other computer simulation techniques are available for composite nanostructures of arbitrary shape.

For composite nanosystems containing metals as a plasmonic subsystem and organic materials (e.g., J-aggregates) as an excitonic subsystem, the classical approach provides a reliable self-consistent explanation for the main phenomena observed in experiments to date. These include, in particular, the resonance and antiresonance phenomena during the interaction of an exciton with dipole and multipole plasmons, the effects of a deep dip in the light absorption spectra, and the replication of spectral bands of plexcitonic nanoparticles and their dimers. Although these phenomena are traditionally interpreted using the terms 'plasmons' and 'excitons,' it is not formally required to describe quasiparticles within the framework of the classical electrodynamic approach. However, since the terms 'plasmon' and 'exciton' are well justified from a physical point of view, their use remains valid even within a purely classical approach. Recently, the term 'plexciton' has come into use, referring to a hybrid quasiparticle.

In classical electrodynamics, the phenomenon of plasmon-exciton coupling can be interpreted as follows. The electric and magnetic fields in each component of the plexcitonic system obey the known boundary conditions for Maxwell's equations. Therefore, the spatial distributions of these fields in both the plasmonic and excitonic subsystems are determined by the geometrical structure and material permittivity of both of them. Plexcitonic coupling arises due to the dependence of the distribution of the fields in the plasmonic subsystem on their distribution in the excitonic subsystem and vice versa. In other words, new hybrid normal modes of field oscillations arise in the system with eigenfrequencies that differ from those of the individual plasmon and exciton resonances. In the simplest case of a two-layer spherical 'core–shell' particle of a small radius, $r \ll \lambda$, the interaction between a dipole plasmon resonance with a frequency of $\omega_{\rm pl}^{\rm (dip)}$ and an excitonic resonance with a frequency of $\omega_{\rm ex}$ results in two new normal modes with ω_+ and ω_- frequencies emerging in the system. The difference between the frequencies of the new normal modes, ω_+ and ω_-, determines the effective constant g of the plexcitonic coupling. The value of g drastically affects the behavior of the optical spectra of hybrid systems containing plasmons and excitons. This corresponds to qualitatively different regimes of near-field plexcitonic coupling: weak, strong, and ultrastrong. Plexcitonic coupling has a near-field nature, because its efficiency rapidly decreases with increasing distance ℓ between the metal (plasmonic) and organic molecular (excitonic) components.

In the theory of plexcitonic coupling, the semiclassical approach is also quite common. In this approach, the excitonic subsystem is described as a quantum-mechanical two-level or multilevel system [253, 254], while the electromagnetic field and the plasmonic subsystem are treated in a conventional classical way. The essence of the semi-classical approach in application to plexcitonic problems is most clearly outlined in review [141] using the example of the propagating surface plasmon-polariton interacting with a set of two-level quantum emitters. In the semiclassical approach, the polarization of the excitonic material is expressed through the mean value of the dipole moment operator of its constituent particles (organic molecules or quantum dots). As a result, it becomes possible to describe the dynamics of a quantum emitter interacting not only with fairly weak fields, but also with a strong local field. This allows one to include nonlinear optical effects in the theory [249]. Thus, with the semiclassical theory it is possible to go beyond the scope of linear electrodynamics and describe the dependence of the optical response of a plexcitonic system on the incident light intensity.

The authors of Ref. [141] also discussed the next step toward a quantum description of plexcitonic systems, in which the electromagnetic field is treated on the basis of secondary quantization formalism using photon creation and annihilation operators. For such systems, this approach, in which the field and emitters are quantized, remains essentially semiclassical, since the plasmonic subsystem is still considered at the classical level. Herewith the entire ensemble of quantum emitters constituting the excitonic subsystems is considered as a unified many-particle quantum system interacting with the quantized electromagnetic field. Within the framework of such a description of the exciton–polariton interaction, splitting of the hybrid modes occurs in the plexcitonic system even in the absence of photons, in line with vacuum Rabi splitting in quantum optics (see [141] for more details).

Within the framework of a consistent quantum approach, it is necessary to quantize all three subsystems of the hybrid system (plasmonic, excitonic, and electromagnetic field). In this case, a self-consistent description of plexcitonic effects can be given by using general methods developed in the field of quantum statistical physics and the physical kinetics of open systems. There are several fundamental approaches to solving many-body problems, including those based on the methods of quantum field theory [255] and on generalizations of the Bogoliubov hierarchy (Bogoliubov–Born–Green–Kirkwood–Yvon hierarchy, BBGKY) [256]. However, applying such general quantum approaches to the description of plexcitonic phenomena requires solving extremely complicated systems of equations, which significantly limits their applicability to solving specific problems in the physics of plexcitonic systems. Some attempts to apply quantum methods to study of the coupling effects between plasmonic and excitonic subsystems (such as molecules or quantum dots) were made in [112, 257]. The theoretical consideration in these works was carried out within the framework of the formalism of Zubarev's Green's functions [258], but some of the essential parameters of the system were chosen empirically rather than obtained by direct calculations. The authors of Ref. [112] calculated the light absorption spectra of two different plexcitonic systems: (a) a quantum emitter located near a metal nanoparticle, and (b) a metal dimer with a quantum emitter placed in its gap. Similarly, the authors of Ref. [257] calculated the photoabsorption spectra of a quantum emitter near a metal dimer at different temperatures.

It is important to note here that most of the available experimental data on the optics and spectroscopy of hybrid metalorganic nanostructures pertain to the range of problems for which the use of a purely classical electrodynamic approach is quite sufficient. Therefore, below, we briefly outline the Mie theory extended to the case of two-layer, three-layer, and multilayer concentric spheres. We also list efficient numerical methods used in specific calculations of optical absorption, scattering, and extinction spectra in metal/J-aggregate and metal/spacer/J-aggregate systems. We also present simple formulas of the quasistatic approximation applicable for explaining the corresponding experimental data for spherical 'core–shell' particles of small radii.

4.2 Extended Mie theory for multilayer spherical particles

For hybrid nanoparticles with a metal core whose size exceeds the Fermi wavelength of an electron in a metal, $\hat{\lambda}_F \sim 1$ nm, a reliable quantitative description of the light absorption and scattering spectra can be given within the framework of classical electrodynamics of continuous media. For the simplest geometry, using local dielectric functions of the constituent materials of the particle, an exact solution to the problem of absorption and scattering of light is a generalization of the standard Mie theory for a homogeneous sphere to the case of multilayer concentric spheres. This approach was developed in a series of works [259–266]. At first, the standard Mie theory was extended to the case of particles with one additional outer layer. A generalization to an arbitrary number of layers was performed in [264] using the matrix formalism and in [265, 266] based on recurrence relations for the coefficients of light scattering by a multilayer spherical particle.

Figure 9a shows a schematic view of a hybrid particle consisting of a core of radius r_1 and a shell of thickness $l = r_2 - r_1$ surrounded by a passive medium with permittivity $\varepsilon_h(\omega)$ and magnetic permeability $\mu_h = 1$. The materials composing concentric spherical layers are assumed to be homogeneous and isotropic with complex frequency-dependent dielectric functions $\varepsilon_1(\omega)$ and $\varepsilon_2(\omega)$ and magnetic permeabilities $\mu_1 = \mu_2 = 1$. A linearly polarized plane monochromatic wave $\propto \exp(-i\omega t + ik_h z)$ is incident on the particle. The incident wave is partially scattered and absorbed by the particle.

The resulting exact expressions for the cross sections of absorption σ_{abs}, scattering σ_{scat}, and extinction σ_{ext} of light from a multilayer spherical particle, applicable for an arbitrary ratio between the wavelength and its total radius, can be represented, as in the case of a homogeneous sphere [267], as series expansions in multipoles:

$$\sigma_{abs} = \frac{\pi}{2k_h^2} \sum_{n=1}^{\infty} (2n+1)\left(2 - |2a_n - 1|^2 - |2b_n - 1|^2\right), \quad (24)$$

$$\sigma_{scat} = \frac{2\pi}{k_h^2} \sum_{n=1}^{\infty} (2n+1)\left(|a_n|^2 + |b_n|^2\right), \quad (25)$$

$$\sigma_{ext} = \frac{2\pi}{k_h^2} \sum_{n=1}^{\infty} (2n+1)\,\mathrm{Re}\left\{a_n + b_n\right\}. \quad (26)$$

Here, a_n and b_n are the expansion coefficients of the transverse electric (TE) and transverse magnetic (TM) modes of the scattered wave, respectively; n is the order of the multipole; and $k_h = \omega\sqrt{\varepsilon_h}/c$ is the modulus of the wave vector of light in the medium surrounding the particle.

The expansion coefficients a_n and b_n in formulas (24)–(26) are determined by the specifics of the problem and depend on the geometric parameters of the hybrid particle and on the values of the permittivities of the materials that make it up. In the case of two-layer spherical 'core–shell' nanoparticles, the general expressions for the complex expansion coefficients a_n and b_n can be written as

$$a_n = -\frac{X_n^{(a)}}{Y_n^{(a)}}, \qquad b_n = -\frac{X_n^{(b)}}{Y_n^{(b)}}, \quad (27)$$

where the functions and $X_n^{(a)}$, $Y_n^{(a)}$ and $X_n^{(b)}$, $Y_n^{(b)}$ can be compactly expressed through the determinants [89]. For the contribution of the TE mode of the nth order, the functions $X_n^{(a)}$ and $Y_n^{(a)}$ have the form

$$X_n^{(a)} = \begin{vmatrix} j_n(k_1 r_1) & j_n(k_2 r_1) & y_n(k_2 r_1) & 0 \\ u_n'(k_1 r_1) & u_n'(k_2 r_1) & v_n'(k_2 r_1) & 0 \\ 0 & j_n(k_2 r_2) & y_n(k_2 r_2) & j_n(k_h r_2) \\ 0 & u_n'(k_2 r_2) & v_n'(k_2 r_2) & u_n'(k_h r_2) \end{vmatrix}, \quad (28)$$

$$Y_n^{(a)} = \begin{vmatrix} j_n(k_1 r_1) & j_n(k_2 r_1) & y_n(k_2 r_1) & 0 \\ u_n'(k_1 r_1) & u_n'(k_2 r_1) & v_n'(k_2 r_1) & 0 \\ 0 & j_n(k_2 r_2) & y_n(k_2 r_2) & h_n^{(1)}(k_h r_2) \\ 0 & u_n'(k_2 r_2) & v_n'(k_2 r_2) & w_n'(k_h r_2) \end{vmatrix}. \quad (29)$$

Here, $k_1 = \omega\sqrt{\varepsilon_1}/c$ and $k_2 = \omega\sqrt{\varepsilon_2}/c$ are the magnitudes of the wave vectors of light in the core and shell; $\varepsilon_1 \equiv \varepsilon_m(\omega)$ and $\varepsilon_2 \equiv \varepsilon_J(\omega)$ are the complex permittivities of the metal core and the organic shell at the frequency of the incident light; r_1 and r_2 are the core radius and the outer radius of the particle, respectively; $j_n(z)$, $y_n(z)$, and $h_n^{(1)}(z)$ are the Bessel, Neumann, and Hankel spherical functions; and $u_n(z) = z j_n(z)$,

$v_n(z) = zy_n(z)$, and $w_n(z) = zh_n^{(1)}(z)$ are the Riccati–Bessel, Riccati–Neumann, and Riccati–Hankel spherical functions, respectively. The prime denotes differentiation of the function with respect to its argument.

Similarly, the final expressions for the functions $X_n^{(b)}$ and $Y_n^{(b)}$, which determine the contributions of the TM modes, can be represented as in [89]

$$X_n^{(b)} = \begin{vmatrix} j_n(k_1r_1) & \sqrt{\frac{\varepsilon_2}{\varepsilon_1}}\,j_n(k_2r_1) & \sqrt{\frac{\varepsilon_2}{\varepsilon_1}}\,y_n(k_2r_1) & 0 \\ u_n'(k_1r_1) & \sqrt{\frac{\varepsilon_1}{\varepsilon_2}}\,u_n'(k_2r_1) & \sqrt{\frac{\varepsilon_1}{\varepsilon_2}}\,v_n'(k_2r_1) & 0 \\ 0 & \sqrt{\frac{\varepsilon_2}{\varepsilon_h}}\,j_n(k_2r_2) & \sqrt{\frac{\varepsilon_2}{\varepsilon_h}}\,y_n(k_2r_2) & j_n(k_hr_2) \\ 0 & \sqrt{\frac{\varepsilon_h}{\varepsilon_2}}\,u_n'(k_2r_2) & \sqrt{\frac{\varepsilon_h}{\varepsilon_2}}\,v_n'(k_2r_2) & u_n'(k_hr_2) \end{vmatrix}, \tag{30}$$

$$Y_n^{(b)} = \begin{vmatrix} j_n(k_1r_1) & \sqrt{\frac{\varepsilon_2}{\varepsilon_1}}\,j_n(k_2r_1) & \sqrt{\frac{\varepsilon_2}{\varepsilon_1}}\,y_n(k_2r_1) & 0 \\ u_n'(k_1r_1) & \sqrt{\frac{\varepsilon_1}{\varepsilon_2}}\,u_n'(k_2r_1) & \sqrt{\frac{\varepsilon_1}{\varepsilon_2}}\,v_n'(k_2r_1) & 0 \\ 0 & \sqrt{\frac{\varepsilon_2}{\varepsilon_h}}\,j_n(k_2r_2) & \sqrt{\frac{\varepsilon_2}{\varepsilon_h}}\,y_n(k_2r_2) & h_n^{(1)}(k_hr_2) \\ 0 & \sqrt{\frac{\varepsilon_h}{\varepsilon_2}}\,u_n'(k_2r_2) & \sqrt{\frac{\varepsilon_h}{\varepsilon_2}}\,v_n'(k_2r_2) & w_n'(k_hr_2) \end{vmatrix}. \tag{31}$$

Combined with formulas (24)–(26), expressions (27)–(31) allow one to calculate the total absorption, scattering, and extinction cross sections, as well as the contributions of individual terms of the multipole series corresponding to TM and TE modes of different orders. In practical calculations, the maximum number of series members that must be taken into account in formulas (24)–(26) can be estimated using the expression [268]

$$n_{\max} = (kr) + 4.05(kr)^{1/3} + 2\,, \tag{32}$$

where $r = r_2$ is the outer radius of the concentric spheres.

For three-layer particles (see Fig. 9) and, especially, multilayer particles, the expressions for the expansion coefficients a_n and b_n turn out to be quite cumbersome. Therefore, it is convenient to use recurrence relations for their calculation rather than represent them in the form of determinants. This approach was used in papers [116, 265, 266].

4.3 Formulas of quasistatic approximation

For a particle with a radius much smaller than the wavelength of light, we can use the quasistatic approximation and limit ourselves to the contribution of the electric dipole term ($n = 1$). Then, the extinction and scattering cross sections have the form [148]

$$\sigma_{\text{ext}}(\omega) = 4\pi k_h \operatorname{Im}\{\alpha(\omega)\}, \quad \sigma_{\text{scat}}(\omega) = \frac{8\pi}{3}\,k_h^4\left|\alpha(\omega)\right|^2. \tag{33}$$

Here, k_h is the modulus of the wave vector of incident radiation in a passive environment with permittivity ε_h, and α is the polarizability of the particle. The simplest form is that of the dipole polarizability of a bare metal particle with radius r and permittivity $\varepsilon = \varepsilon_m$ [148]:

$$\alpha = r^3\,\frac{\varepsilon_m - \varepsilon_h}{\varepsilon_m + 2\varepsilon_h}\,. \tag{34}$$

Thus, according to (34), the polarizability of a sphere is proportional to its volume ($\alpha \propto r^3$), and so the scattering cross section for small-radius spheres in the quasistatic approximation ($kr \ll 1$) turns out to be much smaller than the absorption cross section $\sigma_{\text{scat}} \ll \sigma_{\text{abs}}$. In this situation, the extinction cross section ($\sigma_{\text{ext}} = \sigma_{\text{abs}} + \sigma_{\text{scat}}$) in formula (33) and the absorption cross section are practically equal to each other, $\sigma_{\text{ext}} \approx \sigma_{\text{abs}}$ (see [148], p. 176). For a two-layer particle, instead of ε_m in (34), one should use the effective permittivity of the 'core–shell' system, $\varepsilon_2^{\text{eff}}$, which is equivalent to the permittivity of a homogeneous sphere and is calculated by the formula [263]

$$\varepsilon_2^{\text{eff}} = \varepsilon_2\,\frac{2\bigl(1 - (r_1/r_2)^3\bigr) + \bigl(1 + 2(r_1/r_2)^3\bigr)(\varepsilon_1/\varepsilon_2)}{\bigl(2 + (r_1/r_2)^3\bigr) + \bigl(1 - (r_1/r_2)^3\bigr)(\varepsilon_1/\varepsilon_2)}\,. \tag{35}$$

Here, r_1 and r_2 are the inner and outer radii of the concentric spheres, and $\varepsilon_1 = \varepsilon_m$ and $\varepsilon_2 = \varepsilon_J$ are the permittivities of the metal core and the J-aggregate shell, respectively. Thus, the dipole polarizability α of a two-layer particle of volume $\mathcal{V} = 4\pi r_2^3/3$ is represented as [261]

$$\alpha = \frac{(\varepsilon_1 - \varepsilon_2)(2\varepsilon_2 + \varepsilon_h)r_1^3 + (\varepsilon_2 - \varepsilon_h)(2\varepsilon_2 + \varepsilon_1)r_2^3}{2(\varepsilon_1 - \varepsilon_2)(\varepsilon_2 - \varepsilon_h)(r_1/r_2)^3 + (\varepsilon_2 + 2\varepsilon_h)(2\varepsilon_2 + \varepsilon_1)}\,. \tag{36}$$

Together with (33), this expression makes it possible to estimate the electric dipole contribution to cross sections of light extinction and scattering by a hybrid two-layer particle.

Whenever the radius of a three-layer particle is much smaller than the wavelength of light, the extinction (σ_{ext}) and scattering (σ_{scat}) cross sections can be written as (33) and expressed through its dipole polarizability α and the modulus k_h of the wave vector of incident radiation in a medium with permittivity ε_h. According to [269], the effective dipole polarizability of a three-layer particle, $\alpha(\omega)$, has the form

$$\alpha = r_3^3\,\frac{A(\varepsilon_3 - \varepsilon_h) - B(2\varepsilon_3 + \varepsilon_h)(r_2/r_3)^3}{A(2\varepsilon_3 + \varepsilon_h) - B(\varepsilon_3 - \varepsilon_h)(r_2/r_3)^3}\,. \tag{37}$$

The coefficients A and B in (37) are calculated using the formulas

$$A = (2\varepsilon_3 + \varepsilon_2)(2\varepsilon_2 + \varepsilon_1) + 2(\varepsilon_3 - \varepsilon_2)(\varepsilon_2 - \varepsilon_1)\left(\frac{r_1}{r_2}\right)^3, \tag{38}$$

$$B = (\varepsilon_3 - \varepsilon_2)(2\varepsilon_2 + \varepsilon_1) + (\varepsilon_3 + 2\varepsilon_2)(\varepsilon_2 - \varepsilon_1)\left(\frac{r_1}{r_2}\right)^3, \tag{39}$$

and $\mathcal{V} = 4\pi r_3^3/3$ is the total volume of a three-layer particle.

4.4 Simulation of optical properties of nonspherical hybrid nanoparticles

As already noted in Section 2.5, in contrast to spherical particles, spheroidal particles have a preferred direction along their symmetry axis. Therefore, contrary to a metal sphere, the light absorption and scattering spectra in the case of a homogeneous metal spheroid are split into two peaks of plasmon resonances: longitudinal and transverse. The problem of scattering and absorption of electromagnetic waves by

spheroidal particles is divided into two cases: (i) a prolate spheroid $a > b$ (formed by rotating an ellipse around its long axis a), and (ii) an oblate spheroid $a < b$ (formed by rotating an ellipse around its minor axis b). For a spheroid consisting of a metal core and a J-aggregate shell, the general formulas for the light scattering and absorption cross sections turn out to be very cumbersome for both prolate and oblate spheroids [270]. However, when the size of the composite particle is sufficiently small compared to the radiation wavelength ($a, b \ll \lambda$), the extinction cross sections can be calculated using simple analytical formulas of the quasistatic approximation for a two-layer spheroid [271] and ellipsoid [272].

For hybrid nanostructures of a more complex shape than spherical, spheroidal, cubic, or cylindrical, there are no solutions in the form of analytical or special functions. Light absorption and scattering spectra for both single-layer and multilayer metalorganic nanostructures can be calculated using a variety of numerical methods for solving Maxwell's equations for electromagnetic fields inside and outside nanostructures. The most widely used methods are as follows: (i) Finite-Difference Time-Domain (FDTD) method [273], (ii) T-matrix method [274, 275], (iii) Multiple Multipole (MMP) method [276, 277], (iv) Discrete Dipole Approximation (DDA) [278], and (v) Volume Integral Equations Method (VIEM) [279]. Depending on the type of problem being solved, one method or another has an advantage. Unlike the quasistatic approximation, approaches based on the use of these numerical methods make it possible to determine the cross sections of absorption and scattering of light for an arbitrary relationship between the nanoparticle size and the wavelength of light, taking into account the contribution of all electric and magnetic multipoles.

5. Analytical models of plasmon-exciton coupling

5.1 Simple formulas for frequencies of hybrid plexcitonic modes

Coupling between surface plasmons in the metal core and a Frenkel exciton in the shell leads to the formation of plexcitonic hybrid modes of a composite particle. The eigenfrequencies of hybrid modes of a two-layer metal/J-aggregate nanosphere, i.e., the positions of the maxima in its absorption cross section can be determined approximately using an analytical approach [89]. It is a generalization of a simple means for finding the spectral position of the dipole plasmon resonance peak of a homogeneous metal sphere. According to this approach, the eigenfrequencies of hybrid modes can be calculated within the framework of the applicability of the quasistatic approximation using the relation $\mathrm{Re}\,\{\varepsilon_2^{\mathrm{eff}}(\omega)\} = -2\varepsilon_{\mathrm{h}}$ containing the effective permittivity $\varepsilon_2^{\mathrm{eff}}$ of the two-layer sphere (35). The conventional isotropic model (20) is employed here for the permittivity of the excitonic J-aggregate shell. The consideration [89] is valid in the frequency range where the dominant contribution to the total permittivity of the metal core is determined by free electrons, i.e., $\varepsilon_{\mathrm{m}} = \varepsilon_{\mathrm{intra}}$ (see formula (6)). Then, neglecting the imaginary parts of dielectric functions (6) and (20), i.e. putting $\gamma_{\mathrm{intra}} = 0$ and $\gamma_{\mathrm{ex}} = 0$, we can obtain the cubic equation

$$C_3 x^3 + C_2 x^2 + C_1 x + C_0 = 0\,, \quad x = \omega^2 \tag{40}$$

for the square of the eigenfrequencies of the hybrid modes of a metal/J-aggregate particle. The values of the coefficients C_j ($j = 0, 1, 2, 3$) are determined by the parameters of the dielectric functions of the plasmonic and excitonic subsystems of the hybrid particle and the ratio $\zeta = (r_1/r_2)^3$ of the volumes of concentric spheres with radii r_1 and r_2. Their specific form is given in paper [89].

Using the substitution $y = x + C_2/3C_3$, equation (40) is rewritten in the canonical form

$$y^3 + py + q = 0\,, \quad p = -\frac{a^2}{3} + b, \quad q = 2\left(\frac{a}{3}\right)^3 - \frac{ab}{3} + c\,, \tag{41}$$

where $a = C_2/C_3$, $b = C_1/C_3$, and $c = C_0/C_3$. Since all the coefficients C_i and p, q are real, the number of real roots of equation (40) depends on the sign of $Q = (p/3)^3 + (q/2)^2$. It follows from the above analysis that Q turns out to be negative in the cases under consideration and, consequently, $p < 0$. Therefore, within the framework of the isotropic model (20), equations (40) and (41) have three different real positive roots, with the exception of the limiting cases $r_1 = 0$ and $r_1 = r_2$. It is convenient to represent these roots ($x_i \equiv \omega_i^2$) in the trigonometric form:

$$\omega_1^2 = -\frac{a}{3} + 2\sqrt{-\frac{p}{3}}\,\cos\left(\frac{\beta}{3}\right),$$

$$\omega_{2,3}^2 = -\frac{a}{3} - 2\sqrt{-\frac{p}{3}}\,\cos\left(\frac{\beta}{3} \pm \frac{\pi}{3}\right), \tag{42}$$

$$\cos\beta = -\frac{q}{2\sqrt{-(p/3)^3}}\,. \tag{43}$$

The eigenfrequencies of the hybrid modes depend on the plasma frequency $\omega_{\mathrm{p}} = (4\pi n_{\mathrm{e}} e^2/m_{\mathrm{e}})^{1/2}$ included in the modified Drude formula (6), the frequency ω_{ex}, the effective oscillator strength f of the exciton transition (20), and the ratio $\zeta = (r_1/r_2)^3$. We recall that the eigenfrequency of the electric dipole surface plasmon-polariton, $\omega_{\mathrm{pl}}^{(\mathrm{dip})}$, is expressed through the plasma frequency ω_{p} using the Fröhlich formula (13). Formulas (42) and (43) determine the positions of three maxima in the absorption spectrum of a metal/J-aggregate particle. They are valid in the quasistatic approximation for the case of an outer shell being isotropic, and can be used when interband transitions in the core (e.g., Ag) do not make a noticeable contribution to the dielectric function $\varepsilon_{\mathrm{m}}(\omega, r)$.

Below are given explicit expressions for the coefficients a, b, and c in formulas (41)–(43), depending on the frequencies ω_{p}, and ω_{ex}, the ζ ratio, and the effective oscillator strength f of the transition for the special case when $\varepsilon_{\mathrm{h}} = \varepsilon_{\mathrm{J}}^{\infty} = \varepsilon_{\mathrm{m}}^{\infty} = 1$:

$$a = -\frac{1}{3}\left[3(f+2)\omega_{\mathrm{ex}}^2 + \omega_{\mathrm{p}}^2\right], \quad c = -\frac{\omega_{\mathrm{ex}}^4 \omega_{\mathrm{p}}^2}{9}\left[3 + f(1+2\zeta)\right], \tag{44}$$

$$b = \frac{\omega_{\mathrm{ex}}^2}{9}\left\{\omega_{\mathrm{ex}}^2\left[2f^2(1-\zeta) + 9(f+1)\right] + \omega_{\mathrm{p}}^2\left[f(1+2\zeta) + 6\right]\right\}. \tag{45}$$

In general, the coefficients a, b, and c and the frequencies of the hybrid modes depend, among other factors, on the permittivity ε_{h} of the host medium and the constants $\varepsilon_{\mathrm{m}}^{\infty}$ and $\varepsilon_{\mathrm{J}}^{\infty}$.

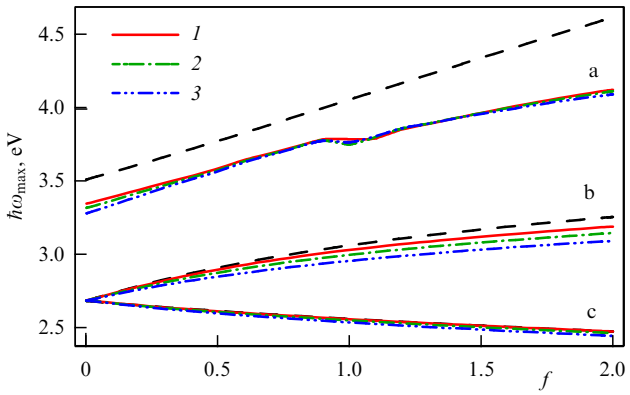

Figure 10. Positions of maxima ($\hbar\omega_{max}$) of (a) 'high-energy,' (b) 'medium-energy,' and (c) 'low-energy' absorption peaks of Ag/J-aggregate particles as functions of effective oscillator strength, f, of an excitonic transition [89]. Solid and dashed-dotted curves correspond to different geometric parameters of system: *1* — $r_1 = 10$ nm, $r_2 = 12$ nm; *2* — $r_1 = 15$ nm, $r_2 = 18$ nm; *3* — $r_1 = 20$ nm, $r_2 = 24$ nm with fixed ratio $r_1/r_2 = 5/6$. Dashed curves are corresponding analytical results (43) obtained for same value of r_1/r_2.

A comparison of the results [89] of the above model with exact calculations within the framework of the extended Mie theory showed their good agreement in the region of applicability of the quasistatic approximation and justified the use of the isotropic model for the permittivity of the J-aggregate shell of a plexcitonic particle. This is demonstrated by Fig. 10, which shows the results [89] for the spectral positions of the maxima of (1) 'high-energy,' (2) 'medium-energy,' and (3) 'low-energy' peaks of light absorption by spherical Ag/J-aggregate particles as functions of the effective oscillator strength f of the transition in the J-band of the dye. The corresponding numerical calculations were performed for various values of the internal, r_1, and external, r_2, radii of the particle: $r_1 = 10$ nm, $r_2 = 12$ nm (curves *1*); $r_1 = 15$ nm, $r_2 = 18$ nm (curves *2*); and $r_1 = 20$ nm, $r_2 = 24$ nm (curves *3*). The values of r_1 and r_2 are chosen so that their ratio remains the same, $r_1/r_2 = 5/6$. The dashed curves in Fig. 10 show the results of calculations of the frequencies of the particle's hybrid modes, carried out within the framework of the analytical model [89]. All optical constants related to the J-aggregate shell (except for the effective oscillator strength f) are taken to be equal to the corresponding values for the TC dye (see Table 2).

Some quantitative discrepancies between the results of the analytical model and the exact calculation are present only for the 'high-energy' peak appearing near the energies of electron transitions between the d-valence band and the sp-conduction band of silver ($\hbar\omega_g = 3.7$ eV). In this spectral range, the dielectric function of silver cannot be reliably described by the Drude formula alone. Therefore, to correctly describe the behavior of this hybrid mode for photon energies that are close to the interband transitions, the analytical approach [89] should be supplemented with a correct evaluation of the contribution to the dielectric function of interband transitions of electrons in the silver core. Moreover, it is necessary to correctly account for the spectral width γ_{ex} of the J-band of the dye shell and the damping coefficients of free, γ_{intra}, and bound, γ_{inter}, electrons. Note that, since the radius of the core in the calculations shown in Fig. 10 does not exceed 20 nm, no high-order multipole resonances ($n > 1$) make a noticeable contribution to the absorption cross section. Therefore, the hybrid modes of the composite system arise here only as a result of the interaction of the Frenkel exciton of the J-aggregate shell and the dipole plasmon in the core.

Figure 10 clearly demonstrates that the positions of the maxima in the light absorption spectra strongly depend on the value of the effective oscillator strength in the J-band of the dye aggregate [89]. The analysis of the dependences of the frequencies of hybrid modes of metalorganic nanoparticles on the values of f and ε_J^∞ was also performed in [67, 121] and recently in [252] for the cases of isotropic and anisotropic excitonic shells.

5.2 Classical model of coupled oscillators

5.2.1 General formulas. The effects of plexcitonic coupling are often described using the model of coupled damped oscillators. It describes a system of dipoles in an external monochromatic field, coupled via local electromagnetic fields. Such models have been extensively used in various applications of vibration theory. Starting from papers [280–282], they have been applied to analyze the effects of plasmonic interactions in metal nanostructures with various organic and inorganic systems, including excitons in quantum dots and in molecular J-aggregates of dyes. According to [121, 141, 283], the system of differential equations for two coupled dipoles can be written as

$$\ddot{p}_{pl} + \gamma_{pl}\dot{p}_{pl} + \omega_{pl}^2 p_{pl} = A_{pl}\left[E_0\cos(\omega t) + M p_{ex}\right], \qquad (46)$$

$$\ddot{p}_{ex} + \gamma_{ex}\dot{p}_{ex} + \omega_{ex}^2 p_{ex} = A_{ex}\left[E_0\cos(\omega t) + M p_{pl}\right]. \qquad (47)$$

Here, p_{pl} and p_{ex} are the dipole moments of the plasmonic and excitonic subsystems, E_0 is the amplitude of the external electric field, and ω is its frequency. The parameters A_{pl} and A_{ex} are related to the classical oscillator strengths f_{pl} and f_{ex}, and M is the dipole coupling constant [283]. The system of equations (46) and (47) allows an exact solution (see, for example, [121]):

$$p_{pl}(t) = \mathrm{Re}\left\{p_{pl}^{(0)}\exp(-i\omega t)\right\}, \quad p_{ex}(t) = \mathrm{Re}\left\{p_{ex}^{(0)}\exp(-i\omega t)\right\}, \qquad (48)$$

$$p_{pl}^{(0)} = \frac{E_0 A_{pl}\left[1 + (A_{ex}M)/B_{ex}(\omega)\right]}{B_{pl}(\omega)\left[1 - (A_{pl}A_{ex}M^2)/\left(B_{pl}(\omega)B_{ex}(\omega)\right)\right]},$$
$$p_{ex}^{(0)} = \frac{E_0 A_{ex}\left[1 + (A_{pl}M)/B_{pl}(\omega)\right]}{B_{ex}(\omega)\left[1 - (A_{pl}A_{ex}M^2)/\left(B_{pl}(\omega)B_{ex}(\omega)\right)\right]}, \qquad (49)$$

where $B_j(\omega) = \omega_j^2 - \omega^2 - i\gamma_j\omega$, $j = \mathrm{pl}, \mathrm{ex}$. The cross sections of extinction and scattering of light by the plexcitonic system have the form [283]

$$\sigma_{ext} = \frac{4\pi n_h \omega}{c}\,\mathrm{Im}\left\{\frac{p_{pl}^{(0)} + p_{ex}^{(0)}}{E_0}\right\},$$
$$\sigma_{scat} = \frac{8\pi}{3}\left(\frac{n_h\omega}{c}\right)^4\left|\frac{p_{pl}^{(0)} + p_{ex}^{(0)}}{E_0}\right|^2, \qquad (50)$$

where n_h is the refractive index of the host medium.

The coupled dipole model has seven parameters: ω_j, γ_j, A_j ($j = \mathrm{pl}, \mathrm{ex}$), and M, which are included in system of equations (46), (47) and in expressions (50) for the cross sections of extinction and scattering of light. The classical expression for the coupling energy V of oscillators, similar to the expression for the coupling energy $V = \hbar g$ of two states in the quantum model, can be easily obtained in the resonant case:

$\omega_{pl} = \omega_{ex} \equiv \omega_0$. In this case, the classical and quantum considerations equally reproduce optical spectra with two symmetrical resonant peaks, and their energy splitting corresponds to the double coupling energy of the oscillators. Within the framework of the classical model, these resonant frequencies are associated with the zeros of the real parts of the denominators in formulas (49). Assuming that the damping constants γ_i are small compared to ω and ω_0, we can find two zeros separated in energy by the value

$$V = \frac{\hbar M}{2\omega_0}\sqrt{A_{pl}A_{ex}}\,. \tag{51}$$

Formula (51) relates the effective plexcitonic coupling energy V with the coupling constant M appearing in the system of equations (46), (47) for coupled dipoles.

For a single excitonic oscillator (a single monomer molecule, molecular aggregate, or quantum dot) interacting with a plasmonic oscillator, the coefficients A_{pl} and A_{ex} can be represented in a standard form [121] through the classical oscillator strengths $f_{pl}^{(cl)}$ and $f_{ex}^{(cl)}$, which determine their polarizabilities:

$$A_{pl} = \frac{e^2}{m_e} f_{pl}^{(cl)}\,,$$

$$A_{ex} = \frac{e^2}{m_e} f_{ex}^{(cl)}\,.$$

Thus, formula (51) is given by

$$V = \frac{\hbar M}{2\omega_0}\frac{e^2}{m_e}\sqrt{f_{pl}^{(cl)} f_{ex}^{(cl)}}\,.$$

When considering N_{ex} excitonic oscillators interacting with a plasmon, the coefficient A_{ex} can be written as [121]

$$A_{ex} = N_{ex}\frac{e^2}{m_e} f_{ex}^{(cl)}\,,$$

so that the expression for the energy of plexcitonic coupling of dipoles takes the form

$$V = \frac{\hbar M}{2\omega_0}\frac{e^2}{m_e}\sqrt{N_{ex}}\sqrt{f_{pl}^{(cl)} f_{ex}^{(cl)}}\,. \tag{52}$$

This expression (52) demonstrates a general important feature, consisting in the proportionality of the plexcitonic coupling energy to the square root of a number of excitonic oscillators, $V \propto \sqrt{N_{ex}}$, which can be monomer molecules, molecular aggregates, or quantum dots. In review [141] on the electromagnetic coupling of surface plasmons with quantum emitters, this feature was demonstrated in several other ways. Note that, under usual experimental conditions, the density of excitons in ordered molecular organic materials is very low [141, 181]. For the plexcitonic systems consisting of a metal core with an outer J-aggregate shell of a dye, this means that the average number of aggregates in the excited state, N_{ex}^*, is significantly less than their total number, N_{ex}, which is included in formula (52), $N_{ex}^* \ll N_{ex}$. The average number of excitons depends on a number of factors, including the type of plexcitonic system under consideration and the power density of the radiation incident on this system. A detailed discussion of this topic is beyond the scope of this review.

5.2.2 Resonance and antiresonance. The phenomenon of resonance, well-known in various areas of physics, consists of an enhanced response of a system to an external excitation at a frequency close to the eigenfrequency of the system. In some cases, the opposite phenomenon, antiresonance, may occur when the system's response is suppressed under certain conditions. The resonance and antiresonance phenomena can be illustrated using the model of coupled oscillators with eigenfrequencies ω_1 and ω_2. In many situations, it can be assumed that only one of them is driven by a periodic force (Fig. 11a). This situation is realized, for example, in the widely studied metalorganic 'core–shell' nanoparticles (see Section 6). For such particles, the interaction of light with their plasmonic subsystem turns out to be dominant, since the volume $\mathcal{V}_{pl}$ of the plasmonic core substantially exceeds the volume $\mathcal{V}_{ex}$ of the outer excitonic shell. Therefore, the polarizability of the metal core, α_{pl}, significantly exceeds the polarizability of the excitonic shell, $\alpha_{pl} \gg \alpha_{ex}$. Below, for the sake of generality, we will use the subscript 1 for an oscillator excited by an external periodic force $F \equiv F_1$ with a frequency ω, without specifying whether this oscillator is plasmonic or excitonic. The system is described by coupled differential equations

$$\ddot{x}_1 + \gamma_1\dot{x}_1 + \omega_1^2 x_1 - \Omega^2 x_2 = \frac{F}{m}\exp(i\omega t)\,, \tag{53}$$

$$\ddot{x}_2 + \gamma_2\dot{x}_2 + \omega_2^2 x_2 - \Omega^2 x_1 = 0\,, \tag{54}$$

where γ_1 and γ_2 are the damping constants of the first and second oscillators, Ω is their coupling constant, and $m \equiv m_1$ is the mass of the driven oscillator.

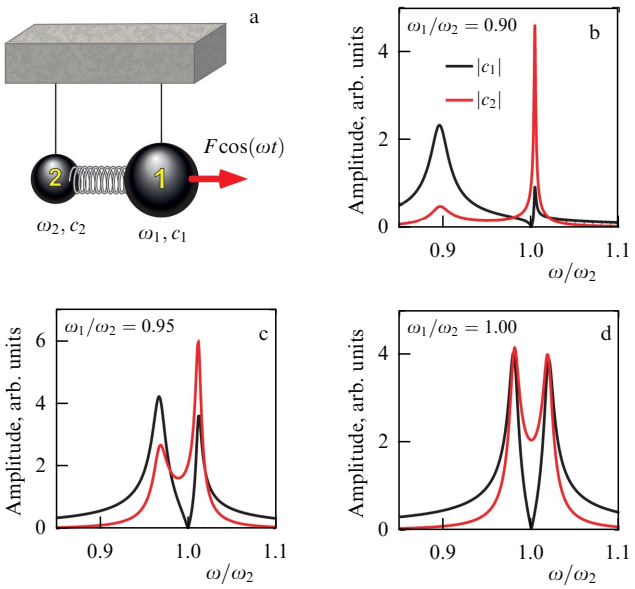

Figure 11. (a) Schematic view of coupled damped oscillators with periodic force $F\cos(\omega t)$ applied to one of them. (b)–(d) Dependences of amplitude $|c_1|$ of oscillations of driven oscillator '1' with eigenfrequency ω_1 and amplitude $|c_2|$ of coupled oscillator '2' with frequency ω_2 on dimensionless frequency ω/ω_2 (see formulas (55), (56)). Calculations are performed for three values of the ratio of eigenfrequencies $\omega_1/\omega_2 = 0.90$ (b), 0.95 (c), and 1.00 (d); factor determining the amplitude of oscillations $|F|/(m\omega_2)$ was chosen equal to 0.1 cm s^{-1}. Other parameters are fixed: $\gamma_1/\omega_2 = 2\times10^{-2}$, $\gamma_2/\omega_2 = 1\times10^{-3}$, $\Omega/\omega_2 = 0.2$.

The free motion of oscillators ($F = 0$) in the absence of coupling ($\Omega = 0$) represents their independent oscillations with given eigenfrequencies ω_1 and ω_2. Solving equation (54) for two coupled oscillators in the form of forced oscillations, $x_1 = c_1 \exp(i\omega t)$ and $x_2 = c_2 \exp(i\omega t)$, leads to the following expressions for the oscillation amplitudes [284]:

$$c_1(\omega) = \frac{(\omega_2^2 - \omega^2 + i\gamma_2\omega)(F/m)}{(\omega_1^2 - \omega^2 + i\gamma_1\omega)(\omega_2^2 - \omega^2 + i\gamma_2\omega) - \Omega^4}, \qquad (55)$$

$$c_2(\omega) = -\frac{\Omega^2(F/m)}{(\omega_1^2 - \omega^2 + i\gamma_1\omega)(\omega_2^2 - \omega^2 + i\gamma_2\omega) - \Omega^4}. \qquad (56)$$

The phase difference between two coupled oscillators is given by the expression

$$\varphi_2 - \varphi_1 = \pi - \arctan\left(\frac{\gamma_2\omega}{\omega_2^2 - \omega^2}\right). \qquad (57)$$

Figure 11 shows the results of our calculations of the oscillation amplitudes $|c_1|$ and $|c_2|$ of two oscillators, performed using formulas (55) and (56) at different ratios between their eigenfrequencies, ω_1/ω_2. The cases of large, intermediate, and zero frequency detunings are illustrated in Figs 11b–d. One can see that in such a system there are two resonances at frequencies ω_- and ω_+, which, neglecting damping ($\gamma_1 = 0$, $\gamma_2 = 0$), are expressed through the eigenfrequencies ω_1 and ω_2 of the oscillators and have the form (see, for example, [121])

$$\omega_\pm^2 = \frac{\omega_1^2 + \omega_2^2}{2} \pm \sqrt{\left(\frac{\omega_1^2 - \omega_2^2}{2}\right)^2 + \Omega^4}. \qquad (58)$$

The behavior of the spectral profile of the first oscillator depends significantly on the detuning of its eigenfrequency ω_1 from the eigenfrequency ω_2 of the second oscillator. In the case of large detuning (Fig. 11b), the first oscillator exhibits resonances with symmetrical and asymmetrical profiles near frequencies ω_1 and ω_2, respectively. The first resonance in the spectrum of oscillator '1' excited by an external force is described by a symmetrical Lorentz-type contour and exhibits a standard increase in the oscillation amplitude near the eigenfrequency ω_1. The second resonance is characterized by an asymmetrical profile. At the eigenfrequency ω_2 of the second coupled oscillator, the amplitude of the first oscillator vanishes. This means complete suppression of the amplitude of the driven oscillator '1' at the eigenfrequency of the coupled oscillator '2.' This is an antiresonance phenomenon caused by destructive interference of oscillations as a result of the action of a periodic external force and interaction with the second oscillator. Antiresonance can be observed in coupled mechanical, acoustic, electromagnetic, and quantum systems [284, 285].

As the detuning of frequencies ω_1 and ω_2 decreases, the difference in the amplitudes $|c_1|$ and $|c_2|$ at the peak maxima becomes less pronounced (Fig. 11c). The shape of the curve describing the two resonant peaks and the dip between them, corresponding to antiresonance, also becomes somewhat more symmetrical. If the eigenfrequencies of the oscillators coincide, $\omega_1 = \omega_2$, the shape of the dip becomes almost symmetrical (Fig. 11d), and the antiresonance phenomenon manifests itself as a splitting of the spectral peak of oscillator '1.' Note that in all three cases both resonance peaks of oscillator '2' are symmetrical (red curves in Figs 11b–d), i.e., there is no antiresonance in the spectrum of the unperturbed oscillator, although its amplitude has a minimum between the peaks.

Using the model of coupled oscillators, a reasonable theoretical interpretation can be given to a number of experimentally observed phenomena in the optics of plexcitonic nanosystems. Moreover, it is possible to provide a simple explanation for some limiting cases of the model, which differ from each other in the qualitatively different behaviors of the light absorption and scattering spectra.

5.2.3 Effect of induced transparency. One of the most discussed phenomena in the optics of plexcitonic nanosystems is a pronounced dip in the light absorption, scattering, and extinction spectra, observed in many experimental studies [67, 92, 318]. This phenomenon arises when plasmon and exciton frequencies coincide exactly (or are quite close), $\omega_0 \equiv \omega_{pl} = \omega_{ex}$, and leads to a sharp increase in the transmission of light at the resonance frequency ω_0. In the transmission spectra, this effect manifests itself as an intense peak. Correspondingly, a number of authors often call it the induced transparency (IT) effect [67, 92, 286, 318].

This phenomenon can be explained theoretically within the framework of the classical coupled oscillators model outlined above. To this end, we need to derive a general expression for the averaged power, $\overline{P}(\omega)$, absorbed by the plexcitonic system over the period of the incident light wave. Using expressions (55), (56) for the amplitudes c_1 and c_2 of the oscillations, we arrive at the following result [295]

$$\overline{P}(\omega) = \frac{\omega}{2}\,\mathrm{Im}\{c_1(\omega)F^*\} = \frac{\omega^2|F|^2}{2m} \times \frac{\gamma_2(\Omega^4 + \gamma_1\gamma_2\omega^2) + \gamma_1(\omega^2 - \omega_2^2)^2}{\left[(\omega^2 - \omega_1^2)(\omega^2 - \omega_2^2) - \Omega^4\right]^2 + \omega^2\left[\gamma_1^2(\omega^2 - \omega_2^2)^2 + \gamma_2^2(\omega^2 - \omega_1^2)^2 + 2\gamma_1\gamma_2\Omega^4\right] + \gamma_1^2\gamma_2^2\omega^4}. \qquad (59)$$

This expression is applicable to an arbitrary detuning of the oscillator frequencies ω_1 and ω_2. It takes into account the fact that, in the simplified model of coupled oscillators, the force F acts only on one of them (Fig. 11a). In order for the induced transparency effect to be most clearly manifested, the decay rate of one of the oscillators must be much smaller than that of the other, $\gamma_2 \ll \gamma_1$, since energy dissipation should not substantially increase as a result of adding a second oscillator. This means that the energy dissipation occurs predominantly in the plasmonic subsystem '1' rather than in the excitonic subsystem '2'. Correspondingly, the width of the plasmon resonance, $\gamma_{pl} \equiv \gamma_1$, is significantly larger than the width of the excitonic band, $\gamma_{ex} \equiv \gamma_2$. This situation is realized in a 'core–shell' plexcitonic system, containing a metal nanoparticle as a core and a dye J-aggregate as a shell. It is such hybrid metalorganic nanoparticles that have been most intensively studied experimentally and theoretically. In particular, a series of detailed numerical calculations were performed using the FDTD method in order to give a self-consistent explanation of this effect.

Here, we offer a simple explanation to the induced transparency effect using analytical formula (59) obtained within the framework of the coupled oscillator model. It takes a particularly simple form when the resonant frequencies of

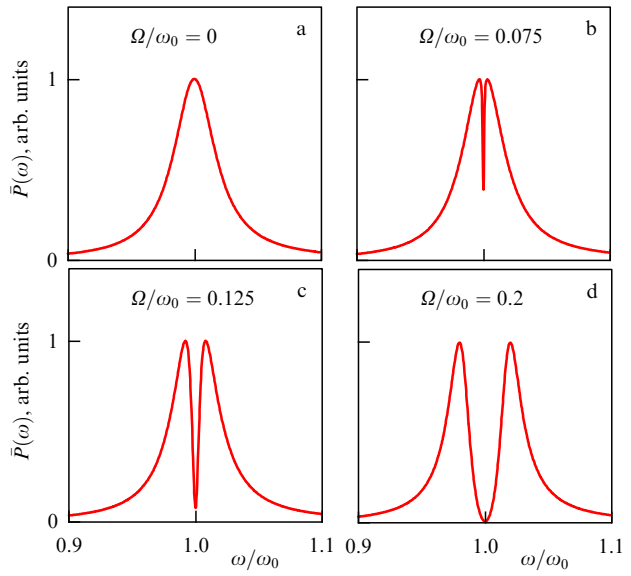

Figure 12. Power, averaged over oscillation period $\overline{P}(\omega)$, absorbed by a system of two coupled oscillators (Fig. 11a) as a function of normalized frequency (ω/ω_0) of incident light at four values of the dimensionless coupling parameter: (a) $\Omega/\omega_0 = 0$, (b) 0.075, (c) 0.125, and (d) 0.2. Eigenfrequencies of oscillators '1' and '2' coincide, $\hbar\omega_1 = \hbar\omega_2 = \hbar\omega_0 = 2.0$ eV; oscillator damping constants are $\hbar\gamma_1 = 8 \times 10^{-2}$ eV and $\hbar\gamma_2 = 1 \times 10^{-3}$ eV; efficiency of driving force is $|F|^2/(m\omega_0^2) = 0.5$ eV.

the coupled plasmonic and excitonic subsystems coincide, $\omega_0 \equiv \omega_1 = \omega_2$:

$$\overline{P}(\omega) = \frac{\omega^2|F|^2}{2m} \times \frac{\gamma_2(\Omega^4 + \gamma_1\gamma_2\omega^2) + \gamma_1(\omega^2 - \omega_0^2)^2}{\left[(\omega^2-\omega_0^2)^2-\Omega^4\right]^2 + \omega^2\left[(\gamma_1^2+\gamma_2^2)(\omega^2-\omega_0^2)^2+2\gamma_1\gamma_2\Omega^4\right]+\gamma_1^2\gamma_2^2\omega^4}. \quad (60)$$

Results of our calculations of the average power absorbed by the plexcitonic system, performed using formula (60), are shown in Fig. 12. The figure clearly demonstrates the phenomenon of induced transparency, i.e., it shows a pronounced dip in the light absorption spectrum at the resonant frequency. One can see that, with increasing coupling constant Ω, the depth of the dip and the distance between the positions of the spectral maxima increase.

It should be noted that, the induced transparency (IT) effect in plexcitonic nanoparticles, i.e., a pronounced dip in the light absorption spectrum, has a different physical nature than that of the effect of electromagnetically induced transparency (EIT), which has been intensively studied for many years in connection with its applications in nonlinear optics and quantum information science [287, 288]. The effect was discovered when exploring the laser radiation interacting with atomic gases. It consists of the elimination of absorption and refraction of light at the resonant transition frequency due to quantum interference between the photoexcitation pathways of the system. According to Fleischhauer et al. [287], the cause of the modified optical response of the medium in this case is the coherence of the atomic states induced by the laser field. The EIT effect is usually described in terms of the quantum dynamics of a three-level atom interacting with two external laser fields. One of them (probe) passes through the medium at a frequency close to that of the transition between the ground and excited states of the atom, and the frequency of the second (control) field is in resonance with the frequency of the transition between two excited states of the atom. Electromagnetic coupling in the system arises as a result of the interaction of the control field and the dipole moment of the transition between the excited states of the atom. A number of optical analogs of the EIT effect have been considered in the literature, including systems of two directly coupled microtoroidal silica resonators [288]. A discussion of these topics is given, for example, in Refs [286–289].

5.2.4 Fano formula and its limiting cases. As shown in Section 5.2.3, the coupled oscillator model successfully describes the resonance and antiresonance phenomena characterized by symmetrical and asymmetrical profiles, respectively, of the spectral peaks of the plexcitonic system, as well as the presence of a pronounced dip in the absorption spectrum associated with the induced transparency effect. In a series of well-known studies (see, for example, [285, 289, 290] and references therein), these phenomena were interpreted in terms of the quantum-mechanical Fano model [291]. Below, we will discuss whether it is justified to use such analogies. When comparing results obtained in the optics of plexcitonic nanostructures with the corresponding results of the Fano theory and its special cases, note that this theory was originally developed in atomic physics to describe the process of electron scattering on an atom in the presence of an autoionizing state. The result for the dimensionless quantity $\sigma(\mathcal{E})$ describing the shape of the resonance cross section has the form [291]

$$\sigma(\mathcal{E}) = \frac{(q+\epsilon)^2}{1+\epsilon^2}, \quad \epsilon = \frac{2(\mathcal{E}-\mathcal{E}_r)}{\Gamma_r}. \quad (61)$$

Here, $\mathcal{E}$ is the energy, $\mathcal{E}_r$ and Γ_r are the energy and width (FWHM) of the resonance in the continuous spectrum band in the Fano model. The cross-section profile in this model is primarily determined by the Fano asymmetry parameter, q.

Now we discuss the limiting cases of the Fano formula (Fig. 13) for the cross section profile $\sigma(\mathcal{E})$. For the discussion of the spectral behavior of the cross section for large values of the parameter q, it is also convenient to introduce a normalized cross section $\tilde{\sigma}(\mathcal{E})$ by the formula $\tilde{\sigma}(\mathcal{E}) = \sigma(\mathcal{E})/(1+q^2)$. It is evident from Fig. 13 that the degree of asymmetry of the profile changes with variation in the asymmetry parameter q. When $q = 0$, formula (61) describes a symmetrical dip in the light absorption cross section, which is sometimes called a quasi-Lorentz profile (Figs 13a and b). A typical asymmetric spectral profile appears at $q > 0$, as seen in Fig. 13a. This is the so-called Fano profile calculated for three values of $q = 0.5$, 1, and 2 (red, blue, and green curves, respectively). At $|q| \gg 1$, the asymmetry of the spectral profile manifests itself only in the low-intensity wing far from the resonance, $\mathcal{E} = \mathcal{E}_r$ $(\epsilon = 0)$. Meanwhile, in the vicinity of the resonance the profile becomes almost symmetric, as demonstrated by Fig. 13b at $q = 1000$. Thus, at $|q| \to \infty$, the Fano formula (61) transforms into the well-known formula [292] of the Breit–Wigner theory for resonant scattering,

$$\sigma(\mathcal{E}) \propto \frac{\Gamma_r/2}{(\mathcal{E}-\mathcal{E}_r)^2 + \Gamma_r^2/4},$$

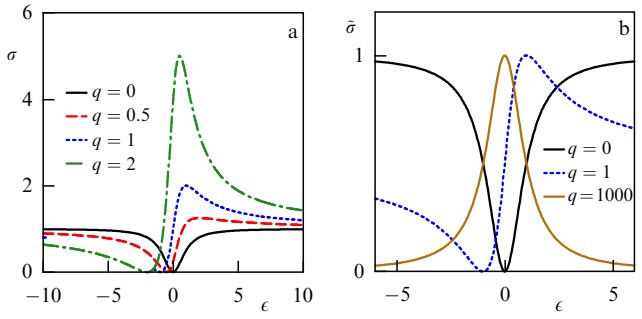

Figure 13. Dependence of the Fano cross-section profile (61), $\sigma(\epsilon) = (q+\epsilon)^2/(1+\epsilon^2)$, on dimensionless energy ϵ for different values of parameter q, which determines the asymmetry of the curve shape $\sigma(\epsilon)$ (Fig. 13a). Normalized curves, $\tilde{\sigma}(\epsilon) = \sigma(\epsilon)/(1+q^2)$, are shown in Fig. 13b. For $q = 0$, there is no asymmetry in the cross-section profile. Fano resonance has a maximum at $\epsilon = 1/q$ and a minimum at $\epsilon = -q$. The case $q \to \infty$ corresponds to Breit–Wigner resonance, when the shape of curve $\sigma(\epsilon)$ becomes symmetrical and is described by the Lorentz profile.

with a Lorentz contour that is symmetrical relative to the resonant energy $\mathcal{E}_r$ with a full width at half maximum Γ_r.

Although the available experimental and theoretical results on the optics of hybrid plexcitonic systems are often discussed in terms of the Fano model, its applicability for describing the behavior of the spectra in each individual case requires, generally speaking, a special analysis. The reason is that the original Fano theory for the autoionization of an atom deals with a purely discrete level against a continuum background [291]. In the optics of plexcitonic nanostructures, an accurate quantitative description of similar interference effects within the framework of the Fano model can be achieved only in the limit of an infinitely narrow excitonic band, $\gamma_{ex}/\gamma_{pl} \to 0$, corresponding to a purely discrete state in the theory [291]. When extending the results of Fano theory to plexcitonic systems with two resonances of finite width (plasmon and exciton), it should be borne in mind that, although the characteristic width of the excitonic resonance is significantly smaller than that of the plasmonic one ($\gamma_{ex} \ll \gamma_{pl}$), both widths must be taken into account when calculating the optical spectra of hybrid nanoparticles. Both widths are taken into account directly in the simple classical model of coupled oscillators and, especially, in exact calculations within the framework of the extended Mie theory or the FDTD method.

Note still that with the classical model of coupled oscillators (see expression (55) in Section 5.2.2), an approximate analytical formula for plexcitonic systems can be derived. To some extent it might be considered as an analogue of the simple expression (61) of the Fano theory. To derive this formula in the model of coupled oscillators, we assume that the driving force with frequency ω and amplitude F acts on plasmonic oscillator only. In addition, we take a rather small width of the exciton resonance equal to zero, $\gamma_{ex} = 0$. The peak of the plasmon resonance with a maximum frequency ω_{pl} and a sufficiently large width γ_{pl} is considered as the band of the continuous spectrum. Then, the square modulus of the corresponding amplitude of forced oscillations, $|c_{pl}(\omega)|^2$, takes the form

$$|c_{pl}(\omega)|^2 = \frac{|F/m|^2}{(\omega_{pl}^2 - \omega^2)^2 + \gamma_{pl}^2\,\omega^2}\,\frac{(q+\epsilon(\omega))^2}{1+\epsilon^2(\omega)}\,, \qquad (62)$$

where the effective parameter $\epsilon(\omega)$ can be written as

$$\epsilon(\omega) = \left(\omega^2 - \omega_{ex}^2 + \frac{\Omega^4(\omega_{pl}^2 - \omega_{ex}^2)}{(\omega_{pl}^2 - \omega_{ex}^2)^2 + \gamma_{pl}^2\omega_{ex}^2}\right) \times \frac{(\omega_{pl}^2 - \omega_{ex}^2)^2 + \gamma_{pl}^2\,\omega_{ex}^2}{\gamma_{pl}\,\omega_{ex}\Omega^4}\,, \qquad (63)$$

and the Fano asymmetry parameter is given by

$$q = \frac{\omega_{ex}^2 - \omega_{pl}^2}{\gamma_{pl}\omega_{ex}}\,. \qquad (64)$$

It follows that, in a general case, there is no direct analogy between the above approximate expressions of the coupled oscillator model and the simple Fano formula (61). In particular, formulas (63) and (64) for the parameters $\epsilon(\omega)$ and q explicitly include the frequencies of both the exciton, ω_{ex}, and plasmon, ω_{pl}, resonances. Despite the fact that in most cases the characteristic width of the excitonic resonance is significantly smaller than that of the plasmon one ($\gamma_{ex} \ll \gamma_{pl}$) it should be taken into account for the correct reproduction of the experimental data. However, in some cases, the approximate expressions (62)–(64) yield results that, to a certain extent, can be interpreted based on the simple Fano formula. This holds true, in particular, when the narrow excitonic peak is located far from the plasmon resonance peak on its wing. This is confirmed by comparing the results for the asymmetrical profile shown in Fig. 11b (the black curve in the vicinity of the right peak, calculated within the framework of the coupled oscillator model) with the asymmetrical Fano profile (Fig. 13a for $q = 1$ and $q = 2$). Another example is the dip in the light absorption spectrum shown in Fig. 11d. It occurs when the condition $\omega_{ex} \approx \omega_{pl}$ is met and corresponds to the dip in the Fano profile at $q = 0$ (Figs 13a and b).

5.3 Models of effective Hamiltonian

5.3.1 Simplest two-level model. To clarify the mechanism of the formation of optical spectra caused by coupling between Frenkel excitons and localized surface plasmons, we can also rely on an approach based on a suitable choice of the effective Hamiltonian of the metal/J-aggregate system. In the simplest case, when one plasmonic mode interacts with one excitonic mode, the effective Hamiltonian describing the effects of plexcitonic coupling in this system has the form

$$H = \begin{pmatrix} \mathcal{E}_{pl} & V \\ V^* & \mathcal{E}_{ex} \end{pmatrix}. \qquad (65)$$

Here, $\mathcal{E}_{pl} = \hbar\omega_{pl}$ is the energy of plasmon resonance, i.e., the position of the maximum of the peak in the photoabsorption spectrum of the metal core of the particle; $\mathcal{E}_{ex} = \hbar\omega_{ex}$ is the exciton energy, i.e., the position of the maximum of the absorption peak of the dye J-aggregate in formula (20); and V is the plexcitonic coupling energy. The eigenvalues of Hamiltonian (65), which determine the energies of the hybrid modes of the plexcitonic system, are given by

$$\mathcal{E}_{\pm} = \frac{1}{2}(\mathcal{E}_{pl} + \mathcal{E}_{ex}) \pm \frac{1}{2}\sqrt{(\mathcal{E}_{pl} - \mathcal{E}_{ex})^2 + 4|V|^2}\,. \qquad (66)$$

Formula (66) is similar to the well-known formula (90.9) in [292], which arises in calculating the electronic terms of a diatomic molecule in the vicinity of their quasi-crossing point in the presence of coupling between the diabatic potential

energy curves. If the excitonic absorption peak is in resonance with the peak maximum of the plasmonic subsystem, $\mathcal{E}_{\rm pl} = \mathcal{E}_{\rm ex}$, then formula (66) yields an expression for the splitting energy of the hybrid modes,

$$\Delta\mathcal{E} = \mathcal{E}_+ - \mathcal{E}_- = 2|V|\,. \tag{67}$$

In other words, this directly gives the constant $V \equiv \hbar g$ of the near-field plexcitonic coupling in composite nanoparticles in the absence of losses. The value of the constant g can thus be found experimentally by measuring the splitting energy of the spectral peaks of the plexcitonic resonances, $\Delta\mathcal{E}$.

Following well-known studies [108–110, 129] on exciton-plasmon-polariton coupling in cavities, the energy splitting of $\Delta\mathcal{E}$ in formula (67) is often interpreted in terms of the Rabi splitting energy, $\Delta\mathcal{E} = \hbar\Omega_{\rm R} = 2\hbar\,|g|$, in the absence of energy dissipation in a plexcitonic nanosystem. However, the value of $\Omega_{\rm R}$, expressed through the constant g, reflects the scale of the plexcitonic coupling between the subsystems, and it does not depend on the external field strength. It is associated with vacuum field fluctuations and correspond to the so-called Rabi vacuum frequency [141]. Thus, the physical meaning of the value of $\Omega_{\rm R}$ for plexcitonic systems differs from the standard definition of the Rabi frequency, $\Omega_{\rm R} = 2|\mathbf{d}_{fi}\mathbf{E}|/\hbar$, written for a two-level atom interacting with external resonant radiation field ($\mathbf{d}_{fi}$ is the matrix element of the dipole moment of the $|i\rangle \to |f\rangle$ transition).

5.3.2 Damping in a plexcitonic system. One can include losses associated with plasmon, $\gamma_{\rm pl}$, and exciton, $\gamma_{\rm ex}$, damping into the theoretical consideration presented in the previous section. To this end, the energies of the plasmonic and excitonic subsystems should be represented as complex quantities, $\mathcal{E}_{\rm pl} \to \mathcal{E}_{\rm pl} - {\rm i}\hbar\gamma_{\rm pl}/2$ and $\mathcal{E}_{\rm ex} \to \mathcal{E}_{\rm ex} - {\rm i}\hbar\gamma_{\rm ex}/2$, respectively. The use of the coupled oscillator model leads to the well-known formula

$$\mathcal{E}_\pm = \hbar\omega_\pm = \frac{\hbar}{2}\left[\omega_{\rm pl} + \omega_{\rm ex} - {\rm i}\left(\frac{\gamma_{\rm pl}}{2} + \frac{\gamma_{\rm ex}}{2}\right)\right] \pm \frac{\hbar}{2}\sqrt{4|g|^2 + \left[\delta + {\rm i}\left(\frac{\gamma_{\rm pl}}{2} - \frac{\gamma_{\rm ex}}{2}\right)\right]^2}\,, \tag{68}$$

used in many papers on plexcitonic coupling (see [153, 293] and references therein). Here, $g = V/\hbar$ is the plasmon-exciton coupling constant introduced above, $\omega_{\rm pl}$ and $\omega_{\rm ex}$ are the eigenfrequencies of the plasmon and exciton, and $\delta = \omega_{\rm pl} - \omega_{\rm ex}$ is their detuning. The same expression can be obtained for the complex eigenvalues of the Hamiltonian

$$\mathcal{H} = \hbar\begin{pmatrix} \omega_{\rm pl} - \dfrac{{\rm i}\gamma_{\rm pl}}{2} & g \\ g^* & \omega_{\rm ex} - \dfrac{{\rm i}\gamma_{\rm ex}}{2} \end{pmatrix}. \tag{69}$$

Formula (68) is in accordance with the Jaynes–Cummings quantum-optical model [294]. The real parts of the eigenfrequencies are determined by the expressions [295]

$${\rm Re}\,\{\omega_\pm\} = \frac{\omega_{\rm pl} + \omega_{\rm ex}}{2} \pm \frac{1}{2}\left[(\gamma_{\rm pl} - \gamma_{\rm ex})^2\delta^2 + \left(4|g|^2 + \delta^2 - \frac{(\gamma_{\rm pl} - \gamma_{\rm ex})^2}{4}\right)^2\right]^{1/4} \times \cos\left[\frac{1}{2}\arctan\left(\frac{4(\gamma_{\rm pl} - \gamma_{\rm ex})\,\delta}{16g^2 + 4\delta^2 - (\gamma_{\rm pl} - \gamma_{\rm ex})^2}\right)\right]. \tag{70}$$

In the special case of zero detuning, when $\delta = 0$ and $\omega_{\rm pl} = \omega_{\rm ex}$, this expression takes particularly simple form [296]

$$\Delta\omega = {\rm Re}\,\{\omega_+ - \omega_-\} = 2{\rm Re}\left\{\sqrt{|g|^2 - \frac{(\gamma_{\rm pl} - \gamma_{\rm ex})^2}{16}}\right\}. \tag{71}$$

Consequently, the hybrid modes of the plexcitonic system (upper ($\mathcal{E}_+$) and lower ($\mathcal{E}_-$) branches) have the following values of complex energy:

$$\mathcal{E}_\pm = \mathcal{E}_0 \pm \frac{1}{2}\sqrt{4|V|^2 - \frac{\hbar^2}{4}(\gamma_{\rm pl} - \gamma_{\rm ex})^2} - {\rm i}\,\frac{\hbar}{4}(\gamma_{\rm pl} + \gamma_{\rm ex})\,, \quad \mathcal{E}_0 \equiv \mathcal{E}_{\rm pl} = \mathcal{E}_{\rm ex}\,. \tag{72}$$

The emergence of the strong coupling regime can be determined by the positive value of the splitting energy of the hybrid modes (+) and (−). According to (71) and (72), this corresponds to the fulfillment of the condition

$$2|g| > \frac{|\gamma_{\rm pl} - \gamma_{\rm ex}|}{2}\,. \tag{73}$$

Here, short-wavelength (+) and long-wavelength (−) resonance peaks appear in the optical spectra. The scale of the coupling constant is often discussed in terms of this frequency, which, with minor losses, reaches the value $\Delta\omega = 2|g|$. On the contrary, if the value of g is sufficiently small, then the hybrid modes (+) and (–) do not split, and there is no point discussing the scale of the value of g in terms of the splitting $\Delta\omega$.

5.3.3 Multilevel models of plexcitonic coupling. A number of problems in the optics of plexcitonic nanosystems require the use of models of multiple coupled oscillators, which are equivalent to models of a multilevel effective Hamiltonian. In particular, these include problems concerning the interaction of a Frenkel exciton with several multipole (dipole, quadrupole, octupole, etc.) plasmons in the Ag/J-aggregate [89] and Au/J-aggregate [118] systems. Another example is strong plexcitonic coupling in the Ag/J-aggregate/WS_2 nanostructure between excitons in the WS_2 monolayer, excitons in the J-aggregate layer, and localized surface plasmons of a silver nanoprism. A mathematical description of this problem was given in [108] using a model of three coupled oscillators. Another example is the problem of strong coupling between quasi-degenerate Frenkel exciton modes in the outer organic shell of a dye and multiple plasmon modes in plexcitonic dimers consisting of a pair of nanoparticles with a silver spherical or disk-shaped core coated with a layer of a J-aggregate [297–299]. Strong plexcitonic coupling in such systems [299] results in replication of spectral bands. This band replication leads to the emergence of twice the number of plasmon-exciton spectral bands (compared to the case of a purely plasmon dimer) and narrow peaks associated with resonances of the J-aggregate shell. This phenomenon was described in [299] using the FDTD method and interpreted within the framework of the model of multiple coupled oscillators and the equivalent method of a multilevel effective Hamiltonian.

5.4 Plasmon-exciton coupling regimes

Interaction of plasmons with excitons can result in various regimes of plexcitonic coupling, which lead to a qualitatively different behavior of the optical spectra of composite

nanosystems containing metal and excitonic components. The efficiency of plexcitonic coupling strongly affects absorption and emission properties of metalorganic nanosystems [293, 300]. The realization of a particular coupling regime depends on a number of factors, the most important of which are (i) the difference between unperturbed eigenfrequencies of the plasmon and exciton, $\delta \equiv \Delta\omega_{\text{pl–ex}} = \omega_{\text{pl}} - \omega_{\text{ex}}$; (ii) the effective strength f of the excitonic oscillator at the transition in the J-band of the dye; (iii) the widths of plasmon (γ_{pl}) and excitonic (γ_{ex}) resonances; and (iv) the sizes of plasmonic and excitonic subsystems. The classification of plexcitonic coupling regimes has been presented in a number of papers (see [67, 301–303] and references therein). Most of them usually distinguish between weak, strong, and ultrastrong coupling regimes.

5.4.1 Weak plexcitonic coupling. Obviously, the condition determining the weak plexcitonic coupling should be opposite in its physical meaning to that of strong coupling. Then, using equation (73), in the case of coincidence of resonance frequencies ($\omega_{\text{pl}} = \omega_{\text{ex}}$), we obtain

$$|g| \ll \frac{|\gamma_{\text{pl}} - \gamma_{\text{ex}}|}{4} . \tag{74}$$

Sometimes this condition is formulated in such a way that the constant g is less than one quarter of the damping constants, $|g| \ll \gamma_{\text{pl}}/4$ or $|g| \ll \gamma_{\text{ex}}/4$, in the weak coupling regime. The interaction ($V = \hbar g$) between the subsystems then leads to relatively weak perturbations of the plasmon mode and excitonic state. In this case, small shifts occur in the positions of the corresponding resonance spectral peaks relative to the unperturbed frequencies of the plasmon (ω_{pl}) and the exciton (ω_{ex}). Then, the spectrum of the composite plexcitonic nanoparticle is close to a superposition of the spectra of its metal and J-aggregate subsystems. Weak coupling of plasmons with the organic or inorganic (molecular or excitonic) component of the nanostructure leads to such well-known physical phenomena as surface-enhanced Raman scattering (SERS [75, 304–306]), plasmon-induced photoabsorption [307] and fluorescence [308, 309], and fluorescence quenching [310].

5.4.2 Strong plexcitonic coupling. The strong plexcitonic coupling regime turns out to be quite attractive for applications. It arises when the near-field plasmon-exciton coupling energy exceeds the average dissipation energy in the system, and new hybrid plexcitonic states of the composite system are formed, with physical properties that neither its plasmonic nor excitonic components possess [311, 312]. In the frequency domain, this situation can be described as splitting of the dispersion curves of the unperturbed plasmon and exciton modes resulting in the formation of new hybrid states of the composite system. The quantum analogue of this phenomenon consists in splitting of the adiabatic curves of the potential energy of a diatomic molecule in the vicinity of the crossing point of the diabatic curves [292]. In the time domain, the formation of hybrid modes in the strong coupling regime manifests itself as a coherent energy exchange between the excitonic and plasmonic subsystems [129, 313]. Such effects were analyzed, in particular, for metal/J-aggregate composite nanogratings [129] and for quantum dots in the gap of metal dimers [313]. However, most experimental works on the optics of plexcitonic nanoparticles studied only various spectral manifestations of plexcitonic effects rather than the temporal dynamics in the strong coupling regime.

A rigorous criterion of strong coupling depends somewhat on the context and a particular area of physics. In various papers [93, 114, 122, 301, 314], this condition is written in different forms. The following two conditions seem to be the most significant from a physical point of view [114,138]:

$$|g| > \frac{|\gamma_{\text{pl}} - \gamma_{\text{ex}}|}{4} , \quad |g|^2 > \frac{\gamma_{\text{pl}}^2 + \gamma_{\text{ex}}^2}{8} . \tag{75}$$

The first condition means that the strong coupling regime arises when the value defined by expression (71), $\Delta\omega = 2[|g|^2 - (\gamma_{\text{pl}} - \gamma_{\text{ex}})^2/16]^{1/2}$, is real. However, the term 'strong coupling' is often formulated in a purely empirical way: the system is in the strong coupling regime whenever Rabi splitting is observed experimentally [141]. As noted in [315], for the experimental observation of the strong coupling regime, a more rigorous condition must be met: the minimum distance between the upper and lower energy branches must be larger than the average width of the plasmon and exciton resonances:

$$\Delta\mathcal{E} = \text{Re}\,\{\mathcal{E}_+ - \mathcal{E}_-\} > \hbar\,\frac{\gamma_{\text{pl}} + \gamma_{\text{ex}}}{2} .$$

Both of these strong coupling criteria are illustrated in Fig. 14, which shows the results of calculations using formula (72) for the energies ($\mathcal{E}_+$ and $\mathcal{E}_-$) of the hybrid modes of the plexcitonic system as functions of the coupling energy $V = \hbar g$. One can see that, under the condition $\hbar g < \hbar g_- = \hbar|\gamma_{\text{pl}} - \gamma_{\text{ex}}|/4$, there is no mode splitting, and the effect of plexcitonic coupling is manifested only in a small change in the width of a single spectral peak. With increasing interac-

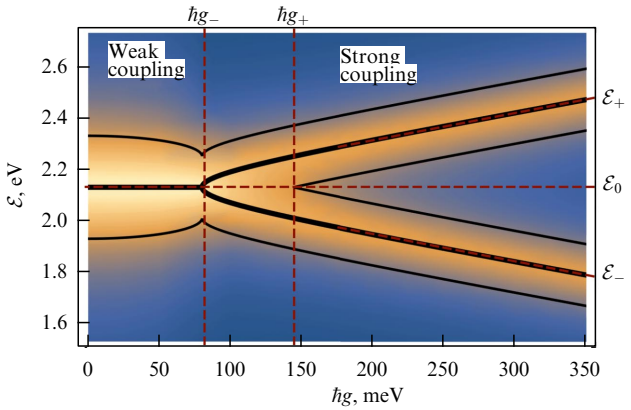

Figure 14. Schematic view of hybrid modes demonstrating the transition from the weak to strong coupling regime in a plexcitonic system with a change in coupling energy $V = \hbar g$. Calculations were performed using formula (72) for the complex energy $\mathcal{E}$ at $\mathcal{E}_0 = \mathcal{E}_{\text{pl}} = \mathcal{E}_{\text{ex}}$, taking into account the full width at half maximum (FWHM) of plasmon ($\hbar\gamma_{\text{pl}}$) and exciton ($\hbar\gamma_{\text{ex}}$) resonances. Thick black curves show positions of maxima in the energy spectrum of the system. Split upper and lower plexcitonic branches correspond to values of $\mathcal{E}_+$ and $\mathcal{E}_-$ in formula (72). Vertical dashed lines indicate coupling energy values that meet rigorous mathematical, $g > g_- = (\gamma_{\text{pl}} - \gamma_{\text{ex}})/4$, and semiempirical, $g > g_+ = [(\gamma_{\text{pl}}^2 + \gamma_{\text{ex}}^2)/8]^{1/2}$, criteria for the occurrence of the strong coupling regime in the system. The following parameters were chosen in calculations: $\mathcal{E}_0 = 2.13$ eV, $\hbar\gamma_{\text{pl}} = 400$ meV, $\hbar\gamma_{\text{ex}} = 80$ meV.

tion energy, the plexcitonic branches (+) and (−) split starting with $hg = hg_-$. However, as follows from Fig. 14, these branches become clearly distinguishable at higher values of $\hbar g$, which obviously satisfies the above-formulated semi-empirical criterion,

$$\hbar g \gtrsim \hbar g_+ = \hbar\sqrt{\frac{\gamma_{\rm pl}^2 + \gamma_{\rm ex}^2}{8}}\,.$$

The dip in the spectra of plexcitonic particles, which is directly related to the splitting of the hybrid modes (+) and (−) with an increase in the constant g, occurs in the strong coupling regime according to the mathematical criterion $|g| > |\gamma_{\rm pl} - \gamma_{\rm ex}|/4$. Moreover, several experimental studies [91, 92, 318] have demonstrated that a decrease in the efficiency of plexcitonic coupling first leads to a decrease in the depth of the dip and eventually to its complete disappearance. This is also confirmed by numerical calculations within the framework of the extended Mie theory. For example, in [116, 119], the efficiency of the near-field coupling between the metal core and the outer J-aggregate shell in three-layer metalorganic nanoparticles decreased due to an increase in the intermediate dielectric layer thickness $\ell_{\rm s}$. In this context, it should be emphasized that the phenomenon of induced transparency in plexcitonic nanoparticles, which fully corresponds to the phenomenon of a dip in the light absorption spectra, definitely takes place in the strong coupling regime. To avoid any misunderstandings, we note that the EIT phenomenon, as already noted in Section 5.2.3, has a different physical nature. Therefore, the fact that the EIT phenomenon pertains to the weak coupling regime (see, for example, [289]) does not contradict the interpretation of induced transparency of plexcitonic particles as a manifestation of the strong coupling regime.

5.4.3 Ultrastrong plexcitonic coupling. In the case of strong plexcitonic coupling, the ultrastrong coupling regime is often singled out, which is characterized by an even greater value of the interaction constant g of the plasmon with the exciton under conditions of coincidence of the frequencies of the plasmon and exciton resonances, $\omega_0 = \omega_{\rm ex} = \omega_{\rm pl}$. In the ultrastrong coupling regime, the constant g reaches values greater than or on the order of one tenth of the resonant frequency of the oscillators, ω_0. Consequently, the frequencies of the hybrid modes of the plexcitonic system, ω_+ and ω_-, differ significantly from the eigenfrequencies of the subsystems, ω_0. In this situation, when describing the interaction of the hybrid system with incident light having a frequency ω from the same spectral range as the original eigenfrequencies ω_0, in addition to the standard resonant contribution to the polarizability of the composite system, $\alpha_{\rm R} \propto (\mathcal{E}_\pm - \hbar\omega)^{-1}$, one should also take into account the nonresonant contribution, $\alpha_{\rm NR} \propto (\mathcal{E}_\pm + \hbar\omega)^{-1}$, which is usually assumed to be negligibly small compared to the resonant one. A consistent approach to taking into account both contributions to the polarizability is presented in monograph [249] (see formula (3.2.23) and its derivation).

The realization of this regime in hybrid metalorganic plexcitonic nanosystems was noted in a number of papers [69, 91, 316–319]. A strict analytical criterion determining the occurrence of the ultrastrong plexcitonic coupling regime, to the best of our knowledge, has not yet been established. Nevertheless, the authors of the above-mentioned papers showed that this regime is achieved when the constant g is 7–10% of the frequency ω_0. In this situation, the value of splitting of the spectral peaks of the hybrid modes on the frequency scale, called the Rabi frequency $\Omega_{\rm R}$, exceeds approximately 15–20% of the frequency ω_0. A certain idea of the efficiency of plasmon-exciton interaction in composite

Table 3. Splitting energies $\Delta\mathcal{E} = {\rm Re}\,\{\mathcal{E}_+ - \mathcal{E}_-\}$ of hybrid modes of a number of composite nanostructures, which determine, in accordance with (71), characteristic values of plexcitonic coupling constant $g \approx \Delta\mathcal{E}/(2\hbar)$. Many studies on plexcitonics, when discussing strong and ultrastrong coupling regimes, refer to $\Delta\mathcal{E}$ as Rabi splitting energy $\hbar\Omega_{\rm R}$.

$\Delta\mathcal{E}$, meV	Shape	Composition	References
155	Nanorod array	Au/Dye(CAS RN 27268-50-4)	Wurtz et al., 2007 [115]
180	Dye aggregates on silver film	Ag/TDBC	Bellessa et al., 2004 [96]
187	Right-handed nanorod dimer	Ag/TDBC	Zhu et al., 2021 [332]
199	Right-handed nanorod	AgAu alloy/TDBC	Cheng et al., 2023 [335]
202	Left-handed nanorod dimer	Ag/TDBC	Zhu et al., 2021 [332]
205	Left-handed nanorod	AgAu alloy/TDBC	Cheng et al., 2023 [335]
207	Nanoprism	Ag/PIC	DeLacy et al., 2015 [92]
214	Nanorod	Au/Ag/TDBC	Wu et al., 2021 [315]
260	Nanostars	Au/JC1(CAS RN 3520-43-2)	Melnikau et al., 2013 [127]
265	Nanorods	Au/JC1(CAS RN 3520-43-2)	Melnikau et al., 2016 [153]
350	Nanodisk	Ag/TDBC	Balci et al., 2019 [318]
377	Nanocubes	Au/PIC	Song et al., 2019 [70]
400	Nanoprism	Ag/TDBC	Balci et al., 2013 [91]
412	Silver film with nanoholes	Ag/H_4TPPS	Salomon et al., 2013 [90]
450	Nanodisk array	Ag/TDBC	Bellessa et al., 2009 [87]
550	Nanodisk	Ag/Heptamethine	Todisco et al., 2018 [69]
700	Dye molecules in a low-Q resonator	Ag/PMMA/Spiropyran	Schwartz et al., 2011 [319]

metalorganic nanosystems of various compositions and shapes can be obtained from Table 3, which lists the values of the splitting energy of the spectral peaks ($\Delta\mathcal{E} = \hbar\Omega_R = 2\hbar|g|$) in the strong and ultrastrong coupling regimes.

6. Absorption, scattering, and extinction spectra of two-layer metalorganic 'core–shell' nanospheres

6.1 Near-field coupling of Frenkel exciton with dipole and multipole plasmons

There are a lot of studies devoted to the synthesis, structure, and spectral characteristics of hybrid nanoparticles of various shapes and sizes, consisting of a metal core and an outer shell of ordered molecular J-aggregates of dyes. They include studies on two-layer metalorganic nanoparticles of spherical shape [63, 65–67, 81, 89, 117–119, 126, 174, 320–326]. There are also a series of experimental and theoretical papers on composite nanoparticles with a metal core and a J-aggregate shell of a more complex geometric shapes, such as spheroidal [122, 327], rod-like [68, 115, 125, 133, 134, 153, 315], and dumbbell-like [94], as well as on composite nanoparticles in the shape of disks [131, 183, 318], triangular prisms [91–93, 328, 329], and stars [95, 127, 128, 329]. Most of the experiments were performed for particles with a gold or silver core coated with one of the cyanine dyes capable of aggregating on the surface of the metal core. These studies draw a fairly complete picture of the nature and main regularities in the absorption and scattering spectra of light by Ag/J-aggregate and Au/J-aggregate nanoparticles under various regimes of near-field coupling between Frenkel excitons and localized surface plasmon-polaritons in hybrid nanoparticles of various sizes and shapes with different optical constants of the metal core and J-aggregate shell.

It is important to note here that, although the shape of hybrid particles has a significant effect on the behavior of their absorption, scattering, and luminescence spectra, many important consistent patterns can already be demonstrated using the example of nanospheres. First we discuss the behavior of the extinction spectra of small-radius metal/J-aggregate nanospheres in an aqueous solution. The corresponding experimental data [174] for silver and gold particles coated with a J-aggregate of the cyanine dye TC with a small core radius $r_1 = 5$ nm and a shell thickness $l_J = 1$ nm are shown in Fig. 15.

In both cases, the behavior of the absorption spectra is affected by the interaction of Frenkel excitons in the outer shell with plasmons localized in the metal core. However, the behavior of these spectra is qualitatively different for Ag/TC and Au/TC particles, reflecting two different regimes (weak and strong) of plexcitonic coupling. For Ag/TC particles, the absorption spectrum of the plexcitonic system is close to a superposition of the spectra of the plasmon resonance and the excitonic J-band of the molecular aggregate. This corresponds to the weak plexcitonic coupling regime arising in the process of light–matter interaction. This is due to the fact that the positions of the maxima of the unperturbed peaks of the plasmon ($\lambda_{pl}^{(Ag)} = 384$ nm) and exciton ($\lambda_{ex} = 475$ nm) resonances are located quite far from each other on the wavelength scale (see Fig. 8). It is a qualitatively different situation for Au/TC particles, with a pronounced dip in the absorption spectrum of the composite particle appearing in the vicinity of the resonance frequency of the J-band of the

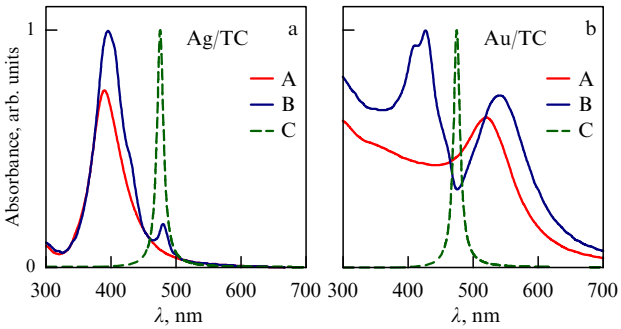

Figure 15. Experimental data [174] on light absorption spectra of hybrid spherical (a) Ag/TC and (b) Au/TC nanoparticles consisting of a metal core (Ag or Au) and a thin J-aggregate layer of TC dye as functions of light wavelength in vacuum (blue curves, B). Red curves (A) in panels (a) and (b) demonstrate corresponding results on light absorption spectra of bare silver and gold cores of these particles. Green dashed curves (C) describe the peak of absorption J-band of TC dye aggregate. Radius of core is $r = 5$ nm; particles are in an aqueous solution.

dye aggregate. The dip can be considered as a vivid example of the strong plexcitonic coupling regime, which arises because the resonance frequencies of the unperturbed plasmonic ($\lambda_{pl}^{(Au)} = 525$ nm) and excitonic subsystems in the case of Au/TC are significantly closer to each other ($|\Delta\lambda| = 50$ nm) than those in the case of Ag/TC ($|\Delta\lambda| = 91$ nm). The presence of a peak or dip near frequencies corresponding to the J-band of the absorption of the TC aggregate is interpreted in [63] as a result of, respectively, constructive and destructive interference of the contributions of the plasmonic and excitonic subsystems to the resulting spectrum of the hybrid particle. Due to the small total size of the Ag/TC and Au/TC nanospheres, in the experiments [174], the behavior of the spectra under consideration is almost entirely determined by the near-field coupling between the Frenkel exciton and the electric dipole plasmon, and the role of higher-order multipoles ($n > 1$) is insignificant.

Calculations for two-layer Ag/TC and Au/TDBC nanospheres [89, 118] show that the situation changes dramatically with a significant increase in the total particle size. Then, the near-field coupling of the Frenkel exciton not only with the dipole but also with higher-order ($n > 1$) multipole plasmons (especially with the quadrupoles and octupoles) plays a significant role in the formation of the optical spectra of hybrid plexcitonic nanoparticles. We demonstrate this effect by calculating the extinction spectra of light by hybrid Ag/TDBC particles within the framework of the Mie theory (Fig. 16). The thickness of the excitonic shell is chosen to be fairly large, $l_J = 8$ nm, so that there are sufficiently strong grounds to justify the scalar 'isotropic' model (20) used to describe the dielectric function $\varepsilon_J(\omega)$ of the excitonic J-aggregate shell of a particle. The following parameters of the TDBC J-aggregate were used in the calculations: $\hbar\omega_{ex} = 2.12$ eV ($\lambda_{ex} = 585$ nm), $\gamma_{ex} = 48$ meV, $f_J = 0.44$, and $\varepsilon_J^{\infty} = 2.3$ [99]. Following papers [89, 251, 299], the dielectric function of the metal core was calculated taking into account the size effect (see Section 2 and formula (9)). The radius r_1 of the silver core was chosen to be 12, 32, 52, and 92 nm.

The formation of the light absorption spectrum of a small-radius Ag/TDBC particle is almost entirely determined by the interaction of the Frenkel exciton with the electric dipole plasmon ($n = 1$). This is shown in Fig. 16a for a particle with outer radius $r_2 = 20$ nm. According to the analytical model

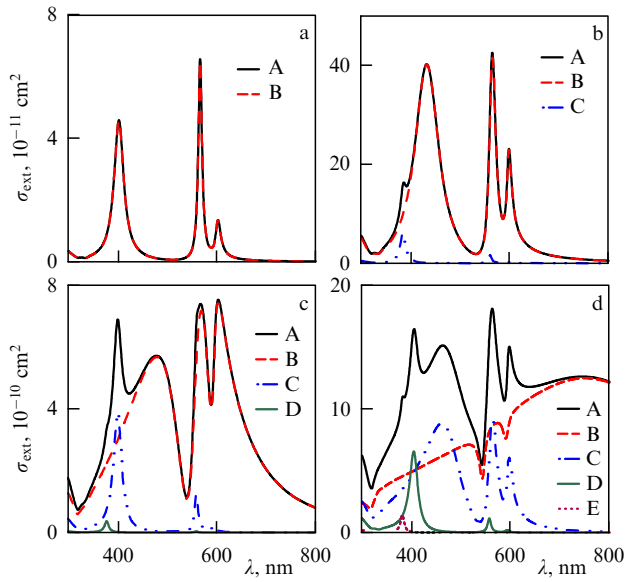

Figure 16. Spectral dependences of light extinction cross sections σ_{ext} by two-layer nanospheres consisting of a silver core and an outer J-aggregate shell of TDBC dye. Calculations were performed within framework of extended Mie theory [148] for four sets of inner and outer radii of the particle: (a) $r_1 = 12$ nm, $r_2 = 20$ nm; (b) $r_1 = 32$ nm, $r_2 = 40$ nm; (c) $r_1 = 52$ nm, $r_2 = 60$ nm; and (d) $r_1 = 92$ nm, $r_2 = 100$ nm. Red, blue, green, and dark magenta curves show, respectively, contributions of dipole ($n = 1$, B), quadrupole ($n = 2$, C), octupole ($n = 3$, D), and hexadecapole ($n = 4$, E) terms to general formula (26) of multipole expansion. Solid black curve (A) is their sum.

(see Section 5.1), when molecular aggregates are isotropically oriented in the organic shell, three pronounced maxima are formed in the extinction spectrum. The left plexcitonic peak appears at a wavelength of $\lambda = 402$ nm near the position of the dipole plasmon resonance of the bare silver core, $\lambda_{pl} = 389$ nm, and turns out to be shifted relative to it toward longer wavelengths by $\Delta\lambda = 13$ nm. In the vicinity of the excitonic transition frequency of the TDBC J-aggregate ($\lambda_{ex} = 585$ nm), two split plexcitonic peaks appear in the cross section at $\lambda = 566$ nm and 603 nm, whose maxima differ substantially from each other in intensity:

$$\frac{\sigma_{ext}^{(left)}}{\sigma_{ext}^{(right)}} = 4.86\,.$$

With increasing outer radius of the particle to $r_2 = 40$ nm (Fig. 16b), a small contribution to the extinction comes from the quadrupole term (blue curve), which leads to the emergence of a weak peak in the total cross section, σ_{ext} (black curve), in the region of $350 \lesssim \lambda \lesssim 400$ nm. The plexcitonic effect manifests itself as a deep dip (at $\lambda = 586$ nm) between two peaks of different intensities,

$$\frac{\sigma_{ext}^{(left)}}{\sigma_{ext}^{(right)}} = 1.84\,,$$

near the position of the maximum of the TDBC J-band, $\lambda_{ex} = 588$ nm. Further increase in the outer radius to $r_2 = 60$ nm leads in the range of $350 \lesssim \lambda \lesssim 450$ nm to a very significant modification of the extinction spectrum as a result of the influence of the quadrupole term (Fig. 16c). Here, in comparison with the previous case (Fig. 16b), the intensities of the middle and right dipole plexcitonic peaks in the extinction spectrum are equalized, and the relative depth of the dip between the left and middle dipole peaks decreases. In addition to this, in the vicinity of $\lambda = 380$ nm, the contribution of the octupole term (green curve) becomes noticeable, which, however, does not lead to a significant change in the behavior of the total extinction cross section.

The behavior of the spectrum of the Ag/TDBC plexcitonic particle changes drastically at $r_2 = 100$ nm (Fig. 16d). First of all, of particular interest is an increase in the total number (6 pieces) of spectral peaks due to the growth of the contribution to the cross section of the quadrupole and octupole resonances. In this case, the peak position shifts strongly to the long-wavelength region and is $\lambda_{max} = 751$ nm due to the interaction of the exciton with the dipole plasmon. The cross section values in this region ($\lambda \gtrsim 650$ nm) can be reproduced quite well taking into account only the dipole term in the Mie expansion. On the contrary, the behavior of the spectrum in the region $\lambda \lesssim 650$ nm is mainly determined by the contribution of multipole resonances.

6.2 Role of size effects

Below is a summary of the main results clarifying the influence of size effects on the optical properties of metal nanoparticles coated with a thin layer of a dye molecular aggregate. The specific manifestation of these effects is determined by several factors. Previously, in Section 2, we demonstrated the importance of the size effect to describe the dielectric function of the noble metal core of a hybrid nanoparticle, associated with the scattering of free electrons at the metal/J-aggregate interface. This effect has been shown to be particularly strong if the particle size is significantly smaller than the mean free path of electrons (l_∞) in bulk silver or gold samples. In addition, as follows from quasistatic approximation formulas (33) and (36), the dipole polarizability (α) of the hybrid particle, and hence the absorption (σ_{abs}) and scattering (σ_{scat}) cross sections, strongly depend on this particle's overall radius (since $\alpha \propto r_2^3$) and on the value of the ratio (r_1/r_2) of the inner and outer radii of the concentric spheres due to the near-field coupling between the core and the shell. Beyond the applicability of the quasistatic approximation (i.e., for $kr \gtrsim 1$), a further significant increase in the outer radius of the hybrid nanoparticle leads to more complex dependences of the spectra on its geometric parameters than those predicted by simple expressions (33) and (36). This is demonstrated for two-layer Ag/J-aggregate nanoparticles by direct calculations [117] of the cross sections within the framework of the extended Mie theory using the size- and frequency-dependent dielectric function of the silver core and the standard isotropic model (20) for the dielectric function of the J-aggregate shell.

For particles with core radii $r_1 = 10$ nm and $r_1 = 30$ nm, it was found that, when the thickness of the J-aggregate shell l_J varies from 1 nm to 12 nm, the positions and intensities of the spectral photoabsorption peaks change significantly even in the case of relatively small changes in the thickness of the outer excitonic layer.

It was also shown that the intensities of the spectral peaks increase substantially with increasing external particle size, mostly due to an increase in its total volume $\mathcal{V} = 4\pi r_2^3/3$. In addition, with a significant increase in the particle size, the behavior of the absorption spectra becomes more complex due to an increase in the total number of spectral peaks (see Fig. 16). It is caused by the effects of the interaction of the Frenkel exciton in the organic shell not only with the electric dipole but also with the multipole (quadrupole, octupole, etc.)

localized plasmons in the metal core of the particle [89]. In a certain range of nanoparticle sizes, when the contributions of the absorption and scattering processes to the resulting total extinction cross section become of the same order, the spectral behavior of the value of $\sigma_{\rm ext}(\lambda)$ is additionally affected by the competition of the contributions of these processes. For silver particles coated with a thin layer of J-aggregate of the dye, the extinction cross section is mainly determined by the light absorption process at an outer radius less than 25–35 nm, while at larger values of the radius, the contribution of the scattering process begins to dominate. For hybrid particles with a gold core, the scattering process becomes predominant at outer particle radius $r_2 \gtrsim 55$–60 nm.

7. Optical spectra of three-layer metalorganic nanospheres

7.1 Absorption and luminescence spectra

The authors of Refs [88, 323] and [68, 115, 330] synthesized three-layer nanoparticles of various geometric shapes and sizes, consisting of a gold or silver core, an outer J-aggregate shell of a cyanine dye (TC, PIC, TDBC, etc.), and an organic spacer layer between them. When interacting with an external electromagnetic field, the spacer acts as a passive dielectric layer between two active layers of the nanoparticle: the core with localized surface plasmons and the outer excitonic shell [116, 119, 251, 299]. Varying the thickness of the interlayer provides an additional opportunity to affect the magnitude and features of the plexcitonic coupling between the core and shell and, thereby, modify the spectral characteristics of the hybrid system compared to two-layer metal/J-aggregate particles.

The key difference between three-layer metalorganic nanoparticles with a passive spacer layer and two-layer particles is that their interaction with light can result in not only absorption and scattering processes but also photoluminescence. This is demonstrated in Fig. 17, which presents experimental data [323] on the absorption and photoluminescence spectra of a colloidal solution of hybrid three-layer Au/TMA/TC nanospheres (solid red curves), as well as on the absorption spectrum of a two-layer Au/TMA particle without an external J-aggregate layer (dashed curve). Note that two plexcitonic peaks are observed in the absorption spectrum of Au/TMA/TC nanoparticles: a sharp one at $\lambda = 459$ nm and a broader one at $\lambda = 526$ nm. It is important to stress that this experiment demonstrated fairly intense photoluminescence of three-layer Au/TMA/TC nanospheres with a maximum in the emission spectrum at $\lambda = 469$ nm (see Fig. 17), which the authors of paper [323] attributed to the luminescence of the TC J-aggregate. In contrast, for two-layer Au/TC nanoparticles, in which the gold cores were coated directly with the J-aggregate, corresponding luminescence was not observed. This fundamental difference was explained in [323] by the quenching of luminescence due to the processes of excitation energy transfer from the J-aggregate shell to the metal core. Such quenching can be quite effective in two-layer nanoparticles, but is significantly suppressed in three-layer nanoparticles due to the presence of an intermediate passive TMA spacer. The presence of photoluminescence in addition to the process of light absorption by three-layer nanoparticles was also observed for a number of other dyes that form an external J-aggregate shell. The corresponding examples include Au/TMA/PIC,

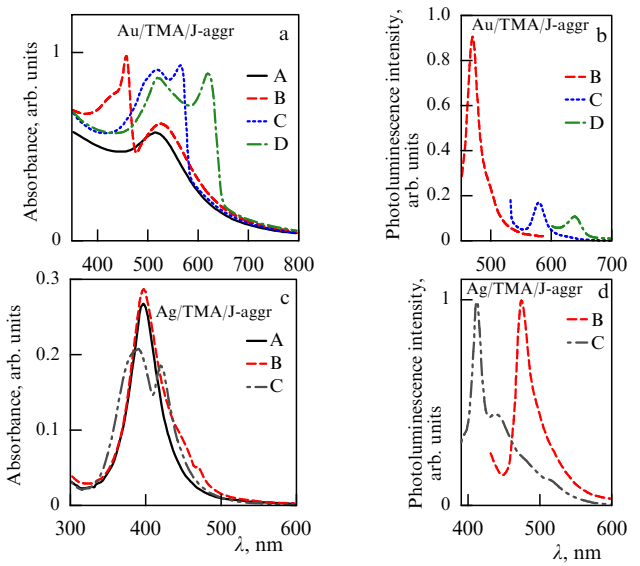

Figure 17. Experimental data on (a, c) absorption and (b, d) photoluminescence spectra of colloidal solutions containing three-layer metal/spacer/J-aggregate nanospheres. Core material was (a, b) gold and (c, d) silver. For hybrid particles with a gold core, experiments [323] were carried out with the following J-aggregates of dyes: TC (red dashed curves, B), PIC (blue short-dashed curves, C), and Thia(Et) (green dashed-dotted curves, D). In experiments [88] with composite nanospheres with a silver core, J-aggregates of dyes TC (red dashed curves, B) and OS (gray dashed-dotted curves, C) were used. Panels (a) and (c) show light absorption spectra of uncoated Au/TMA and Ag/TMA nanospheres, respectively (solid black curves, A). Geometric parameters of particles with a gold core are as follows: $D = 5.2$ nm is core diameter, $\ell_{\rm s} = 1.1$ nm is TMA spacer thickness, and $l_{\rm J} = 1.7$ nm is J-aggregate layer thickness. Corresponding parameters for particles with a silver core are as follows: $D = 14.1$ nm, $\ell_{\rm s} = 1$ nm and $l_{\rm J} = 4$ nm. Photoluminescence excitation wavelengths are $\lambda = 430$ nm for Au/TMA/TC, $\lambda = 520$ nm for Au/TMA/PIC, $\lambda = 550$ nm for Au/TMA/Thia(Et), $\lambda = 380$ nm for Ag/TMA/TC, and $\lambda = 405$ nm for Ag/TMA/OC.

Au/TMA/Thia(Et) nanoparticles (see the structural formulas of the dyes in Table 2) with a gold core of a spherical [323] and rod-like [330] shape, as well as three-layer Ag/TMA/TC and Ag/TMA/OC nanospheres with a silver core [88].

7.2 Effect of thickness of spacer layer on optical spectra

For a number of problems in the optics and spectroscopy of nanoparticles with a metal core and a double shell, which consists of passive organic spacer and an active J-aggregate outer layer, what stands out is that changing the spacer layer thickness provides an additional opportunity to alter the magnitude and nature of the coupling between the plasmonic core and the outer excitonic shell. This offers some new opportunities for modifying the spectral characteristics of the hybrid nanosystem in comparison with the case of two-layer metal/J-aggregate particles. This was demonstrated in [116] using the example of spherical Ag/TMA/TC nanoparticles with a silver core, an outer J-aggregate shell of the TC cyanine dye, and an organic spacer layer of TMA (N,N,N-trimethyl(11-mercaptoundecyl)ammonium chloride). Similar calculations of the light absorption spectra were carried out in [119] for the composite Au/TMA/J-aggregate nanospheres with a gold core.

To demonstrate the near-field nature of the plexcitonic coupling and the strong dependence of the results on the distance between the plasmonic and excitonic subsystems, we

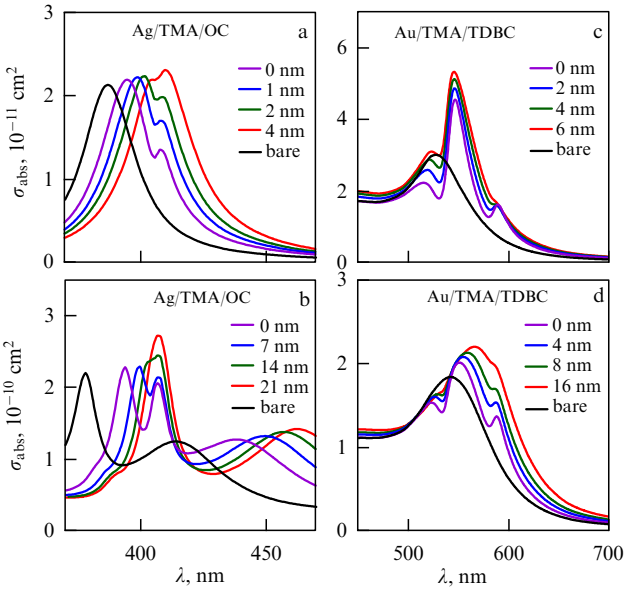

Figure 18. Light absorption cross sections σ_{abs} by (a, b) three-layer Ag/TMA/OC and (c, d) Au/TMA/TDBC nanospheres in an aqueous medium as functions of wavelength of light (λ) in vacuum at different values of thickness ℓ_s of dielectric spacer layer. Calculations were performed within framework of modified Mie theory using the following values of metal core radius r_1, thickness of outer J-aggregate shell l_J, and sets of ℓ_s quantities: (a) $r_1 = 10$ nm, $l_J = 1$ nm, $\ell_s = 0, 1, 2, 4$ nm; (b) $r_1 = 70$ nm, $l_J = 7$ nm, $\ell_s = 0, 7, 14, 21$ nm; (c) $r_1 = 20$ nm, $l_J = 1$ nm, $\ell_s = 0, 2, 4, 6$ nm; and (d) $r_1 = 40$ nm, $l_J = 1$ nm, $\ell_s = 0, 4, 8, 16$ nm. Correspondence of colored spectral curves to certain values of spacer layer thickness ℓ_s is shown in panels. Black curves demonstrate absorption spectra of light by uncoated metal cores.

calculated the light absorption cross sections of three-layer Ag/TMA/OC (Figs 18a and b) and Au/TMA/TDBC (Figs 18c and d) nanospheres. These series of calculations were performed using the extended Mie theory for concentric spheres for four different values of the thickness (ℓ_s) of the spacer layer at different values of the radii (r_1) of the metal core and the thicknesses (l_J) of the outer J-aggregate shell.

Both series of calculations demonstrate strong dependences of the results for the absorption cross sections on the distance ℓ_s between the two interacting active plasmonic and excitonic subsystems. In particular, Fig. 18a shows that, in the case of the silver core, the efficiency of the near-field plexcitonic coupling substantially decreases with increasing ℓ_s. This is manifested as a decrease in the depth of the dip in the vicinity of wavelengths $\lambda = 406$ nm with an increase in the value of ℓ_s. A weakening of the plexcitonic coupling with increasing thickness of the passive spacer also occurs for composite nanospheres of a larger size, as can be seen from Fig. 18b for a core radius of $r_1 = 70$ nm. With such geometric parameters of the particle, the splitting of the spectral peaks near the wavelengths $\lambda = 394$ and 407 nm is pronounced in the absence of a spacer layer at $\ell_s = 0$ nm. However, the splitting is significantly reduced in the presence of a passive spacer with thicknesses $\ell_s = 7$ and 14 nm, and completely disappears at $\ell_s = 21$ nm. One should also pay attention to the distinctions in the overall behavior of the absorption spectra shown in Figs 18a and b for some different particle sizes. This is to be expected, since an increase in the size of a plexcitonic particle significantly changes its effective polarizability, and essentially enhances the contribution to the cross section of the quadrupole and octupole plexcitonic resonances.

The general trend of the plexcitonic coupling, consisting in the rapid fall of its efficiency with increasing distance between the plasmonic and excitonic subsystems of a composite particle, also holds true for three-layer nanospheres with a gold core, a passive spacer layer, and an outer J-aggregate shell. This is clearly demonstrated in Figs 18c and d for particles with a J-aggregate of the TDBC dye in the outer layer. As the thickness of the organic TMA spacer (ℓ_s) increases, the spectral dips located at wavelengths $\lambda = 530$ nm and 580 nm gradually diminish, while the dips near $\lambda = 580$ nm practically vanish. Evidently, the behavior of the spectral curves in Figs 18c and d differs substantially from the case shown in Figs 18a and b for the Ag/TMA/OC metalorganic system. This stems from the considerable difference in the dielectric properties of the Ag and Au metal cores and the J-aggregates of the dyes OC and TDBC, so that the plexcitonic resonances appear for the Ag/TMA/OC and Au/TMA/TDBC systems in different parts of the visible spectrum.

Note also that, in this section, we performed all the calculations using the standard isotropic model (20) for describing the permittivity of molecular aggregates of dyes. Taking into account the effects of the anisotropy of the outer excitonic shell of a three-layer metalorganic nanoparticle in each specific case can change the spectral behavior of the absorption cross section for given values of the geometric parameters of the particle. Nevertheless, the outlined general trend, where the near-field coupling diminishes when the excitonic and plasmonic subsystems are spatially separated, certainly holds.

8. Plexcitonic coupling effects in nanorods and nanoplatelets and their dimers

8.1 Spectral behavior of plexcitonic nanorods with varying their length and number of spacer layers

Due to the presence of longitudinal and transverse plasmon resonances in the case of elongated metal nanoparticles, the spectra of hybrid metalorganic nanorods have their own distinct features compared to the case of plexcitonic nanospheres. In general, both transverse and longitudinal plasmon-polaritons can participate in the near-field coupling with the Frenkel exciton. However, since the positions of the maxima of the longitudinal and transverse resonances are largely determined by the ratio of the longitudinal and transverse sizes of the rod ($L_\parallel/L_\perp$) and can be very significantly moved apart relative to each other on the frequency (or wavelength) scale, the exciton and plasmon with the closest values of the resonance energies experience the strongest interaction with each other. Accordingly, in the case of an exact resonance ($\omega_{pl}^{\parallel} = \omega_{ex}$ and $\omega_{pl}^{\perp} = \omega_{ex}$), effects of strong coupling between an exciton and one of the plasmon modes (such as induced transparency) can occur in a similar way to how it takes place in the case of the nanospheres considered above. This follows directly from the available experimental data [68, 115, 125, 133, 134, 153, 315, 330] and FDTD calculations [68, 94].

Figure 19 shows the results of calculating the extinction spectra of an Ag/TC nanorod. Upon increasing its length L, the field modes excited by incident radiation polarized along the axis of the nanorod pass from the weak plexcitonic coupling regime to the strong coupling regime. The modes excited by external radiation polarized perpendicular to the

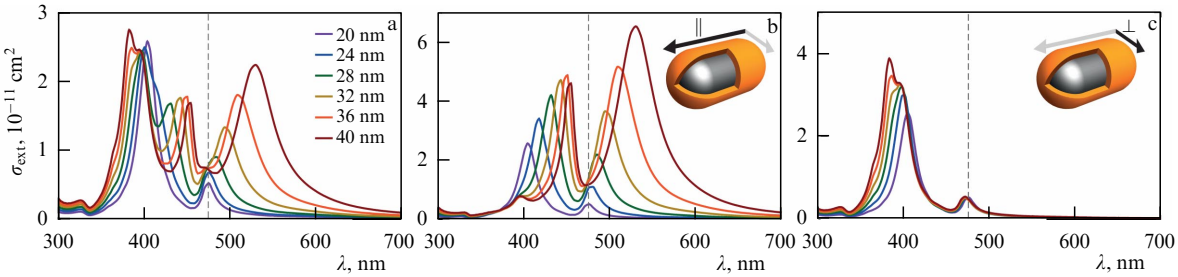

Figure 19. Extinction cross sections of Ag/TC nanorods with round ends in an aqueous solution as functions of wavelength of light in vacuum. Length of silver core was varied in range from $L = 20$ nm to 40 nm with step of 4 nm as shown in inset of Fig. 19a, core diameter is $D = 20$ nm, and thickness of J-aggregate shell is $l_J = 1$ nm. (a) Extinction cross sections of rod averaged over its possible orientations. Panels (b) and (c) show extinction cross sections of light polarized (b) parallel to the axis of rod and (c) perpendicular to this axis. At $L = 20$ nm, rod transforms into a spherical particle. Dashed vertical line shows position of TC J-aggregate peak.

nanorod axis are in the weak coupling regime in all the cases considered here. A characteristic feature of such spectra is that, with a change in the ratio of the length of the rod to its diameter ($L_\parallel/L_\perp$), the positions of the maxima of the plexcitonic resonances corresponding to the longitudinal and transverse modes shift in significantly different ways (Figs 19b and c). With an increase in the ratio $L_\parallel/L_\perp$, the peaks of the plexcitonic resonances for the longitudinal mode shift toward the long-wavelength region of the spectrum, and for the transverse mode, this shift is directed toward short wavelengths. In this case, the plexcitonic peaks for the longitudinal mode are subject to a more significant shift than are the peaks corresponding to the transverse mode. As can be seen from Figs 19b and c, the magnitudes of the maxima of these peaks also change differently. These features are directly reflected in the spectral behavior of the extinction cross sections averaged over the orientations of the rod in space.

Using hybrid nanorods as an example, we will demonstrate another important characteristic feature of plexcitonic coupling, namely, a significant dependence of its efficiency on the number of dielectric spacer layers between the plasmonic component (the rod core) and its outer excitonic shell. Yoshida et al. [330] synthesized multilayer Au/TMA/(PSS/PDDA)$_n$/Thia(Ph) nanorods with a spacer consisting of a monolayer of TMA (N,N,N-trimethyl(11-mercaptoundecyl)ammonium chloride) precipitate and several layers of PSS/PDDA polyelectrolyte ($n = 0$, 1, 2). Figure 20 shows the behavior of the spectra with an increase in the number n of spacer layers of the PSS/PDDA polyelectrolyte; namely, a decrease in the depth of the dip in the spectrum in the vicinity of the resonance ($\lambda \approx 680$ nm) clearly demonstrates a weakening of the efficiency of the near-field coupling between the plasmon localized in the core and the Frenkel exciton in the outer shell.

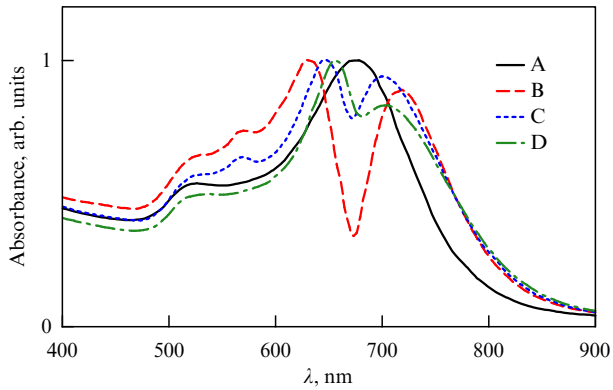

Figure 20. Absorption spectrum [330] of a colloidal solution containing multilayer Au/TMA/(PSS/PDDA)$_n$/Thia(Ph) nanorods with an external J-aggregate shell of Thia(Ph) dye (see the structural formula in Table 2). Black solid curve (A) is a two-layer Au/TMA particle. Colored curves correspond to multilayer particles with different numbers of PSS/PDDA polyelectrolyte spacer layers: $n = 0$ (red dashed curve B), $n = 1$ (blue short-dashed curve C), and $n = 2$ (green dashed-dotted curve D).

8.2 Manifestation of optical chirality in extinction and circular dichroism spectra

In recent years, a series of papers has been published examining the effects of optical chirality in metalorganic nanostructures. These studies have been largely motivated by the great practical interest on the part of medicine and pharmaceuticals in the effects of interaction of light with so-called enantiomers, i.e., isomers that are mirror-symmetric with respect to each other. The great applied significance of such isomers is determined by the fact that they perform different functions and have significantly different biological activity. Optical detection and separation of enantiomers, as well as control of photochemical reactions involving them, are topical problems of modern nanophotonics (see [331] and references therein). On the other hand, in most of the existing papers on plexcitonic nanoparticles, their chiral properties have not been discussed at all, and studies of the fundamental features of plexcitonic coupling in chiral composite particles have only intensified in the last few years.

Notably, a series of experimental studies has been carried out recently (see, for example, [315, 332–335]) in which the effects of plexcitonic coupling in chiral metal/J-aggregate nanoparticles were studied. It should be noted that chirality of a metalorganic nanosystem can stem from fundamentally different factors, for example, (i) chirality of the plasmonic core [335], (ii) chirality of aggregates in the organic shell [315], and (iii) chiral geometry of a complex consisting of several achiral particles [332]. Whenever a chiral molecular aggregate is located near the surface of a metal nanostructure, the near-field plasmon-exciton interaction leads to the emergence of circular dichroism in the vicinity of the plasmon resonance frequency, even if the metal nanostructure itself is achiral. The use of this plexcitonic phenomenon makes it possible to endow achiral plasmonic nanostructures with optical activity.

In this context, Wu et al. [315] recently studied the circular dichroism and light extinction spectra of Au/Ag composite nanocuboids coated with chiral J-aggregates of the TDBC dye, the monomers of which do not exhibit optical activity (Figs 21a and b). The position of the plasmon resonance of the two-component metal core of the Au/Ag nanocuboid was controlled by changing the thickness of the silver shell of the

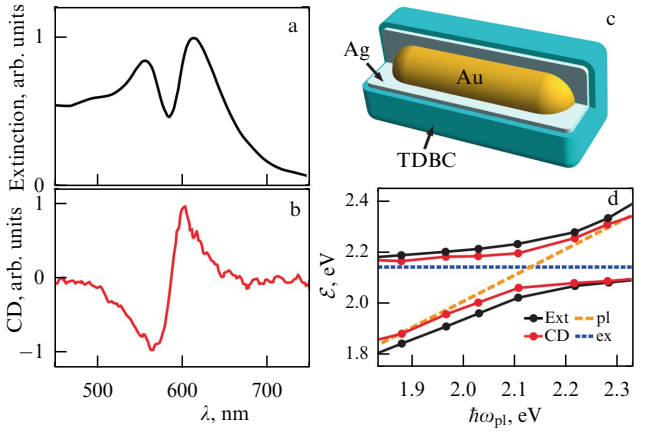

Figure 21. (a) Extinction and (b) circular dichroism spectra of an Au/Ag nanocuboid coated with a chiral J-aggregate of TDBC dye [315]. (c) Schematic view of the particle. (d) Energies of hybrid modes of composite nanoparticle (black and red dots connected by solid curves) as functions of spectral position ($\hbar\omega_{\text{pl}}$) of plasmon resonance of Au/Ag core (orange dashed line). Blue dashed line shows energy of maximum of J-band of TDBC dye, $\hbar\omega_{\text{ex}}$.

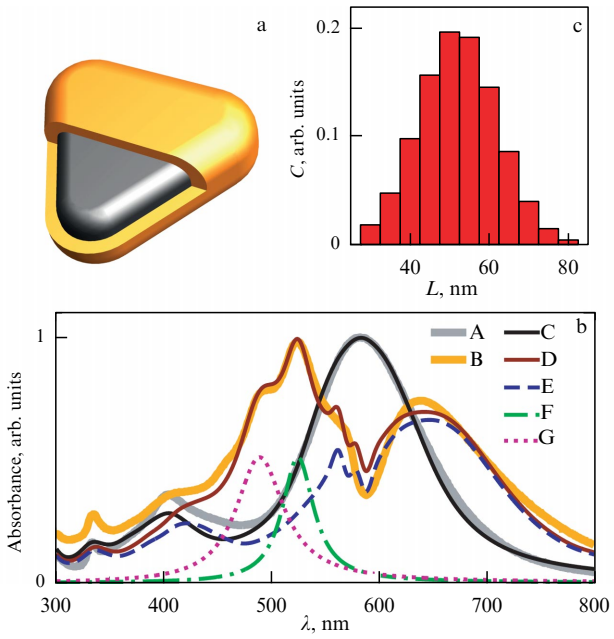

Figure 22. (a) Schematic view of a two-layer metalorganic nanoprism. (b) Experimental data [92] and results of FDTD calculations of absorption spectra of bare silver nanoprisms and two-layer Ag/PIC nanoprisms. Thick gray (A) and orange (B) curves are experimental data for spectra of bare and coated nanoprisms. Black (C) and wine (D) curves are calculation results for bare and coated nanoprisms. Wine curve is obtained taking into account absorption contributions of PIC dye monomer and dimer, as well as the spread of nanoprisms by size. Blue dashed line (E) is calculation of absorption by two-layer nanoprisms. Green dashed-dotted line (F) and pink dotted line (G) are absorption contributions of the monomer and dimer. (c) Histogram of distribution of concentrations (C) of nanoprisms on length of their side, L.

gold rod (Fig. 21c). This allowed the authors of Ref. [315] to experimentally determine the dependence of the energy of hybrid plexcitonic modes on the magnitude of the spectral detuning of the resonances of the isolated metal and J-aggregate subsystems. The dependences obtained in [315] are shown in Fig. 21d. The formation of hybrid modes was confirmed by measuring the positions of peak maxima not only in the extinction spectra but also in the circular dichroism spectra. This indicates that the circular dichroism of the hybrid particle was caused not simply by an increase in the intensity of the dichroic response of the chiral TDBC J-aggregate due to a local field enhancement, but by the formation of new hybrid states in the strong coupling regime. The observed splitting energy of the plexcitonic peaks at the quasi-intersection point differed for the extinction and circular dichroism spectra and amounted, according to the data in [315], to $\Delta\mathcal{E} = 214$ meV and $\Delta\mathcal{E} = 136$ meV, respectively. This difference in the spectral profiles of the two types (Figs 21a and b) was explained in [315] within the framework of the quasistatic approximation. Note that, compared to extinction spectra, circular dichroism spectra contain narrower bands, and the different signs of the signals (positive and negative) of the two hybrid modes ensure their simpler and more reliable experimental measurement.

8.3 Induced transparency of plexcitonic nanoplatelets

The induced transparency effect described in Section 5.2.3 is most prominently manifested in a number of experimental studies on the optical properties of plexcitonic nanoplatelets: nanoprisms and nanodisks. Figure 22 shows experimental data [92] on the light absorption spectra of silver triangular nanoprisms coated with a thick layer ($l_{\text{J}} = 8$ nm) of the PIC dye J-aggregate. The choice of a nanoprism as a core makes it possible to satisfy the resonance condition between the plasmon of the core and the exciton of the J-aggregate shell by varying the length of the prism base edge. A quantitative measure of the efficiency of plexcitonic coupling is the energy splitting between the upper and lower plexcitonic branches determined from the experiment. The magnitude of this splitting, $\hbar\Omega_{\text{R}} = 207$ meV, was determined for such a length of the edge of the prism base that led to a coincidence (resonance) at $\lambda = 582$ nm of a unperturbed energies of the plasmon ($\hbar\omega_{\text{pl}}$) and the exciton ($\hbar\omega_{\text{ex}}$). In the theory of nonadiabatic transitions between the electronic terms of a diatomic molecule, the fulfillment of the resonance condition ($\hbar\omega_{\text{ex}} = \hbar\omega_{\text{pl}}$) corresponds to the intersection point of the diabatic curves of the potential energy. The resulting energy splitting of the hybrid modes of the composite nanoplatelet indicates the presence of a strong plexcitonic coupling regime (see Section 5.4) in the phenomenon of induced transparency.

In the solution prepared in experimental study [92], in addition to J-aggregate-coated silver nanoprisms with a fairly wide range of sizes, there were also monomers and dimers of the dye. Therefore, the resulting absorption spectra recorded in a colloidal solution are defined as a sum $\sigma(\omega) = \sum_j c_j\sigma_j(\omega)$ of the absorption cross sections $\sigma_j(\omega)$ of its individual components j with weighting factors proportional to their concentrations (c_j) in the solution. The absorption cross sections of nanoprisms with sizes varying from $L = 30$ nm to $L = 75$ nm with a step of 5 nm were calculated. The prism height was $h = 10$ nm, and the thickness of the organic shell was $l_{\text{J}} = 8$ nm. The parameters of the J-aggregate of the PIC dye are taken from Table 2.

The effect of induced transparency (i.e., a dip in the absorption spectrum of light) was also observed in [91], where the object demonstrating this phenomenon was a triangular silver nanoprism coated with the J-aggregate of the TDBC dye (Figs 23a–d). In the experiment, the wavelength of the localized plasmon was tunable in the range from 400 to

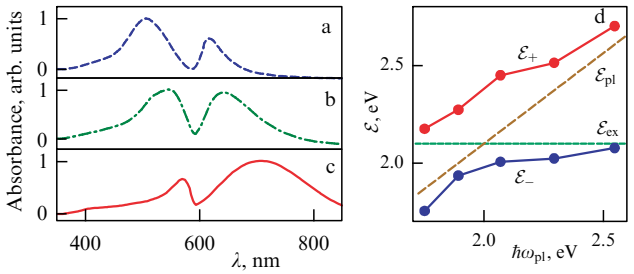

Figure 23. (a)–(c) Absorption spectra of triangular silver nanoprisms coated with J-aggregate of TDBC dye in an aqueous solution [91] at different edge lengths: (a) 60 nm, (b) 100 nm, and (c) 140 nm. (d) Behavior of energy branches $\mathcal{E}_+$ (red curve) and $\mathcal{E}_-$ (blue curve) of Ag/TDBC hybrid modes as functions of energy $\mathcal{E}_{pl} = \hbar\omega_{pl}$ of the plasmon in an uncoated prism (dark yellow line). Green horizontal line is energy $\mathcal{E}_{ex} = \hbar\omega_{ex}$ of the exciton transition in J-band of TDBC dye aggregate.

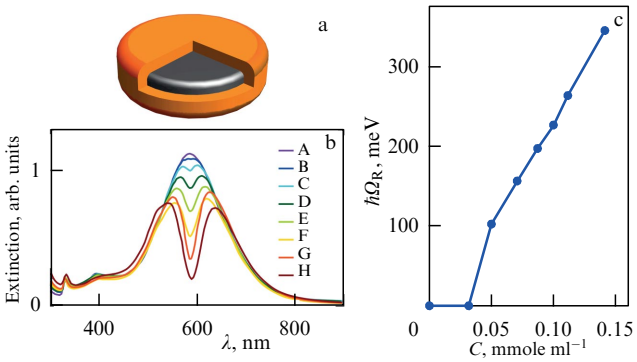

Figure 24. Demonstration of possibility of controlling the energy of plexcitonic coupling in a hybrid Ag/TDBC system by changing the amount of aggregated dye in the outer excitonic layer. (a) Schematic view of a two-layer metalorganic nanodisk. (b) Extinction spectra of plexcitonic nanodisks at different values of dye concentration in a colloidal solution of Ag/TDBC nanoparticles. Order of curves from top to bottom, designated A, B, C, ..., H, corresponds to an increase in the dye concentration. Curve A refers to the case of a silver disk uncoated with an aggregate. (c) Value of energy splitting ($\hbar\Omega_R = 2\hbar g$) of upper and lower states of hybrid system as a function of concentration C of TDBC dye in the solution.

1100 nm. Plotting the energy branches of the $\mathcal{E}_+$ and $\mathcal{E}_-$ hybrid modes of the Ag/TDBC plexcitonic nanoprism based on measurements of the dependence of the positions of the spectral maxima made it possible to determine for this system the characteristic value of the constant ($V = \hbar g$) of the plexcitonic coupling, which, under the conditions of resonance of the plasmonic and excitonic subsystems, corresponds to the splitting energy of the hybrid modes, $\Delta\mathcal{E} = \mathrm{Re}\,\{\mathcal{E}_+ - \mathcal{E}_-\} = \hbar\Omega_R = 2V = 400$ meV (Fig. 23d). This energy amounted to 19% of that of the exciton transition in the J-band of the TDBC aggregate, which, according to the semi-empirical criterion given in Section 5.4, corresponds to the ultrastrong plexcitonic coupling regime. Such a significant value of the coupling energy is the result of strong localization of the electric field near the sharp corners of the nanoprism. A comparison of the results presented in Table 3 on the splitting energies of spectral peaks obtained by different authors in studying the regimes of strong and ultrastrong plexcitonic coupling in metalorganic nanosystems shows that one of the highest values of $\hbar\Omega_R$ was obtained in [91].

Computer simulation of the optical spectra of silver and gold nanoprisms and nanostars coated with dye aggregates having different optical properties (TC, PIC, and TDBC) was performed in [329] in order to study possible regimes of plexcitonic coupling. The calculations were carried out by the FDTD method using the standard isotropic model (20) of the excitonic shell. In this case, typical dips were reproduced in the absorption spectra of the systems studied, which are consistent with the effect of induced transparency.

The phenomenon of induced transparency was also studied in [318] using silver nanodisks coated with a layer of TDBC dye J-aggregate as an example (Fig. 24a). In the experiments, the plexcitonic coupling strength was varied, and a very high value of the splitting energy of hybrid modes was achieved, $\hbar\Omega_R > 350$ meV, indicating a transition to the limit of ultrastrong plexcitonic coupling. The disk diameter was selected in such a way that the plasmon and exciton resonance frequencies coincided ($\lambda_{ex}^{TDBC} = 585$ nm). The formation of plexcitonic nanoparticles manifested itself in a pronounced dip in their extinction spectra.

The experimental data [318] on the extinction spectra are shown in Fig. 24b for different values of dye concentration. The authors manipulated the amount of aggregated dye molecules attached to silver nanodisks by controlling the concentration of dye molecules in the colloidal solution. Figure 24b shows that varying the concentration significantly affects the depth of the dip in the extinction spectrum of Ag/TDBC nanodisks and causes a transition from the weak coupling regime (at low concentrations) to the strong and then ultrastrong coupling regimes (at high concentrations). The experimental results shown in Fig. 24c show an increase in the Rabi splitting energy with increasing dye concentration after reaching the strong coupling regime. The above is consistent with the theory presented in Section 5.2. The main result of [318] was, therefore, the demonstration of the possibility of effectively controlling the process of the formation of the J-aggregate layer on the nanodisk surface and the magnitude of the plexcitonic coupling energy and, accordingly, the extinction and transmission spectra of hybrid nanoplatelets.

8.4 Replication of spectral bands of plexcitonic nanoparticle dimers

An unusual manifestation of the strong plasmon-exciton coupling regime is the effect of spectral band replication, which qualitatively differs in its physical nature from the previously discovered plexcitonic effects. As was shown in [297, 299], the spectra of pairs of closely spaced and partially merging two-layer metalorganic nanoparticles contain a double number of plexcitonic spectral bands, compared to cases where the dimer particle has no organic shell. These plexcitonic bands can be divided into two groups: 'original' $\mathbf{o}_i$ bands, which exactly reproduce the plasmon peaks ($\mathbf{p}_i$), and their 'replicas' ($\mathbf{r}_i$) with a specific mutual arrangement and distribution of intensity. Figure 25 explains the essence of the phenomenon using the example of the light absorption spectra of pairs of two-layer Ag/TDBC nanoparticles of spherical (Figs 25c and d) and disk-like (Fig. 25e) shapes.

The positions of the $\mathbf{o}_i$ bands in the spectra of two-layer dimers are close to those of the $\mathbf{p}_i$ bands of plasmon dimers. There are also narrow spectral peaks $\mathbf{s}_i$, which should be attributed to exciton resonances in the J-aggregate shell. It is important to note that the spectra of plexcitonic dimers also

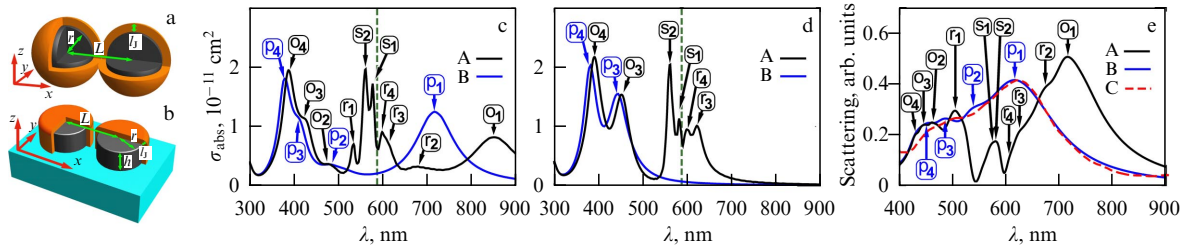

Figure 25. Demonstration of spectral band replication effect using plexcitonic dimers consisting of a pair of nanoparticles with a silver core coated with a J-aggregate of TDBC dye as an example. Panels (a) and (b) show schematic images of dimers under study, consisting of (a) two hybrid nanospheres and (b) two hybrid nanodisks on a glass substrate. Panels (c)–(d) show results of calculations [299] of optical spectra of plexcitonic dimers in an aqueous solution (black curve, A) and their comparison with corresponding results for uncoated silver dimers (blue curve, B). Panels (c) and (d) show light absorption spectra by Ag/TDBC nanospheres for two values of the distance between their centers: (c) $L = 18$ nm and (d) $L = 22$ nm. In both calculations, the radius of silver cores and shell thickness were $r = 10$ nm and $l_J = 3$ nm. Panel (e) shows dark-field spectra for Ag/TDBC nanodisks; red dashed line (C) shows experimental data [336] for bare silver disks. Radius and height of silver disks $r = 40$ nm and $h = 40$ nm; distance between their centers $L = 110$ nm, and shell thickness $l_J = 12$ nm. Vertical green dashed line indicates position of J-band center. Arrows indicate $\mathbf{p}_i$, 'plasmon' peaks of the uncoated dimer; $\mathbf{o}_i$ and $\mathbf{r}_i$, plexcitonic peaks associated with 'original' and 'replication' bands of the dimer; and $\mathbf{s}_i$, resonances of J-aggregate shell of the dimer.

contain an additional group of bands, $\mathbf{r}_i$ (Figs 25c and d). These bands are always located on the other side of the $\mathbf{o}_i$ bands relative to the exciton resonance of the J-aggregate of the dye. The mutual arrangement, relative widths, and intensities of the plasmon $\mathbf{p}_i$ bands are reproduced quite accurately by the $\mathbf{o}_i$ bands and are reflected with some distortions by the $\mathbf{r}_i$ bands on the other side of the exciton resonance. This becomes especially noticeable if we trace the changes in the position of the $\mathbf{o}_i$ and $\mathbf{r}_i$ spectral bands that arise when the distance between the particles in the hybrid dimer is varied and compare these changes with the corresponding shifts of the $\mathbf{p}_i$ bands of the uncoated metal dimer. The above-described properties in optical spectrum plexcitonic dimers composed of two hybrid metalorganic Ag/TDBC nanospheres and 'core–shell' nanodisks were established in [299] using FDTD numerical simulations. A qualitative and quantitative explanation of the phenomenon of spectral band replication was also given using the effective multilevel Hamiltonian model (see Section 5.3.3). This Hamiltonian took into account the terms responsible for the interaction of quasi-degenerate exciton modes of the organic shell with multiple modes of the plasmon dimer composed of two uncoated metal nanospheres or nanodisks (for more details, see [299]).

Note also that the relationship between the occurrence of the replication phenomenon and achieving the strong plasmon-exciton interaction regime was studied in [298] by analyzing the change in the spectra of metalorganic nanoparticle dimers upon the introduction of a passive dielectric spacer layer between their cores and shells. As the thickness of this spacer layer increases, the 'replicas' of the plasmon resonances approach the position of the J-aggregate band and disappear. This confirms the validity of the classification of spectral bands in terms of plexcitonic 'originals' and 'replicas' of plasmon resonances. A peculiar feature of the spectral band replication effect is that it is observed in situations where the J-band of the molecular aggregate lies at some distance relative to the plasmon resonance peak toward the long-wavelength side. This distinguishes it from traditional dip effects in the absorption spectra of hybrid metalorganic nanoparticles, which appear under the condition of proximity or coincidence of the resonance frequencies of the plasmonic and excitonic subsystems.

9. Effects of anisotropy of excitonic shell and their influence on light absorption and scattering spectra

9.1 Optical anisotropy of molecular J-aggregates

Absorption and scattering spectra of light, as well as analysis of the plasmon-exciton interaction regimes in hybrid metal/J-aggregate and metal/spacer/J-aggregate nanostructures, were previously theoretically described in almost all cases within the framework of various isotropic models. In isotropic models, the outer layer of the organic dye is usually considered an isotropic medium with an effective scalar local resonance dielectric function (20). In many cases, such theoretical approaches make it possible to describe the optical spectra of plexcitonic nanosystems and adequately interpret a particular regime of plasmon-exciton coupling. However, isotropic approaches are inapplicable to the analysis of cases where the outer organic shell of the system has pronounced anisotropic dielectric properties.

It is well known that nano- and micrometer-sized structures consisting of large extended molecules are usually anisotropic. A striking example of dyes capable of forming molecular J-aggregates with pronounced anisotropic dielectric properties is pseudoisocyanine dye (PIC). The synthesis of molecular aggregates of this and other dyes, as well as the study of their morphology, have been the subject of intensive research for many years [337–341]. In particular, in order to clarify the arrangement and direction of the molecules constituting the aggregate, the linear dichroism of a film of highly oriented J-aggregate of pseudoisocyanine bromide was studied in [338]. The anisotropic effects in the absorption and fluorescence spectra of fibril-shaped J-aggregates of pseudoisocyanine dyes in thin-film matrices was observed in [339]. Experimental results for oriented J-aggregates of the PIC dye demonstrated a significant difference between the absorption spectra obtained for light polarizations parallel and perpendicular to the orientation axis of the J-aggregate. Pronounced anisotropic absorption has also been demonstrated for J-aggregates of a number of carbocyanine dyes [195, 342]. It has been shown that, when light is polarized parallel to the direction of alignment of these molecular aggregates, intense narrow bands appear in their absorption spectra.

Anisotropy effects in the processes of absorption and scattering of light by various nanoparticles have been actively studied for many years. This is owing to the important role the effects play in some technological and biological applications [343]. A modification of the Mie theory for describing the scattering and extinction spectra of spherical nanoparticles coated with an optically anisotropic outer shell was proposed in [344]. Within the framework of the quasistatic approximation, an analytical description of the optical spectra of ellipsoidal plasmon particles coated with an anisotropic shell was developed in [272]. Orientational effects in dipole–dipole interactions between neighboring dye molecules have recently been considered using the coupled dipole model in a spherical metalorganic core–shell systems [345]. In this work, the influence of the dye molecule concentration in the shell and the coating uniformity on the process of light scattering was also studied theoretically. A thin-shell approximation of the Mie scattering problem for spherical 'core–shell' and 'core–double–shell' structures with radial anisotropy in the outer layer was proposed in [346, 347]. This approximation describes some orientational and anisotropic effects arising from the resonant dye–plasmon interaction. In addition, the authors of Refs [348, 349] developed a model to estimate the effective dielectric function of the anisotropic layer of dye molecules adsorbed on a metal surface and to describe the electromagnetic core–shell interaction in such systems. The role of orientational effects of the molecular self-assembly of a J-aggregate excitonic shell in the formation of optical spectra of some plexcitonic 'core–shell' and 'core–double–shell' nanoparticles of various sizes, shapes, and compositions is clarified in [251, 252].

9.2 Features of spectra of plexcitonic systems with isotropic and anisotropic outer shells

Let us discuss the role of the anisotropy of the outer shell of ordered molecular J-aggregates in the formation of the plexcitonic coupling and optical spectra of metalorganic nanoparticles. The authors of Refs [251, 252] studied theoretically the effects of plasmon-exciton interaction and the behavior of the absorption and scattering spectra of light by hybrid nanoparticles of various shapes, containing a metal core and an outer shell of molecular J-aggregates of organic dyes. In [251], it was shown that taking into account the anisotropy of the J-aggregate shell of the composite system makes it possible to consistently explain the available experimental data on the optical spectra of a number of studied metalorganic nanoparticles, which cannot be correctly described within the framework of the standard isotropic model of the outer J-aggregate shell (see formula (20)).

This fact is illustrated by Figs 26a and b, which show the optical spectra of hybrid three-layer Au/MUA/PIC and Au/TMA/PIC nanoparticles with gold cores and the same molecular aggregate of the PIC dye, but with different passive dielectric spacer layers of MUA and TMA. The anisotropy effect manifests itself in the qualitatively different shape of these spectra for the cases of normal and tangential orientation of the aggregated molecules in the dye shell relative to the surface of the nanostructure. It was shown that the results of theoretical calculations are in good agreement with the available experimental data only when the optical anisotropy of the shell is taken into account, and when there is only one clearly pronounced spatial orientation of the aggregate. Agreement is achieved for (Fig. 26a) Au/MUA/PIC and (Fig. 26b) Au/TMA/PIC nanoparticles if the PIC aggregates are oriented along the normal to the surface and along the surface, respectively. It is worth noting here that, according to the results of experimental studies [322, 323, 330], the use of a number of optically passive organic substances (for example, TMA or MUA) as dielectric spacers promotes the aggregation of dye molecules on the surface of nanoparticles.

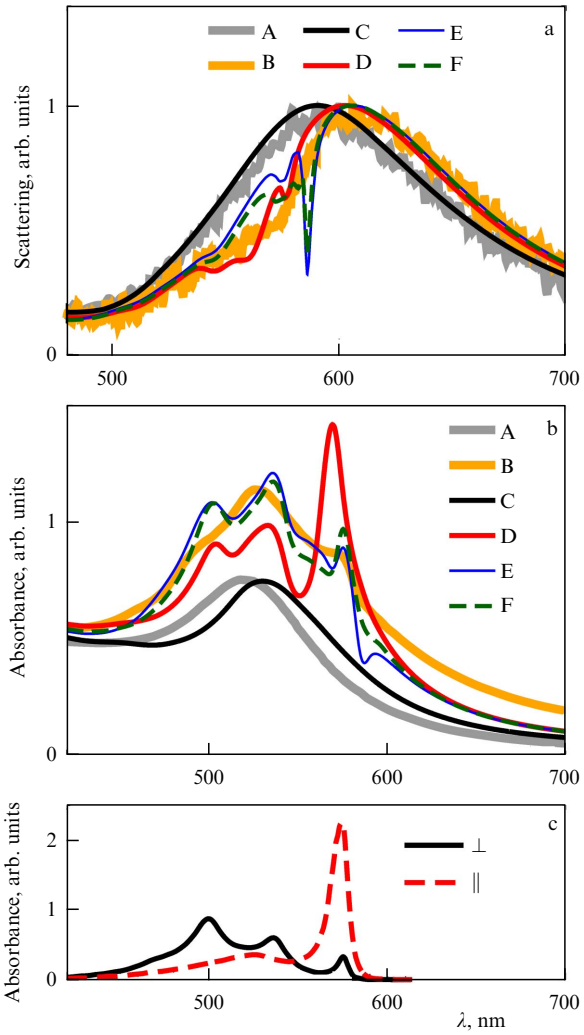

Figure 26. (a) Comparison of experimental [322] and theoretical [251] data on scattering spectra of two-layer Au/MUA and three-layer Au/MUA/PIC nanospheres with a diameter of 100 nm. Thick gray (A) and orange (B) curves are experimental data for two- and three-layer particles. Black curve (C) shows calculation results for two-layer particles; red (D), thin blue (E) curves and green dashed line (F) show calculation results for three-layer particles. Calculations were performed for the PIC dye J-aggregate in the outer shell oriented normally (D) and tangentially (E) to surface, and also using isotropic (F) dielectric function (20). (b) Comparison of experimental [323] and theoretical [251] data on absorption spectra of two-layer Au/TMA and three-layer Au/TMA/PIC nanospheres with a diameter of 9.1 nm. Designations of curves are the same as in panel (a). (c) Absorption spectra of J-aggregate of PIC dye with polarization of incident light parallel (dashed red curve) and perpendicular (solid black curve) to aggregate axis [338].

A comparison of the results for Au/MUA/PIC and Au/TMA/PIC nanoparticles, which have completely different spacer layers of MUA and TMA, indicates a strong dependence of the orientation of the molecular aggregate of the hybrid nanoparticle on the surface material on which the

aggregate is assembled. This conclusion is consistent with modern concepts in chemistry that metal nanoparticles coated with MUA and TMA form oppositely charged particles [350, 351]. Thus, it is possible to effectively control the optical properties of hybrid metalorganic nanostructures by selecting the proper optically passive spacer layer between the plasmonic core and the outer excitonic shell. Therefore, the effect of the passive dielectric spacer layer on the resulting spectra of the hybrid system does not stem solely from specific values of its permittivity ε_s and thickness ℓ_s. Along with these factors, the physicochemical properties of the passive spacer material have a strong influence on the optical spectra, since they determine the orientation of molecular aggregates during the formation of the outer J-aggregate shell.

Note that the use of the isotropic scalar dielectric function (20) of the outer organic shell in the calculations can provide a reasonable explanation for some of the available experimental data. Analysis shows that, if the effective oscillator strength of the exciton transition in the J-band of the molecular aggregate is small enough, the optical spectra of metalorganic nanoparticles with tangential orientation of the J-aggregate in the outer shell of the dye are quite close to the spectra of hybrid nanoparticles with an optically isotropic shell. In this case, the behavior of these spectra will differ significantly from the calculated spectra of the same hybrid nanoparticles, but with a normal orientation of the J-aggregate in the excitonic shell.

The nature of the differences in the spectra of metalorganic nanoparticles with isotropic and anisotropic shells in the strong and ultrastrong plexcitonic coupling regimes was studied in [252]. It was shown that the use of the isotropic permittivity of the J-aggregate can lead to significant discrepancies between the theoretical predictions and experimental spectra of hybrid nanoparticles. This discrepancy is especially noticeable in the case of metalorganic structures with a shell made of the J-aggregate of the TDBC dye, since the value of the effective oscillator strength of its exciton band is quite large ($f \sim 0.22$). The energy of the plexcitonic coupling (Rabi splitting) in such a system reaches hundreds of meV. In this case, calculations performed using the isotropic model (20) for the dielectric function ε_J predict a third resonance between two polariton bands [67, 89] (Figs 27a and d). However, this resonance was observed experimentally only in cases of large thicknesses of J-aggregate layers ($\gtrsim 10$ nm) (see, for example, [87]). At these thicknesses of the organic excitonic shell, a significant part of it is located at a sufficiently large distance from the metal surface; accordingly, this part of the shell does not enter into strong coupling with the plasmonic core of the particle. In such a situation, the anisotropy effects observed in the optical spectra in the strong plexcitonic coupling regime are hardly manifested. In experiments with nanoparticles coated with an organic shell having a thickness of several nanometers, such resonance was not observed (see the discussion in [352]), despite the predictions by the isotropic model.

The calculation results presented in Figs 27a–i show that the use of isotropic permittivity (20) for describing the outer excitonic shell of the metalorganic nanoparticle leads to the appearance of an additional band near $\lambda = 490$ nm in the spectrum. The intensity of this band increases with increasing effective oscillator strength f_J. However, in the spectra obtained using the tensor model of the anisotropic shell, this band is absent for both (tangential and normal) orientations of the J-aggregates in the organic shell. Figure 27j demonstrates that the assumption of the tangential orientation of the J-aggregates of the TDBC dye in the outer shell allows one to reach good agreement between theoretical [252] and experimental [352] data. At the same time, the use of isotropic permittivity does not make it possible to achieve satisfactory agreement with the experiment.

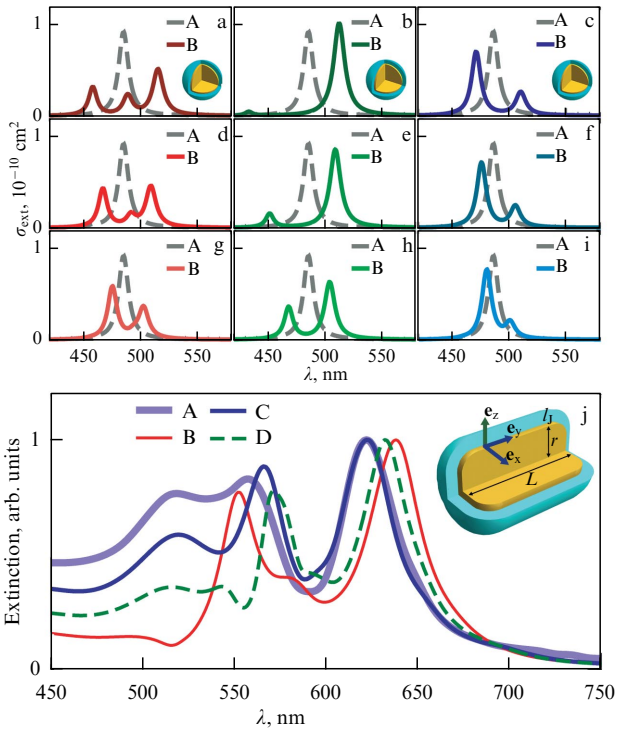

Figure 27. (a–i) Extinction spectra of a two-layer nanosphere with a gold core and a J-aggregate shell at different values of effective oscillator strength f_J and different orientations of J-aggregate relative to the metal surface [252]. (a–c) Results of calculations at $f_J = 0.15$ using (a) isotropic dielectric function and (b) normal and (c) tangential orientation of J-aggregates in the dye shell. (d–i) Similar calculations for $f_J = 0.08$ and $f_J = 0.03$. Gray dashed curve (A) shows calculations for an uncoated particle. Colored solid curves (B) show results for two-layer particles with a core diameter $D = 25$ nm and a shell thickness $l_J = 3$ nm. Dielectric function of the metal is described by Drude formula with parameters corresponding to plasmon resonance of gold [352]. Parameters of model J-aggregate are as follows: $\varepsilon_J^\infty = 1.7$, $\omega_{ex} = 2.5$ eV, and $\gamma_{ex} = 0.05$ eV. (j) Extinction spectra of a gold nanorod coated with TDBC. Thick lavender curve (A) shows experimental results [352]. Thin red (B) and blue (C) curves and green dashed line (D) are results of calculations [252]. Calculations were performed for different orientations of J-aggregate in the outer shell: normal (B) and tangential (C) to the surface, as well as using the isotropic (D) dielectric function (20). Radius of nanorod $r = 9.8$ nm, length $L = 32$ nm, and thickness of dye shell $l_J = 3$ nm.

10. Conclusions

The review provides insight into physical phenomena of light interaction with hybrid nanostructures due to the near-field coupling between Frenkel excitons in the outer organic shell and surface plasmon-polaritons localized in their metal core. This rapidly emerging research field extends some general ideas in subwavelength optics, plasmonics, and organic photonics. We have briefly discussed key properties of dipole and multipole localized plasmon-polaritons in metal nanoparticles and molecular excitons in ordered aggregates of dyes, which are necessary for understanding the effects of plexcitonic coupling and the main features in the behavior of

absorption, scattering, and luminescence spectra of the metalorganic nanostructures. We have outlined the basic physical approaches and methods for describing optical phenomena arising upon interaction of light with such structures. Furthermore, we have formulated some simple models for interpreting various plexcitonic coupling regimes, including weak, strong, and ultrastrong coupling. In addition to the traditionally discussed topics, considerable attention has been paid to the investigation of some novel points in the optics of plexcitonic nanostructures. In particular, we have explored the influence of size effects on the behavior of optical spectra of metalorganic nanosystems; analyzed the role of electric dipole, quadrupole, and octupole plasmons on the nature of plexcitonic coupling; and studied the role of a passive dielectric organic layer (spacer between the plasmonic core and the excitonic shell) in the formation of nanostructures with qualitatively different optical properties. In addition, we have overviewed a number of available experimental and theoretical results on the light absorption, scattering, and extinction, as well as photoluminescence and circular dichroism of hybrid metalorganic nanoparticles of various compositions, sizes, and geometric shapes (spheres, disks, rods, and prisms).

Importantly, our theoretical analysis of plexcitonic effects is not limited to the presentation of the standard scalar 'isotropic' model of the excitonic shell of a composite nanoparticle, but also covers a new physical approach based on the use of a tensor model for describing molecular aggregates with tangential and normal components of permittivity that differ significantly from each other. Within the framework of this approach, recently we have provided a successful quantitative explanation of the available experimental data on the optical spectra of plexcitonic nanospheres and nanorods, adequately taking into account the anisotropy of the excitonic shell of the system. Among other phenomena studied recently by means of new approaches is the replication of spectral bands of plexcitonic dimers of two-layer nanodisks and nanospheres. The phenomenon has been explained using FDTD numerical calculations and received a clear physical interpretation within the framework of the effective multilevel Hamiltonian model. Another example of a new phenomenon studied recently and discussed in our review is the optical chirality of plexitonic systems, manifested in the circular dichroism and extinction spectra of a metal nanorod coated with a chiral J-aggregate dye.

The experimental and theoretical data presented in the review clearly demonstrate that the choice of the shape, size, and composition of plasmonic and excitonic subsystems can dramatically affect the efficiency and regime of plexcitonic coupling in various hybrid nanosystems. Thus, modern synthesis methods make it possible to fabricate hybrid nanoparticles, multilayer nanostructures, and their arrays with new unique optical properties. As such, metalorganic nanostructures and nanomaterials are considered to be promising subject matter for nanophotonics and molecular optoelectronics. Such nanostructures can be used to develop highly sensitive biological and chemical sensors and photodetectors with high spectral selectivity, efficient converters of light energy in the visible and near-IR ranges, and novel fluorescent materials. Hybrid metalorganic nanostructures seem promising for achieving efficient coherent transfer of near-field interaction in nanophotonic devices. Such plexcitonic structures allow for efficient control and manipulation of light fields on nanometer spatial and ultrashort time scales. They are also of interest for a number of photonic applications due to the enormous values of nonlinear optical susceptibilities of molecular aggregates forming the organic component of hybrid metalorganic nanosystems. In the past few years, the possibility of their use for enhancing the effects of optical chirality has been intensively discussed in applications to the problems of selective detection of chiral organic molecules and their complexes at low concentrations.

In conclusion, we note that the physical approaches and methods for describing plexcitonic phenomena in metalorganic nanosystems have much in common with the consideration of similar effects of coupling between plasmon-polaritons and excitons in inorganic composite materials, for example, in systems containing metal nanoparticles and semiconductor quantum dots, quantum wells, or quantum wires. To a certain extent, this also applies to theoretical models for describing optical effects caused by electromagnetic coupling of excitons with polaritons in microcavities. So, the insights on the optics of metalorganic nanostructures presented in the review are useful for understanding the essence of plexcitonic phenomena in the aforementioned systems.

The study was supported by the Russian Science Foundation (grant no. 19-79-30086). We are very grateful to our colleague Sergey Moritaka for discussing the results and his constructive advice, as well as for great assistance provided to the authors in preparing a number of materials for the review. We are also grateful to Alexander Narits for careful reading of the manuscript and valuable comments.

References

1. Gallop N P et al. *Nat. Mater.* **23** 88 (2024)
2. Perego J et al. *Nat. Commun.* **13** 3504 (2022)
3. Koduru J R, Karri R R, Mubarak N M (Eds) *Hybrid Nanomaterials for Sustainable Applications*: *Case Studies and Applications* (Amsterdam: Elsevier, 2023) https://doi.org/10.1016/C2021-0-01044-0
4. Beddoes B et al. *Opt. Express* **31** 18336 (2023)
5. Xie Y et al. *Polymers* **15** 3721 (2023)
6. Vats G et al. *Adv. Mater.* **35** 2205459 (2023)
7. Youngblood N et al. *Nat. Photon.* **17** 561 (2023)
8. Kim J H et al. *Adv. Mater.* **34** 2104678 (2022)
9. Manzhos S et al. *Adv. Phys. X* **6** 1908848 (2021)
10. Milichko V A et al. *Phys. Usp.* **59** 727 (2016); *Usp. Fiz. Nauk* **186** 801 (2016)
11. Reus M A et al. *Adv. Opt. Mater.* **12** 2301008 (2024)
12. Yang S et al. *J. Lumin.* **270** 120560 (2024)
13. Trapani D et al. *Materials* **15** 5450 (2022)
14. Narayan R (Ed.) *Encyclopedia of Sensors and Biosensors* (Amsterdam: Elsevier, 2022)
15. Firoozi A et al. *Sci. Rep.* **13** 11325 (2023)
16. Ates H C et al. *Nat. Rev. Mater.* **7** 887 (2022)
17. Rodrigues F et al. *Photonics* **10** 182 (2023)
18. Chandrasekar R *Chem. Commun.* **58** 3415 (2022)
19. Davis T J, Gómez D E, Roberts A *Nanophotonics* **6** 543 (2017)
20. Fernandez-Bravo A et al. *Nat. Mater.* **18** 1172 (2019)
21. Wang Z et al. *Laser Photon. Rev.* **11** 1700212 (2017)
22. Balykin V I *Phys. Usp.* **61** 846 (2018); *Usp. Fiz. Nauk* **188** 935 (2018)
23. Park C et al. *Phys. Rev. Lett.* **113** 113901 (2014)
24. Kazantsev D V et al. *Phys. Usp.* **60** 259 (2017); *Usp. Fiz. Nauk* **187** 277 (2017)
25. Khodadadi M, Nozhat N, Moshiri S M M *Opt. Express* **28** 3305 (2020)
26. Agranovich V M, Gartstein Yu N, Litinskaya M *Chem. Rev.* **111** 5179 (2011)
27. Will P-A, Reineke S, in *Handbook of Organic Materials for Electronic and Photonic Devices* (Ed. O Ostroverkhova) (Amsterdam: Elsevier, 2019) p. 695

28. Zhou Y (Ed.) *Optoelectronic Organic-Inorganic Semiconductor Heterojunctions* (Boca Raton, FL: CRC Press, 2021)
29. Klimov V *Nanoplasmonics* (New York: Pan Stanford Publ., 2014); Translated from Russian: *Nanoplazmonika* (Moscow: Fizmatlit, 2009)
30. Chang H et al. "Plasmonic nanoparticles: basics to applications (I)," in *Nanotechnology for Bioapplications* (Advances in Experimental Medicine and Biology, Vol. 1309, Ed. B H Jun) (Singapore: Springer, 2021) p. 133, https://doi.org/10.1007/978-981-33-6158-4_6
31. Lindquist N C et al. *Rep. Prog. Phys.* **75** 036501 (2012)
32. Qazi U Y, Javaid R *Adv. Nanopart.* **5** 27 (2016)
33. Kondorskiy A D, Lebedev V S *J. Russ. Laser Res.* **42** 697 (2021)
34. Tribelsky M I, Miroshnichenko A E *Phys. Usp.* **65** 40 (2022); *Usp. Fiz. Nauk* **192** 45 (2022)
35. Khlebtsov N G, Dykman L A, Khlebtsov B N *Russ. Chem. Rev.* **91** RCR5058 (2022); *Usp. Khim.* **91** RCR5058 (2022)
36. Krasnok A E et al. *Phys. Usp.* **56** 539 (2013); *Usp. Fiz. Nauk* **183** 561 (2013)
37. Lepeshov S I et al. *Phys. Usp.* **61** 1035 (2018); *Usp. Fiz. Nauk* **188** 1137 (2018)
38. Barbillon G (Ed.) *Nanoplasmonics*: *Fundamentals and Applications* (London: IntechOpen, 2017) https://doi.org/10.5772/65150
39. Klimov V V *Phys. Usp.* **64** 990 (2021); *Usp. Fiz. Nauk* **191** 1044 (2021)
40. Diedenhofen S L et al. *Light Sci. Appl.* **4** e234 (2015)
41. Tam F et al. *Nano Lett.* **7** 496 (2007)
42. Liaw J-W et al. *Opt. Express* **17** 13532 (2009)
43. Ming T et al. *J. Phys. Chem. Lett.* **3** 191 (2012)
44. Dong J et al. *Nanophotonics* **4** 472 (2015)
45. Lee H et al. *Nanophotonics* **9** 3089 (2020)
46. Kneipp K et al. *Phys. Rev. Lett.* **78** 1667 (1997)
47. Le Ru E C, Etchegoin P G *Principles of Surface-Enhanced Raman Spectroscopy and Related Plasmonic Effects* (Oxford: Elsevier, 2008) https://doi.org/10.1016/B978-0-444-52779-0.X0001-3
48. Chen S et al. *J. Phys. Chem. C* **119** 5246 (2015)
49. Khlebtsov B N et al. *Phys. Chem. Chem. Phys.* **25** 30903 (2023)
50. Arslanagić S, Ziolkowski R W *Photon. Nanostruct. Fundam. Appl.* **13** 80 (2015)
51. Smirnov B M *Phys. Usp.* **60** 1236 (2017); *Usp. Fiz. Nauk* **187** 1329 (2017)
52. Lee C et al. *Chem. Rev.* **121** 4743 (2021)
53. Shapiro B I *Russ. Chem. Rev.* **75** 433 (2006); *Usp. Khim.* **75** 484 (2006)
54. Würthner F, Kaiser T E, Saha-Möller C R *Angew. Chem. Int. Ed.* **50** 3376 (2011)
55. Kobayashi T (Ed.) *J-Aggregates* Vol. 2 (Singapore: World Scientific, 2012) https://doi.org/10.1142/8226
56. Bricks J L et al. *Methods Appl. Fluoresc.* **6** 012001 (2018)
57. Hestand N J, Spano F C *Chem. Rev.* **118** 7069 (2018)
58. Otsuki J *J. Mater. Chem. A* **6** 6710 (2018)
59. Hecht M, Würthner F *Acc. Chem. Res.* **54** 642 (2021)
60. Ma S et al. *Aggregate* **2** e96 (2021)
61. Shapiro B I et al. *Opt. Express* **26** 30324 (2018)
62. Shapiro B I et al. *Quantum Electron.* **48** 856 (2018); *Kvantovaya Elektron.* **48** 856 (2018)
63. Wiederrecht G P, Wurtz G A, Bouhelier A *Chem. Phys. Lett.* **461** 171 (2008)
64. Fofang N T et al. *Nano Lett.* **8** 3481 (2008)
65. Lebedev V S et al. *Colloids Surf. A* **326** 204 (2008)
66. Lebedev V S et al. *Quantum Electron.* **40** 246 (2010); *Kvantovaya Elektron.* **40** 246 (2010)
67. Antosiewicz T J, Apell S P, Shegai T *ACS Photon.* **1** 454 (2014)
68. Shapiro B I et al. *Quantum Electron.* **45** 1153 (2015); *Kvantovaya Elektron.* **45** 1153 (2015)
69. Todisco F et al. *ACS Photon.* **5** 143 (2018)
70. Song T et al. *Nanomaterials* **9** 564 (2019)
71. Watanabe K et al. *Chem. Rev.* **106** 4301 (2006)
72. Kravets V G et al. *Phys. Rev. Lett.* **105** 246806 (2010)
73. Kravets V G et al. *Nano Lett.* **10** 874 (2010)
74. Singh K et al. *Microchem. J.* **197** 109888 (2024)
75. Walters C M et al. *Adv. Mater.* **30** 1705381 (2018)
76. Ralević U et al. *Appl. Surf. Sci.* **434** 540 (2018)
77. Wang A X, Kong X *Materials* **8** 3024 (2015)
78. Sorokin A V et al. *J. Phys. Chem. C* **119** 2743 (2015)
79. Sorokin A V et al. *J. Phys. Chem. C* **124** 10167 (2020)
80. Lu L et al. *Langmuir* **18** 7706 (2002)
81. Hranisavljevic J et al. *J. Am. Chem. Soc.* **124** 4536 (2002)
82. Zhang J, Fu Y, Lakowicz J R *J. Phys. Chem. C* **111** 50 (2007)
83. Akhavan S et al. *ACS Nano* **11** 5430 (2017)
84. Kabbash M E et al. *J. Nanomater.* **2016** 4819040 (2016)
85. Weeraddana D et al. *J. Chem. Phys.* **147** 074117 (2017)
86. Wiederrecht G P, Wurtz G A, Hranisavljevic J *Nano Lett.* **4** 2121 (2004)
87. Bellessa J et al. *Phys. Rev. B* **80** 033303 (2009)
88. Yoshida A, Kometani N *J. Phys. Chem. C* **114** 2867 (2010)
89. Lebedev V S, Medvedev A S *Quantum Electron.* **42** 701 (2012); *Kvantovaya Elektron.* **42** 701 (2012)
90. Salomon A et al. *ChemPhysChem* **14** 1882 (2013)
91. Balci S *Opt. Lett.* **38** 4498 (2013)
92. DeLacy B G et al. *Nano Lett.* **15** 2588 (2015)
93. Zengin G et al. *Phys. Rev. Lett.* **114** 157401 (2015)
94. Kondorskiy A D et al. *J. Russ. Laser Res.* **36** 175 (2015)
95. Melnikau D et al. *J. Lumin.* **242** 118557 (2022)
96. Bellessa J et al. *Phys. Rev. Lett.* **93** 036404 (2004)
97. Symonds C et al. *New J. Phys.* **10** 065017 (2008)
98. Cade N I, Ritman-Meer T, Richards D *Phys. Rev. B* **79** 241404 (2009)
99. Bellessa J et al. *Electronics* **3** 303 (2014)
100. Chmereva T M, Kucherenko M G, Kurmangaleev K S *Opt. Spectrosc.* **120** 881 (2016); *Opt. Spektrosk.* **120** 941 (2016)
101. Matsui H, in *Noble and Precious Metals–Properties, Nanoscale Effects and Applications* (Eds M Seehra, A Bristow) (London: IntechOpen, 2017) Ch. 5, https://doi.org/10.5772/intechopen.71466
102. Forn-Díaz P et al. *Rev. Mod. Phys.* **91** 025005 (2019)
103. Bitton O, Gupta S N, Haran G *Nanophotonics* **8** 559 (2019)
104. Liu R et al. *Phys. Rev. B* **103** 235430 (2021)
105. Kucherenko M G, Nalbandyan V M, Chmereva T M *Opt. Spectrosc.* **130** 593 (2022); *Opt. Spektrosk.* **130** 745 (2022)
106. Kim Y et al. *Nanophotonics* **12** 413 (2023)
107. Hirai K, Hutchison J A, Uji-i H *Chem. Rev.* **123** 8099 (2023)
108. Jiang P et al. *Opt. Express* **27** 16613 (2019)
109. Tserkezis C et al. *Rep. Prog. Phys.* **83** 082401 (2020)
110. Deng X et al. *Opt. Express* **31** 32082 (2023)
111. Tserkezis C *Phys. Rev. A* **107** 043707 (2023)
112. Manjavacas A, García de Abajo F J, Nordlander P *Nano Lett.* **11** 2318 (2011)
113. DeLacy B G et al. *Opt. Express* **21** 19103 (2013)
114. Schlather A E et al. *Nano Lett.* **13** 3281 (2013)
115. Wurtz G A et al. *Nano Lett.* **7** 1297 (2007)
116. Lebedev V S, Medvedev A S *Quantum Electron.* **43** 1065 (2013); *Kvantovaya Elektron.* **43** 1065 (2013)
117. Lebedev V S, Medvedev A S *J. Russ. Laser Res.* **34** 303 (2013)
118. Moritaka S S et al. *Bull. Lebedev Phys. Inst.* **47** 280 (2020); *Kratk. Soobshch. Fiz. Fiz. Inst. Akad. Nauk* (9) 41 (2020)
119. Moritaka S S, Lebedev V S *Bull. Lebedev Phys. Inst.* **50** 589 (2023); *Kr. Soobshch. Fiz. Fiz. Inst. Akad. Nauk* (12) 112 (2023)
120. Chen H et al. *J. Phys. Chem. C* **116** 14088 (2012)
121. Thomas R et al. *ACS Nano* **12** 402 (2018)
122. Zengin G et al. *Sci. Rep.* **3** 3074 (2013)
123. Simon T et al. *J. Phys. Chem. C* **120** 12226 (2016)
124. Nan F et al. *Nano Lett.* **15** 2705 (2015)
125. Ni W et al. *Nano Lett.* **10** 77 (2010)
126. Lekeufack D D et al. *Appl. Phys. Lett.* **96** 253107 (2010)
127. Melnikau D et al. *Nanoscale Res. Lett.* **8** 134 (2013)
128. Vasa P et al. *EPJ Web Conf.* **41** 09018 (2013)
129. Vasa P et al. *Nature Photon.* **7** 128 (2013)
130. Vasa P, Lienau C *ACS Photon.* **5** 2 (2018)
131. Fain N, Ellenbogen T, Schwartz T *Phys. Rev. B* **100** 235448 (2019)
132. Ates S et al. *Opt. Lett.* **45** 5824 (2020)
133. Guo J et al. *Nanoscale* **13** 15812 (2021)
134. Dey J, Virdi A, Chandra M *Nanoscale* **15** 17879 (2023)
135. Sukharev M, Nitzan A *J. Phys. Condens. Matter* **29** 443003 (2017)
136. Manuel A P et al. *J. Mater. Chem. C* **7** 1821 (2019)
137. Kholmicheva N et al. *Nanophotonics* **8** 613 (2019)
138. Vasa P *Adv. Phys. X* **5** 1749884 (2020)
139. He Z et al. *Appl. Sci.* **10** 1774 (2020)

140. Wei H et al. *Adv. Funct. Mater.* **31** 2100889 (2021)
141. Törmä P, Barnes W L *Rep. Prog. Phys.* **78** 013901 (2015)
142. Cao E et al. *Nanophotonics* **7** 145 (2018)
143. Han Z, Bozhevolnyi S I *Rep. Prog. Phys.* **76** 016402 (2013)
144. Barnes W L, Dereux A, Ebbesen T W *Nature* **424** 824 (2003)
145. Zhang J, Zhang L, Xu W *J. Phys. D* **45** 113001 (2012)
146. Raether H *Surface Plasmons on Smooth and Rough Surfaces and on Gratings* (Springer Tracts in Modern Physics, Vol. 111) (Berlin: Springer-Verlag, 1988) https://doi.org/10.1007/BFb0048317
147. Girard C, Joachim C, Gauthier S *Rep. Prog. Phys.* **63** 893 (2000)
148. Bohren C F, Huffman D R *Absorption and Scattering of Light by Small Particles* (Weinheim: Wiley-VCH Verlag, 1998); Translated into Russian of the 1st ed.: *Pogloshchenie i Rasseyanie Sveta Malymi Chastitsami* (Moscow: Mir, 1985)
149. Hohenau A, Leitner A, Aussenegg F R, in *Surface Plasmon Nanophotonics* (Springer Series in Optical Sciences, Vol. 131, Eds M L Brongersma, P G Kik) (Dordrecht: Springer, 2007) p. 11, https://doi.org/10.1007/978-1-4020-4333-8_2
150. Koch W, Holthausen M C *A Chemist's Guide to Density Functional Theory* (Weinheim: Wiley-VCH, 2001)
151. Chateau D et al. *Nanoscale* **7** 1934 (2015)
152. Cardinal M F et al. *J. Phys. Chem. C* **114** 10417 (2010)
153. Melnikau D et al. *J. Phys. Chem. Lett.* **7** 354 (2016)
154. Scarabelli L, Liz-Marzán L M *ACS Nano* **15** 18600 (2021)
155. Yin Z et al. *RSC Adv.* **6** 86297 (2016)
156. Swarnapali A et al. *Phys. Chem. Chem. Phys.* **17** 21133 (2015)
157. Gaponenko S V *Introduction to Nanophotonics* (Cambridge: Cambridge Univ. Press, 2010)
158. Novotny L, Hecht B *Principles of Nano-Optics* (Cambridge: Cambridge Univ. Press, 2012); Translated into Russian of the 1st ed.: *Osnovy Nanooptiki* (Moscow: Fizmatlit, 2011)
159. Bigot J-Y et al. *Phys. Rev. Lett.* **75** 4702 (1995)
160. Inouye H et al. *Phys. Rev. B* **57** 11334 (1998)
161. Kreibig U, Vollmer M *Optical Properties of Metal Clusters* (Springer Series in Materials Science, Vol. 25) (Berlin: Springer-Verlag, 1995) https://doi.org/10.1007/978-3-662-09109-8
162. Johnson P B, Christy R W *Phys. Rev. B* **6** 4370 (1972)
163. Babar S, Weaver J H *Appl. Opt.* **54** 477 (2015)
164. Palik E D (Ed.) *Handbook of Optical Constants of Solids II* (Boston: Academic Press, 1991)
165. Rakić A D *Appl. Opt.* **34** 4755 (1995)
166. Kondorskiy A D, Mekshun A V *Bull. Lebedev Phys. Inst.* **50** 557 (2023); *Kratk. Soobshch. Fiz. Fiz. Inst. Akad. Nauk* (12) 96 (2023)
167. Kondorskiy A D, Mekshun A V *J. Russ. Laser Res.* **44** 627 (2023)
168. Fuchs R, Claro F *Phys. Rev. B* **35** 3722 (1987)
169. Ruppin R, Yatom H *Phys. Status Solidi B* **74** 647 (1976)
170. Aleksandrov A F, Rukhadze A A *Lektsii po Elektrodinamike Plazmopodobnykh Sred* (Lecture Notes on Electrodynamics of Plasma-Like Media) (Moscow: Izd. Mosk. Univ. Fiz. Fak. MGU, 1999)
171. Kelly K L et al. *J. Phys. Chem. B* **107** 668 (2003)
172. Kondorskiy A D, Lam N T, Lebedev V S *J. Russ. Laser Res.* **39** 56 (2018)
173. Creighton J A, Eadon D G *J. Chem. Soc. Faraday Trans.* **87** 3881 (1991)
174. Kometani N et al. *Langmuir* **17** 578 (2001)
175. Mekshun A V et al. *Bull. Lebedev Phys. Inst.* **47** 276 (2020); *Kratk. Soobshch. Fiz. Fiz. Inst. Akad. Nauk* (9) 34 (2020)
176. Payne E M et al. *J. Phys. Chem. B* **110** 2150 (2006)
177. Khlebtsov B N, Melnikov A, Khlebtsov N G *J. Quant. Spectrosc. Radiat. Transfer* **107** 306 (2007)
178. Zenin V A et al. *ACS Photon.* **7** 1067 (2020)
179. Ray D, Kiselev A, Martin O J F *Opt. Express* **29** 24056 (2021)
180. Frenkel J *Phys. Rev.* **37** 1276 (1931)
181. Davydov A S *Theory of Molecular Excitons* (New York: Plenum Press, 1971); Translated from Russian: *Teoriya Molekulyarnykh Eksitonov* (Moscow: Nauka, 1968)
182. Shapiro B I *Nanotechnol. Russ.* **3** 139 (2008); *Ross. Nanoteknol.* **3** 72 (2008)
183. Todisco F et al. *ACS Nano* **9** 9691 (2015)
184. Takeshima N et al. *Nanoscale Res. Lett.* **15** 15 (2020)
185. Asanuma H et al. *J. Photochem. Photobiol. C* **13** 124 (2012)
186. Ciardelli F, Ruggeri G, Pucci A *Chem. Soc. Rev.* **42** 857 (2013)
187. Shapiro B I et al. *Nanotechnol. Russ.* **5** 58 (2010); *Ross. Nanoteknol.* **5** 35 (2010)
188. Kobayashi T (Ed.) *J-Aggregates* (Singapore: World Scientific, 1996) https://doi.org/10.1142/3168
189. Brixner T et al. *Adv. Energy Mater.* **7** 1700236 (2017)
190. Lee C C et al. *Chem. Soc. Rev.* **38** 671 (2009)
191. Bardeen C J *Annu. Rev. Phys. Chem.* **65** 127 (2014)
192. McRae E G, Kasha M *J. Chem. Phys.* **28** 721 (1958)
193. Kasha M, in *Physical Processes in Radiation Biology. Proc. of an Intern. Symp., Michigan State Univ., May 6–8, 1963* (Eds L Augenstein, R Mason, B Rosenberg) (New York: Academic Press, 1964) p. 17
194. Kasha M, Rawls H R, El-Bayoumi M A *Pure Appl. Chem.* **11** 371 (1965)
195. Didraga C et al. *J. Phys. Chem. B* **108** 14976 (2004)
196. Scheblykin I G et al. *J. Phys. Chem. B* **105** 4636 (2001)
197. Moritaka S S, Lebedev V S *JETP Lett.* **118** 792 (2023); *Pis'ma Zh. Eksp. Teor. Fiz.* **118** 794 (2023)
198. Moritaka S S, Lebedev V S *J. Chem. Phys.* **160** 074901 (2024)
199. Dicke R H *Phys. Rev.* **93** 99 (1954)
200. Gierschner J et al. *J. Phys. Chem. Lett.* **4** 2686 (2013)
201. Gierschner J, Park S Y *J. Mater. Chem. C* **1** 5818 (2013)
202. Chuang C et al. *Chem* **5** 3135 (2019)
203. Deshmukh A P et al. *J. Phys. Chem. C* **123** 18702 (2019)
204. Zhu T, Wan Y, Huang L *Acc. Chem. Res.* **50** 1725 (2017)
205. Levitz A, Marmarchi F, Henary M *Photochem. Photobiol. Sci.* **17** 1409 (2018)
206. Doria S et al. *ACS Nano* **12** 4556 (2018)
207. Bogdanov V L et al. *JETP Lett.* **53** 105 (1991); *Pis'ma Zh. Eksp. Teor. Fiz.* **53** 100 (1991)
208. Wang Y *J. Opt. Soc. Am. B* **8** 981 (1991)
209. Zhuravlev F A et al. *JETP Lett.* **56** 260 (1992); *Pis'ma Zh. Eksp. Teor. Fiz.* **56** 264 (1992)
210. Shelkovnikov V V et al. *J. Struct. Chem.* **34** 909 (1993); *Zh. Strukt. Khim.* **34** 90 (1993)
211. Gadonas R, Feller K-H, Pugzlys A *Opt. Commun.* **112** 157 (1994)
212. Spano F C, Knoester J, in *Advances in Magnetic and Optical Resonance* Vol. 18 (Ed. W S Warren) (New York: Academic Press, 1994) p. 117
213. Markov R V et al. *Nonlinear Opt.* **25** 365 (2000)
214. Shelkovnikov V V et al. *Opt. Spectrosc.* **92** 884 (2002); *Opt. Spektrosk.* **92** 958 (2002)
215. Shelkovnikov V V, Plekhanov A I, in *Macro to Nano Spectroscopy* (Ed. J Uddin) (Rijeka: IntechOpen, 2012) p. 317, https://doi.org/10.5772/48055
216. Lee Y U et al. *Adv. Opt. Mater.* **6** 1701400 (2018)
217. Gerasimova T N et al. *Chem. Sustain. Dev.* **8** 109 (2000)
218. Markov R V et al. *Quantum Electron.* **31** 1063 (2001); *Kvantovaya Elektron.* **31** 1063 (2001)
219. Markov R V et al. *J. Exp. Theor. Phys.* **99** 480 (2004); *Zh. Eksp. Teor. Fiz.* **126** 549 (2004)
220. Sasaki F, Kano T, Kobayashi S *Phys. Rev. B* **63** 205411 (2001)
221. Bednarz M, Knoester J *J. Phys. Chem. B* **105** 12913 (2001)
222. Kano H, Kobayashi T *J. Chem. Phys.* **116** 184 (2002)
223. Rehhagen C et al. *J. Phys. Chem. Lett.* **11** 6612 (2020)
224. Belko N V et al. *J. Phys. Chem. C* **126** 7922 (2022)
225. Jumbo-Nogales A et al. *J. Phys. Chem. Lett.* **13** 10198 (2022)
226. Knoester J, Spano F C, in *J-Aggregates* (Ed. T Kobayashi) (Singapore: World Scientific, 1996) p. 111, https://doi.org/10.1142/9789812830029_0005
227. Nishimura K, Tokunaga E, Kobayashi T *Chem. Phys. Lett.* **395** 114 (2004)
228. Dijkstra A G, Jansen T C, Knoester J *J. Chem. Phys.* **128** 164511 (2008)
229. Milota F et al. *J. Chem. Phys.* **131** 054510 (2009)
230. Abramavicius D et al. *Chem. Rev.* **109** 2350 (2009)
231. Ginsberg N S, Cheng Y-C, Fleming G R *Acc. Chem. Res.* **42** 1352 (2009)
232. Bolzonello L, Fassioli F, Collini E *J. Phys. Chem. Lett.* **7** 4996 (2016)
233. Quenzel T et al. *ACS Nano* **16** 4693 (2022)
234. Peruffo N, Mancin F, Collini E *Adv. Opt. Mater.* **11** 2203010 (2023)
235. Russo M et al. *Adv. Opt. Mater.***12** 2400821 (2024)
236. Fidder H, Knoester J, Wiersma D A *J. Chem. Phys.* **98** 6564 (1993)

237. Minoshima K et al. *Chem. Phys. Lett.* **218** 67 (1994)
238. Gadonas R et al. *J. Chem. Phys.* **106** 8374 (1997)
239. Hirschmann R et al. *Chem. Phys. Lett.* **151** 60 (1988)
240. Malyshev V A, Moreno P *Phys. Rev. A* **53** 416 (1996)
241. Malyshev V A, Glaeske H, Feller K-H *Phys. Rev. A* **58** 670 (1998)
242. Glaeske H, Malyshev V A, Feller K-H *Phys. Rev. A* **65** 033821 (2002)
243. Klugkist J A, Malyshev V, Knoester J *J. Chem. Phys.* **127** 164705 (2007)
244. Klugkist J A, Malyshev V A, Knoester J *J. Chem. Phys.* **128** 084706 (2008)
245. Zabolotskii A A *Opt. Spectrosc.* **101** 606 (2006); *Opt. Spektrosk.* **101** 644 (2006)
246. Zabolotskii A A *J. Exp. Theor. Phys.* **106** 404 (2008); *Zh. Eksp. Teor. Fiz.* **133** 466 (2008)
247. Nesterov L A et al. *Opt. Spectrosc.* **115** 499 (2013); *Opt. Spektrosk.* **115** 572 (2013)
248. Zabolotskii A A *Optoelectron. Instrum. Data Process.* **52** 76 (2016); *Avtometriya* **52** 92 (2016)
249. Boyd R W *Nonlinear Optics* (Amsterdam: Elsevier, 2008)
250. Wooten F *Optical Properties of Solids* (New York: Academic Press, 1972)
251. Kondorskiy A D, Moritaka S S, Lebedev V S *Opt. Express* **30** 4600 (2022)
252. Kondorskiy A D *Chinese Opt. Lett.* **22** 093602 (2024)
253. Grynberg G, Aspect A, Fabre C *Introduction to Quantum Optics: From the Semi-Classical Approach to Quantized Light* (Cambridge: Cambridge Univ. Press, 2010)
254. Meystre P, Sargent M (III) *Elements of Quantum Optics* (Berlin: Springer, 2007)
255. Abrikosov A A, Gorkov L P, Dzyaloshinski I E *Methods of Quantum Field Theory in Statistical Physics* (Englewood Cliffs, NJ: Prentice-Hall, 1963); Translated from Russian: *Metody Kvantovoi Teorii Polya v Statisticheskoi Fizike* (Moscow: Fizmatgiz, 1962)
256. Campa A et al. *Physics of Long-Range Interacting Systems* (Oxford: Oxford Univ. Press, 2014) Ch. 7
257. White A J, Galperin M *Phys. Chem. Chem. Phys.* **14** 13809 (2012)
258. Zubarev D N *Sov. Phys. Usp.* **3** 320 (1960); *Usp. Fiz. Nauk* **71** 71 (1960)
259. Fuller K A *Opt. Lett.* **18** 257 (1993)
260. Aden A L, Kerker M *J. Appl. Phys.* **22** 1242 (1951)
261. Güttler A *Ann. Physik* **11** 65 (1952) https://doi.org/10.1002/andp.19524460202
262. Ruppin R, Englman R *J. Phys. C* **1** 630 (1968)
263. Irimajiri A, Hanai T, Inouye A *J. Theor. Biol.* **78** 251 (1979)
264. Bhandari R *Appl. Opt.* **24** 1960 (1985)
265. Wu Z S, Wang Y P *Radio Sci.* **26** 1393 (1991)
266. Sinzig J, Quinten M *Appl. Phys. A* **58** 157 (1994)
267. Stratton J A *Electromagnetic Theory* (Hoboken, NJ: John Wiley and Sons, 2007); Translated into Russian of the 1st ed.: *Teoriya Elektromagnetizma* (Moscow–Leningrad: Gostekhizdat, 1948)
268. Barber P W, Hill S C *Light Scattering by Particles: Computational Methods* (Advanced Ser. in Applied Physics, Vol. 2) (Singapore: World Scientific, 1990)
269. Scaife B K P *Principles of Dielectrics* (Oxford: Oxford Univ. Press, 1998)
270. Voshchinnikov N V, Farafonov V G *Astrophys. Space Sci.* **204** 19 (1993)
271. Wang D-S, Kerker M *Phys. Rev. B* **25** 2433 (1982)
272. Ambjörnsson T et al. *Phys. Rev. B* **73** 085412 (2006)
273. Taflove A, Hagness S C *Computational Electrodynamics: The Finite-Difference Time-Domain Method* (Boston: Artech House, 2005)
274. Waterman P C *Phys. Rev. D* **3** 825 (1971)
275. Mishchenko M I, Travis L D, Lacis A A *Scattering, Absorption, and Emission of Light by Small Particles* (Cambridge: Cambridge Univ. Press, 2002)
276. Hafner Ch *The Generalized Multipole Technique for Computational Electromagnetics* (Boston: Artech House, 1990)
277. Moreno E et al. *J. Opt. Soc. Am. A* **19** 101 (2002)
278. Yurkin M A, Hoekstra A G *J. Quant. Spectrosc. Radiat. Transfer* **106** 558 (2007)
279. Lee J, Mal A K *Appl. Math. Comput.* **67** 135 (1995) https://doi.org/10.1016/0096-3003(94)00057-B
280. Nitzan A, Brus L E *J. Chem. Phys.* **75** 2205 (1981)
281. Gersten J, Nitzan A *J. Chem. Phys.* **75** 1139 (1981)
282. Gersten J, Nitzan A *J. Chem. Phys.* **73** 3023 (1980)
283. Shah R A et al. *Phys. Rev. B* **88** 075411 (2013)
284. Joe Y S, Satanin A M, Kim C S *Phys. Scr.* **74** 259 (2006)
285. Miroshnichenko A E, Flach S, Kivshar Yu S *Rev. Mod. Phys.* **82** 2257 (2010)
286. Krivenkov V et al. *Laser Photon. Rev.* **13** 1800176 (2019)
287. Fleischhauer M, Imamoglu A, Marangos J P *Rev. Mod. Phys.* **77** 633 (2005)
288. Peng B et al. *Nat. Commun.* **5** 5082 (2014)
289. Limonov M F et al. *Nature Photon.* **11** 543 (2017)
290. Gallinet B, in *Fano Resonances in Optics and Microwaves: Physics and Applications* (Springer Ser. in Optical Sciences, Vol. 219, Eds E Kamenetskii, A Sadreev, A Miroshnichenko) (Cham: Springer, 2018) p. 109, https://doi.org/10.1007/978-3-319-99731-5_5
291. Fano U *Phys. Rev.* **124** 1866 (1961)
292. Landau L D, Lifshitz E M *Quantum Mechanics: Non-Relativistic Theory* (Oxford: Pergamon Press, 1991); Translated from Russian: *Kvantovaya Mekhanika: Nerelyativistskaya Teoriya* (Moscow: Nauka, 1989)
293. Dong Z C et al. *Nature Photon.* **4** 50 (2010)
294. Jaynes E T, Cummings F W *Proc. IEEE* **51** 89 (1963)
295. Moritaka S S, Lebedev V S *Bull. Lebedev Phys. Intst.* **51** S750 (2024); *Kvantovaya Elektron.* **54** 362 (2024)
296. Gómez D E, Giessen H, Davis T J *J. Phys. Chem. C* **118** 23963 (2014)
297. Kondorskiy A D, Lebedev V S *Quantum Electron.* **48** 1035 (2018); *Kvantovaya Elektron.* **48** 1035 (2018)
298. Kondorskiy A D, Mekshun A V *Bull. Lebedev Phys. Inst.* **49** 341 (2022); *Kratk. Soobshch. Fiz. Fiz. Inst. Akad. Nauk* (10) 55 (2022)
299. Kondorskiy A D, Lebedev V S *Opt. Express* **27** 11783 (2019)
300. Wiederrecht G P, Hall, J E, Bouhelier A *Phys. Rev. Lett.* **98** 083001 (2007)
301. Petoukhoff C E, Dani K M, O'Carroll D M *Polymers* **12** 2141 (2020)
302. Faucheaux J A, Fu J, Jain P K *J. Phys. Chem. C* **118** 2710 (2014)
303. Chen H et al. *J. Phys. Chem. C* **116** 14088 (2012)
304. Fleischmann M, Hendra P J, McQuillan A J *Chem. Phys. Lett.* **26** 163 (1974)
305. Campion A, Kambhampati P *Chem. Soc. Rev.* **27** 241 (1998)
306. Cui L et al. *Sci. Rep.* **5** 11920 (2015)
307. Pockrand I et al. *J. Chem. Phys.* **70** 3401 (1979)
308. Pompa P P et al. *Nature Nanotechnol.* **1** 126 (2006)
309. Yeh D-M et al. *Nanotechnology* **19** 345201 (2008)
310. Dulkeith E et al. *Phys. Rev. Lett.* **89** 203002 (2002)
311. Liu X et al. *Nature Photon.* **9** 30 (2015)
312. Liu W et al. *Nano Lett.* **16** 1262 (2016)
313. Pelton M, Storm S D, Leng H *Nanoscale* **11** 14540 (2019)
314. Khitrova G et al. *Nature Phys.* **2** 81 (2006)
315. Wu F et al. *ACS Nano* **15** 2292 (2021)
316. Petoukhoff C E, Dani K M, O'Carroll D M, in *JSAP–OSA Joint Symp. 2019 Abstracts, OSA Technical Digest* (Washington, DC: Optica Publ. Group, 2019) paper 18p_E208_13, https://doi.org/10.1364/JSAP.2019.18p_E208_13
317. Xiong X et al. *Nanophotonics* **9** 257 (2020)
318. Balci F M et al. *J. Phys. Chem. C* **123** 26571 (2019)
319. Schwartz T et al. *Phys. Rev. Lett.* **106** 196405 (2011)
320. Sato T et al. *Chem. Lett.* **30** 402 (2001)
321. Wurtz G A, Hranisavljevic J, Wiederrecht G P *J. Microsc.* **210** 340 (2003)
322. Uwada T et al. *J. Phys. Chem. C* **111** 1549 (2007)
323. Yoshida A, Yonezawa Y, Kometani N *Langmuir* **25** 6683 (2009)
324. Vujačić A et al. *J. Phys. Chem. C* **116** 4655 (2012)
325. Laban B et al. *J. Phys. Chem. C* **118** 23393 (2014)
326. Laban B B, Vodnik V, Vasić V *Nanospectroscopy* **1** 5460 (2015)
327. Gülen D *J. Phys. Chem. C* **114** 13825 (2010)
328. Balci S et al. *ACS Photon.* **3** 2010 (2016)
329. Lam N T, Kondorskiy A D, Lebedev V S *Bull. Lebedev Phys. Inst.* **46** 390 (2019); *Kratk. Soobshch. Fiz. Fiz. Inst. Akad. Nauk* (12) 34 (2019)
330. Yoshida A, Uchida N, Kometani N *Langmuir* **25** 11802 (2009)
331. Solomon M L et al. *Acc. Chem. Res.* **53** 588 (2020)
332. Zhu J et al. *Nano Lett.* **21** 3573 (2021)
333. He C et al. *Nano Lett.* **23** 9428 (2023)
334. Kumar M et al. *ACS Appl. Nano Mater.* **6** 13894 (2023)

335. Cheng Q et al. *Nano Lett*. **23** 11376 (2023)
336. Gunnarsson L et al. *J. Phys. Chem. B* **109** 1079 (2005)
337. Scherer P O J, Fischer S F *Chem. Phys*. **86** 269 (1984)
338. Misawa K et al. *J. Lumin*. **60–61** 812 (1994)
339. Tani T et al. *J. Lumin*. **122–123** 244 (2007)
340. Obara Y et al. *Int. J. Mol. Sci*. **13** 5851 (2012)
341. Haverkort F, Stradomska A, Knoester J *J. Phys. Chem. B* **118** 8877 (2014)
342. Pugzlys A et al. *Int. J. Photoenergy* **2006** 029623 (2006)
343. Qiu C et al. *Laser Photon. Rev*. **4** 268 (2010)
344. Roth J, Dignam M J *J. Opt. Soc. Am*. **63** 308 (1973)
345. Auguié B, Le Ru E C *J. Phys. Chem. C* **122** 19110 (2018)
346. Tang C, Auguié B, Le Ru E C *ACS Photon*. **5** 5002 (2018)
347. Tang C, Auguié B, Le Ru E C *Phys. Rev. A* **104** 033502 (2021)
348. Auguié B, Darby B L, Le Ru E C *Nanoscale* **11** 12177 (2019)
349. Tang C, Auguié B, Le Ru E C *Phys. Rev. B* **103** 085436 (2021)
350. Kalsin A M et al. *Science* **312** 420 (2006)
351. Kowalczyk B et al. *Nature Mater*. **11** 227 (2012)
352. Stete F et al. *ACS Photon*. **10** 2511 (2023)